

W1993

6 GC
7.1

**A TOMOGRAPHIC VIEW OF THE GULF STREAM
SOUTHERN RECIRCULATION GYRE AT 38°N, 55°W**

C54

1993

by

David Brian Chester

B.S. Southampton College of Long Island University
(1986)

M.S. Massachusetts Institute of Technology/Woods Hole
Oceanographic Institution
(1989)

Submitted in partial fulfillment of the
requirements for the degree of

Doctor of Philosophy

at the

MASSACHUSETTS INSTITUTE OF TECHNOLOGY

and the

WOODS HOLE OCEANOGRAPHIC INSTITUTION

February 1993

© David B. Chester 1993

The author hereby grants to MIT and to WHOI permission to reproduce
and to distribute copies of this thesis document in whole or in part.

Signature of Author

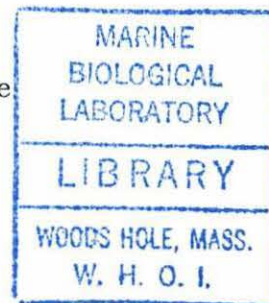
Joint Program in Physical Oceanography
Massachusetts Institute of Technology
Woods Hole Oceanographic Institution
January 29, 1993

Certified by *E*

Paola Malanotte-Rizzoli
Professor
Thesis Supervisor

Accepted by *u*

Lawrence J. Pratt
Chairman, Joint Committee for Physical Oceanography
Massachusetts Institute of Technology
Woods Hole Oceanographic Institution



A TOMOGRAPHIC VIEW OF THE GULF STREAM SOUTHERN RECIRCULATION GYRE AT 38°N, 55°W

by

David Brian Chester

Submitted in partial fulfillment of the requirements for the degree of
Doctor of Philosophy at the Massachusetts Institute of Technology
and the Woods Hole Oceanographic Institution

January 29, 1993

Abstract

Reciprocal acoustic transmissions made in a region just south of the Gulf Stream are analyzed to determine the structure and variability of temperature, current velocity, and vorticity fields at the northern extent of the southern recirculation gyre. For ten months (November, 1988 through August, 1989), a pentagonal array of tomographic transceivers was situated in a region centered at 38°N, 55°W as part of the eastern array of the SYNOP (SYNoptic Ocean Prediction) Experiment. The region of focus is one rich in mesoscale energy, with the influence of local Gulf Stream meandering and cold-core ring activity strikingly evident. Daily-averaged acoustic transmissions yielded travel times which were inverted to obtain estimates of range-averaged temperature and current velocity fields, and area-averaged relative vorticity fields. The acoustically determined estimates are consistent with nearby current meter measurements and satellite infrared imagery. The signature of cold-core rings is clearly evident in the sections. Spectral estimates of the fields are dominated by motions with periodicities ranging from 32–128 days. Second-order statistics, such as eddy kinetic energies, and heat and momentum fluxes, are also estimated. The integrating nature of the tomographic measurement has been exploited to shed some light on the radiation of eddy energy from the Gulf Stream. The Eliassen–Palm flux diagnostic has been applied to an investigation of wave radiation from the Gulf Stream. Results of the diagnosis suggest that the Gulf Stream itself is the source of wave energy radiating into the far field and found in the interior of the North Atlantic subtropical gyre.

Thesis Supervisor:

Dr. Paola Malanotte-Rizzoli, Professor
Massachusetts Institute of Technology

Table of Contents

Abstract	3
Acknowledgments	7
List of Tables	9
List of Figures	11
1. Introduction	15
1.1 Motivation	15
1.2 Background	17
1.3 Novel Aspects of Thesis	22
1.4 Thesis Overview	25
2. The 1988/1989 SYNOP Gulf Stream Tomography Experiment	27
2.1 Oceanographic Setting	27
2.2 Experimental Design	36
2.3 Environmental Data	42
3. Formulation of the Tomographic Inverse Problem	47
3.1 Introduction	47
3.2 The Forward Problem	51
3.3 The Inverse Problem	55
3.4 Acoustic Considerations	57
3.5 The Processed Tomographic Data	64

3.6	Errors	76
3.6.1	Introduction	76
3.6.2	Travel Time Variance	78
3.6.3	Mooring Motion	85
3.6.4	Inverse Solution Errors — Resolution and Variance	92
3.6.5	Discussion	93
4.	The Oceanographic Fields	97
4.1	The Ocean Model	97
4.2	Temperature	103
4.3	Current Velocity	109
4.4	Vorticity	117
4.5	Discussion	124
5.	Statistics and Dynamics	127
5.1	Introduction	127
5.2	Statistics of the Region	131
5.3	The Vorticity Equation	137
5.4	Eliassen–Palm Flux Calculation	140
5.5	Discussion	144
6.	Summary and Discussion	149
	Appendix A: Ambient Noise	155
	References	159

Acknowledgments

First of all I would like to thank my thesis advisor, Paola Malanotte-Rizzoli, for her patient guidance and support, and the freedom she has given me along the way. Her enthusiasm and generous encouragement have been a constant source of inspiration. I would also like to thank the members of my thesis committee — Nelson Hogg, Jim Lynch, Joe Pedlosky, and Carl Wunsch, and the defense chairman, Breck Owens, for many valuable suggestions concerning various aspects of the thesis, and oceanography in general. Critical comments of earlier drafts of this thesis have greatly improved the accuracy and readability of the text. I cannot imagine assembling a more qualified group of individuals.

Nick Witzell was instrumental in the engineering and testing of the tomographic transceivers. Conversations with Doug Webb, Pierre Tillier, and Steve Liberatore have led to much of my understanding of the operation of the tomographic instrumentation. Art Newhall was also very helpful with computer programming pointers, especially during the initial processing of the raw tomographic data. Nelson Hogg generously provided the current meter data used in this thesis. Numerical model output was graciously supplied by Antonietta Capotondi. Sean Kery provided the NOYFB mooring motion program, along with user-friendly tips on its execution. The interaction with fellow Joint Program students, too many to mention, has also been stimulating and much appreciated. I would also like to thank Anne-Marie Michael for her invaluable assistance in the preparation of the manuscript.

Last but not least I would like to thank my family and friends for their unyielding support throughout my stay at Woods Hole. Their continual encouragement and good nature have kept me on an even keel despite the occasional maelstrom.

This research was carried out under Office of Naval Research (ONR) University Research Initiative contract N00014-86-K-0751 and ONR contract N00014-90-J-1481. Construction of the tomographic instruments was supported by grants and contracts with MIT: National Science Foundation grant OCE 85-12430 and by ONR. The field work was supported by ONR under contract N00014-85-G-0241 (Secretary of the Navy Professorship (C. Wunsch)).

List of Tables

2.1	Instrument Locations	38
2.2	Signal Parameters	39
3.1	Signal-to-Noise Ratio	68
3.2	Cross-Correlation Statistics	71
3.3	Travel Time Variance	84
3.4	Precision of Tomographic Measurement	95
5.1	Statistical Comparison	134

List of Figures

2.1	Map of the western North Atlantic.	28
2.2	Mean and kinetic energy for the North Atlantic.	29
2.3	Mesoscale variability of the Atlantic Ocean from Geosat altimetry. .	30
2.4	Horizontal distribution of eddy kinetic energy at 700 m depth in the western North Atlantic.	30
2.5	Zonal velocity and eddy kinetic energy sections along 55°W.	31
2.6	A scheme for the total transport in the western North Atlantic. . . .	32
2.7	Velocity stick plot time series for mooring 8 of Polymode Array 2. .	34
2.8	Temperature time series for mooring 8 of Polymode Array 2.	35
2.9	Observational plan of the SYNoptic Ocean Prediction Experiment (SYNOP).	37
2.10	Velocity stick plot time series for current meter mooring 11 of the eastern array.	43
2.11	Temperature time series for current meter mooring 11 of the eastern array.	44
3.1	Levitus climatological sound speed profile at 37°N, 55°W.	58
3.2	Range-independent ray traces for moorings 2 to 4 and moorings 2 to 5.	60
3.3	Arrival time sequences for the eigenrays depicted in Figure 3.2. . . .	61
3.4	Order of ray arrivals.	63
3.5	Raw pulse response records for S2R5 and S5R2.	65
3.5	Raw pulse response records for S4R5 and S5R4.	66
3.6	Daily-averaged pulse response records for S2R5 and S5R2.	69
3.6	Daily-averaged pulse response records for S4R5 and S5R4.	70
3.7	Peaks for S2R5 and S5R2.	73

3.7	Peaks for S4R5 and S5R4.	74
3.8	Tomographic pressure records for moorings 2 and 4.	87
3.9	Comparison of observed mooring 3 transceiver depth excursion with NOYFB model predictions.	89
3.10	Difference of mooring 3 transceiver depth excursion and NOYFB model predictions.	90
3.11	Moorings motion model-predicted regression curve for horizontal excur- sion versus vertical excursion.	91
4.1	Ray identification for S5R2.	99
4.2	The ocean model and ray path spatial coverage for case S2R5. . . .	100
4.3	Buoyancy frequency profile from Levitus climatological data.	101
4.4	Temperature anomaly for leg 2↔5.	105
4.5	Satellite sea surface IR (temperature) maps for November 7, 1988 and April 1, 1989.	106
4.6	Comparison of tomographic measurement of temperature with the average of two temperature thermistor measurements.	107
4.7	Temperature power spectra at 1000 m depth.	108
4.8	Current velocity for leg 3 ↔ 4.	110
4.9	Comparison of tomographic measurement of current velocity with an average of current meter measurements.	111
4.10	Comparison of tomographic measurement of current velocity with a single current meter measurement.	113
4.11	Coherence between the tomographic and current meter measurement of velocity.	114
4.12	Surface streamfunctions for the quasi-geostrophic numerical model domain.	115
4.13	Velocity power spectra at 1000 m depth.	116
4.14	Relative vorticity for area 2345.	118

4.15	Time series of relative vorticity at a depth of 1000 m.	119
4.16	Comparison of tomographic estimate of relative vorticity with current meter estimate of $dv/dx - du/dy$	120
4.17	Comparison of tomographic estimate of relative vorticity with current meter estimate of the circulation.	122
4.18	Spectral comparison of relative vorticity estimates obtained from tomography, current meter and numerical model.	123
5.1	Meridional heat-flux spectrum.	136
5.2	Eliassen-Palm flux vectors.	143
A.1	Ambient noise calculation.	156
A.2	Ambient noise level at mooring 2.	157

Chapter 1. Introduction

1.1 Motivation

Some of the most energetic features of the world's oceans are contained within the western boundary regions of the subtropical gyres. The western boundary currents, as exemplified by the Gulf Stream in the North Atlantic, the Kuroshio in the North Pacific, and the Agulhas in the Indian Ocean, play a major role in the global heat budget by transporting mass and warm water from the tropics to high latitudes. At the same time, these very currents are responsible for dissipating much of the torque and energy imparted to the oceanic surface by the atmospheric winds. Not surprisingly then, the dynamics of the western boundary regions are quite complex, involving the interplay of motions occupying a full spectrum of space and time scales.

The Gulf Stream is prototypical of such energetic western boundary currents. Upon exiting the Florida Straits with a transport of about $30 \times 10^6 \text{ m}^3/\text{s}$ the Gulf Stream remains a relatively thin jet of warm water proceeding northeastward along the continental slope. The transport of the Gulf Stream doubles by the time it reaches Cape Hatteras, but the fundamental character of the Stream remains intact. Continuing northeastward toward the New England Seamount Chain, the Gulf Stream becomes a broader, more sinuous current system, with a transport of roughly $150 \times 10^6 \text{ m}^3/\text{s}$ in the vicinity of the seamounts. Further downstream, east of the seamounts, the Gulf Stream System evolves into an eastward flowing jet flanked by a northern and southern countercurrent. The structure of the Gulf Stream System is very complicated in this region, with large-amplitude meandering

of the jet and the formation and growth of rings being commonplace. The transport of the eastward moving Gulf Stream reduces to about $100 \times 10^6 \text{ m}^3/\text{s}$ at 55°W as much of the Gulf Stream water recirculates in a cyclonic northern gyre and an anticyclonic southern gyre. The two recirculation gyres are largely responsible for the enhanced downstream transport of the Gulf Stream. They are complex circulations which result from the interaction of a strong western boundary current with a highly energetic eddy field.

Large-scale distribution of eddy energy illustrates a remarkable inhomogeneity in the world oceans, with a preponderance of eddy kinetic and eddy potential energy in the immediate vicinity of the western boundary currents of the subtropical gyres (see *e.g.*, Wyrski *et al.*, 1976; Dantzler, 1977; Stammer and Böning, 1992). It seems natural to conclude that this energetic mesoscale variability originates from the boundary currents themselves. The dominant source of eddy energy in the Gulf Stream region, and in much of the gyre interior, appears to derive from instabilities of the Gulf Stream itself. Both observational evidence and recent theoretical studies support this claim (Hogg, 1981; Wunsch, 1983; Malanotte-Rizzoli *et al.*, 1987; Hogg, 1988; Welsh *et al.*, 1991; Bower and Hogg, 1992; Malanotte-Rizzoli *et al.*, 1992). Eddy energy and momentum deriving from the instabilities can be fed into the gyre interior. Gulf Stream rings and meanders can act as transport mechanisms in this scenario (Flierl and Robinson, 1984). Radiating Rossby waves can play a prominent role in this scheme (see *e.g.*, Hogg, 1988; Bower and Hogg, 1992; Malanotte-Rizzoli *et al.*, 1992). Hogg (1983) and Brown *et al.*, (1986) find that both the lateral and vertical eddy momentum fluxes are important contributors to the Gulf Stream/southern recirculation gyre exchange processes. In addition, flow over

topography, in this case the New England Seamount Chain, may also provide an additional source of eddy energy, primarily in the abyssal circulation (Hogg, 1983).

Several important questions remain unanswered or only partially addressed. The most significant concern is an adequate description of the mean and variability fields of temperature, current velocity, and relative vorticity in the near-field region. We can then look in greater detail at important questions regarding the physics of these dynamically active areas of the oceanic circulation. What do the mean and variability fields of the near-field look like? Is there any conclusive signature of wave radiation in these regions? It is not known *a priori* that we will be able to distinguish the radiation signature in the near-field region as the wave train may not be well organized this close to the Stream. What processes are responsible for radiating the energy away from the currents to the near and far field? A major goal of this thesis is to investigate these issues.

1.2 Background

The main focus of this thesis is on the physics of the Gulf Stream near-field region. The oceanographic setting for this endeavor is the northern reaches of the southern recirculation gyre at 55°W. This recirculation area is a northwestern intensification of the circulation within the North Atlantic subtropical gyre. It is a region of highly energetic variability (see *e.g.*, Wyrski *et al.*, 1976; Dantzler, 1977; Richardson, 1983; Richman *et al.*, 1977), with the nearby passage of the Stream and its large-amplitude meandering having a dramatic influence on the properties of the field. The southern recirculation gyre comprises a large portion of the region south of the Gulf Stream in the vicinity of the New England Seamounts. East of the

seamounts, Gulf Stream water leaves the core of the current, proceeds in a southwesterly direction, and reenters the Stream upstream of the seamounts. Further south of this tight anticyclonic gyre is a broader, more diffuse westward flow. The formation, growth, and detachment of rings from the Gulf Stream are commonplace occurrences in the Gulf Stream system, and the subsequent westward propagation of rings in the near field dominates much of the variability of the recirculation region. The Gulf Stream has been intensively studied by several generations of oceanographers, and an important verdict has been reached — to fully understand the Stream and its evolution, the Stream itself cannot be studied in isolation from its surroundings. The path and variability of the Stream are directly coupled to the near field, with the meandering stream feeding the eddy field, and vice versa.

Theoretical endeavors, primarily in the realm of numerical modeling, have provided much insight into the dynamics of these regions. Rhines and Holland (1979) and Holland and Rhines (1980) point out the importance of energy conversions to maintain the observed structures. The somewhat idealized model results indicate that the recirculation cells result from the eddy vorticity fluxes, more significantly from the divergence of the eddy vorticity fluxes. As the Gulf Stream proceeds northward, the acquired planetary vorticity must be compensated by a corresponding adjustment in the relative vorticity and/or vortex stretching. The potential vorticity must somehow be dissipated for the Stream to connect to the interior flow, and this is presumably accomplished through eddy fluxes. Vorticity conservation demands that the flow move along isopleths of constant potential vorticity. Eddy fluxes of potential vorticity drive circulations across mean potential vorticity contours, and quasigeostrophic numerical models suggest that these fluxes may be very important terms in the mean dynamical balances in recirculation re-

gions. The eddy vorticity flux is composed of two terms — a relative vorticity flux which represents the lateral transfer of momentum and a stretching flux which is responsible for the vertical transfer of momentum. The stretching flux arises due to changes in the thickness of isopycnal layers. The relative vorticity flux dominates in the western boundary region of the model ocean, but the stretching flux dominates in the gyre interior. Holland and Rhines (1980) find that the eddy potential vorticity flux is directed down the mean potential vorticity gradient, a result which is consistent with eddy generation via instability. Again, it is the divergence of these terms that is important in driving the recirculation gyres themselves.

Instabilities of the Stream and recirculation regions have significant implications for the local dynamical balances. The Gulf Stream transports warm water to the north. The temperature of the Gulf Stream water is warmer than the temperature of the water in the northern reaches of the southern recirculation gyre. This creates the potential for local baroclinic instability. A heat flux directed down this thermal gradient (*i.e.*, to the south) is then able to release available potential energy of the large-scale circulation, and feed it into the eddy field. The result is to lessen the meridional gradients somewhat at the expense of supplying kinetic and potential energy to the eddies. Barotropic instability of the Stream is also important in the region. Observational evidence suggests that negative values of the momentum flux exist north of the Stream, and positive values to the south (see *e.g.*, Bower and Hogg, 1992). Bower and Hogg do not see clear evidence of wave radiation away from the Stream to the south, and speculate that other eddy-generation mechanisms, such as baroclinic instability of the westward recirculation, may mask the radiating signal.

Various observational studies have focused on the Gulf Stream near-field region. Variability of this region has been shown to be dominated by low-frequency energy, with periods ranging from 10–100 days. This band of variability will be referred to as the eddy field. One of the dominant signals in the eddy field is the presence of topographic Rossby waves in the deeper records, especially on the inshore side of the Gulf Stream (see *e.g.*, Thompson, 1971; Luyten, 1977; Thompson, 1977; Hogg, 1981). Radiation of the planetary waves away from the Stream (to the north), and a southwestward phase velocity, is surmised from the polarization properties of the variability field. In the region north of the Stream, this implies a negative momentum flux. South of the Stream, there is less observational evidence of topographic Rossby waves. Thompson (1978) and Hogg (1981) point out that these bottom trapped motions may force deep countercurrents on either side of the Stream. Bower and Hogg (1992) suggest that the energy source for these high-energy velocity fluctuations may derive from the coupling of westward propagating Rossby waves with a time dependent, eastward-propagating meander field.

The Gulf Stream and its instability have been investigated for some time. Meanders, which dominate the lateral displacement of the Gulf Stream, play an integral role in the evolution of the Stream. They generally propagate eastward with the mean current. If considered solely as steady propagating features, they cannot escape the Stream and couple to westward migrating Rossby waves (Talley, 1982a; 1982b; Pedlosky, 1977; Hogg, 1988). Recently, however, several scenarios have been proposed which allow energy to escape the Gulf Stream under certain realizable circumstances. The salient feature is that the Gulf Stream meandering must be transient, incorporating both the stochastic growth and decay of meandering events, to produce radiation away from the Stream. The excited Rossby waves are then able

to propagate away from the axis of the Stream. Evidence to support this hypothesis has been provided by Hogg (1988) and Malanotte-Rizzoli *et al.* (1992).

Two previous experiments [Local Dynamics Experiment (LDE) at 30°N, 69°30'W and Polymode Array 2 at 36°N, 55°W] have looked in some detail at the dynamics of the southern recirculation gyre. The LDE current meter moorings were situated about 500 km from the axis of the Gulf Stream, and somewhat in the far-field region of the Stream. Polymode Array 2 current meter moorings were positioned roughly 300 km south of the Gulf Stream axis. By conducting a detailed energy analysis of the LDE current meter data, Bryden (1982) finds that the eddies lose energy in their interaction with the mean flow, but they do not locally feed energy into the kinetic energy of the mean flow. In both experiments, eddies were found to gain energy by converting available potential energy contained in the large-scale flow into eddy energy (Bryden, 1982 and Hogg, 1985). From the Polymode data set, Hogg (1983) finds that both lateral and vertical momentum fluxes are important in driving the recirculation gyre, with the vertical flux dominating the lateral flux in the region just south of the Gulf Stream axis. The results are somewhat speculative owing to large uncertainties in the estimates of the fluxes.

Most of our understanding of the dynamics and variability of the southern recirculation gyre to date has derived from the analysis of current meter data and numerical modeling studies. These efforts are still continuing. During the latter half of the 1980s, a large-scale field experiment focusing on much of the Gulf Stream System was conducted. The observational program, commonly referred to as SYNOP (SYNOptic Ocean Prediction), consisted of three arrays — an inlet array located off the coast of Cape Hatteras, a central array situated at 67°W, and an eastern array positioned at 55°W. One of the primary goals of the overall experiment was

to investigate the energetics, dynamics and variability of the Gulf Stream at various sections across its path. To address this issue, both moored current meters and a pentagonal array of acoustic tomography transceivers were situated in the eastern array. The tomographic transceivers were situated in the southern portion of the eastern array, centered at 38°N , 55°W , in the vicinity of the southernmost current meter moorings. This is a site located roughly 100 km south of the axis of the Gulf Stream. The tomographic instruments were purposely moored near current meter moorings to allow for a full comparison of results deriving from the two measurement systems. The inclusion of the acoustic array was intended not only for purposes of validation of the tomographic measurement, but more importantly to demonstrate the utility of acoustic tomography in an energetic mesoscale region. This thesis focuses on the investigation of the structure, energetics, variability, and dynamics of the southern recirculation gyre at 55°W using an array of tomographic instruments.

1.3 Novel Aspects of Thesis

The crux of this thesis is an attempt to fill in some of the important gaps in our understanding of the physics of the western boundary current near-field region. The region of focus is situated at the northern reaches of the Gulf Stream southern recirculation gyre at 55°W , in a region of extremely energetic variability. At present, there is only rudimentary observational knowledge of even the grossest features of these regions. To this end, we investigate the structure, energetics, variability, and dynamics of the southern recirculation gyre.

The primary purposes of this thesis are twofold:

- The first objective is to investigate the structure, energetics, variability, and dynamics of the Gulf Stream southern recirculation gyre. The mean and variability fields are estimated using a 300-day data record. Statistics of the region are estimated and used to discuss the eddy/wave mean-flow interaction issue. A thorough understanding of the role of eddies in transporting physical properties, such as momentum, heat, energy, and vorticity, through the oceanic medium is necessary to examine this interaction.
- An ancillary objective is to address the accuracy and reliability of the tomographic measurement. The present analysis aids in the validation of the tomographic measurement. An important contribution of this thesis is a close comparison of the tomographic measurement with contemporaneous current meter measurements.

The new results contributed by the thesis are the following. The structure and variability of the southern recirculation region are estimated with good vertical resolution over a 300-day period. The variability of the region, with striking evidence of cold-core rings, is seen quite clearly in temperature and relative vorticity time series. The vertical resolution is greater than has been available previously. The observational base prior to this experiment consisted mostly of a few current meters in the vertical at isolated points and point CTD measurements.

The integrating nature of the tomographic measurements is used to measure the large-scale properties of the field in this highly energetic region. Thus, heat and momentum fluxes are more representative of the large-scale field than of a single point. One of the most interesting results of the thesis is the direct estimate

of relative vorticity over regions of roughly 10,000 square kilometers. Using the circulation around the periphery of an enclosed region, the areal-averaged vorticity is simply obtained using Stokes' theorem. In the region of study, relative vorticity can prove unambiguously the presence and/or passage of cyclonic, cold-core rings that may not be detectable with other measurements, especially if the infrared imagery is not available or the ring has shed its surface signature. This direct measurement of vorticity also has errors much smaller than those obtained from previous observations. Most previous attempts at estimating vorticity required the differentiation of the field with point measurements typically of the order of 100 km apart. The errors in that type of calculation are quite large, owing in large part to the finite differencing of the measurements.

Second-order statistics, such as heat and momentum fluxes, are also calculated for the array, and their significance is discussed. Utilizing the estimated statistics, an investigation of wave radiation from the Gulf Stream is presented. The Eliassen-Palm flux diagnostic, which is more commonly utilized in atmospheric literature, has been applied to the problem of wave radiation from the Gulf Stream. The result of this diagnostic suggests the Gulf Stream as the source of energy in the gyre far field.

Complementary to the physical issues mentioned above is a comparison of tomographic measurement with current meter measurements and numerical model output. This thesis also contains the first significant attempt to estimate second-order statistics with tomographic measurements.

The significance of the forementioned results rests primarily in the implication of the Gulf Stream as a main source of energy for eddies in the gyre interior.

In addition, a higher resolution view of the mean and variability field is quite important. The parameterization of eddies, especially with regard to their spatial and temporal scales, is important for comparison with numerical models. We will never have enough measurements to look at all of the details of the region. Thus, we use models to further our knowledge of the important dynamical balances. The importance of adequately describing the variability field in the region cannot be overemphasized as this field is directly coupled to the Gulf Stream, and acts as a source of energy in actually driving the mean flow.

1.4 Thesis Overview

The thesis is divided into six chapters. The 1988/1989 SYNOP Gulf Stream tomography experiment is the subject of Chapter 2. To put the experiment in perspective, an overview of the oceanography of the southern recirculation gyre is given. A discussion of the experiment follows, and available concurrent data is presented.

Chapter 3 focuses on the tomographic measurement. A brief background of the tomographic measurement is given. The tomographic measurement naturally divides into two separate pieces — the forward problem of modelling acoustic propagation in the ocean environment, and the inverse problem of using tomographic data to infer information about the intervening oceanic medium. The acoustic forward problem is discussed first. The methodology for inverting the acoustic data is then provided. The acoustic propagation of the region in the context of ray theory is then considered. Next, the processed acoustic data is presented. As the error treatment in tomography is somewhat specialized, a thorough discussion of

the errors inherent in the tomographic measurement is given. The reader who is not interested in these technical details can simply read the introduction and discussion sections to obtain an adequate background, and skip the remainder of the chapter.

The results of the inverse analysis of the tomographic data set are the subject of Chapter 4. The ocean model adopted for the present analysis is introduced. Vertical slices of temperature, current velocity, and vorticity are provided, and a complete discussion of the oceanographic field follows. Also presented are spectra for these quantities. A comparison with current meter data and output from a quasigeostrophic numerical model is also given.

Chapter 5 focuses on the statistics and dynamics of the southern recirculation gyre. Second-order statistics, such as heat and momentum fluxes are presented. A description of the energetics of the region is also given. An analysis of wave/mean-flow interaction properties of the region is conducted using the generalized Eliassen-Palm flux vectors. Implications for wave radiation from the Stream to the far field follow.

Finally, a summary and discussion of the results presented in the treatise are provided in Chapter 6. The key insights gained into the physics of the western boundary current near field are summarized and discussed. A few suggestions for future experimental endeavors are also provided.

Chapter 2. The 1988/1989 SYNOP Gulf Stream Tomography Experiment

2.1 Oceanographic Setting

Before proceeding to a description of the SYNOP tomography experiment, a broadbrush overview of the hydrography of the region of interest is given. The tomographic array was situated at 38°N , 55°W , in the western North Atlantic. Figure 2.1 shows a map of the western North Atlantic, with the mean axis of the Gulf Stream superposed. As the Gulf Stream flows offshore from Cape Hatteras, it follows a predominantly easterly path. In the region of 60°W to 65°W , the Stream encounters the New England Seamount Chain, which rises from the seafloor to a height of roughly 2500 m beneath the ocean surface. In this region, and further downstream, the Gulf Stream becomes a much more sinuous current. Large-amplitude meandering of the Stream and the generation of rings are commonplace.

The Gulf Stream region is a highly energetic area, as can be seen in the surface mean flow kinetic energy and eddy kinetic energy maps shown in Figure 2.2. Ship-drift estimates averaged over 1° squares were used in the calculation of the surface kinetic energies (see Wyrski *et al.*, 1976). The estimates are subject to large observational errors and smoothing problems, but the general picture persists. Most of the surface kinetic energy, both in the mean flow and in the eddy field, is confined to the western boundary region, and decays away from the strong current. More recent views of the energetic variability of the Gulf Stream region are provided in Figures 2.3 and 2.4. Figure 2.3 shows the rms variability of the sea level obtained from 32 months of altimetric measurements (Stammer and Böning,

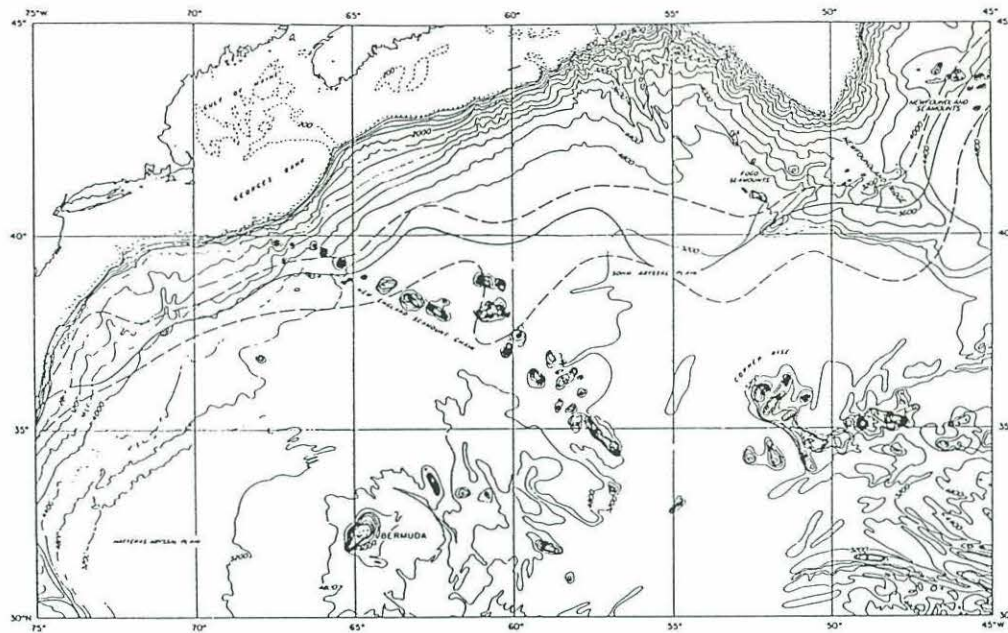


Figure 2.1: Map of the western North Atlantic, adapted from Hogg *et al.*, (1986). The solid curve depicts the mean position of the Gulf Stream (as defined by the 15° isotherm at 200 m), from Fisher (1977). The 15° isotherm is found between the dashed curves 50% of the time.

1992). Figure 2.4 shows the horizontal distribution of eddy kinetic energy at 700 m depth calculated from SOFAR float data (Owens, 1991). A similar distribution is seen in the eddy potential energy field, based on the vertical displacement of the thermocline, where again the largest energy densities are associated with the Gulf Stream region (Dantzler, 1977). Vertical profiles of zonal velocity and eddy kinetic energy along 55°W, derived from measurements made with drifting buoys, SOFAR floats, and current meters (Richardson, 1985), are given in Figure 2.5. Throughout the water column, eddy kinetic energy is concentrated about the axis of the Gulf Stream, and diminishes latitudinally away from the strong current. Eddy energy is greatest in the near surface regions of the Gulf Stream, and decays vertically as the Stream itself becomes weaker.

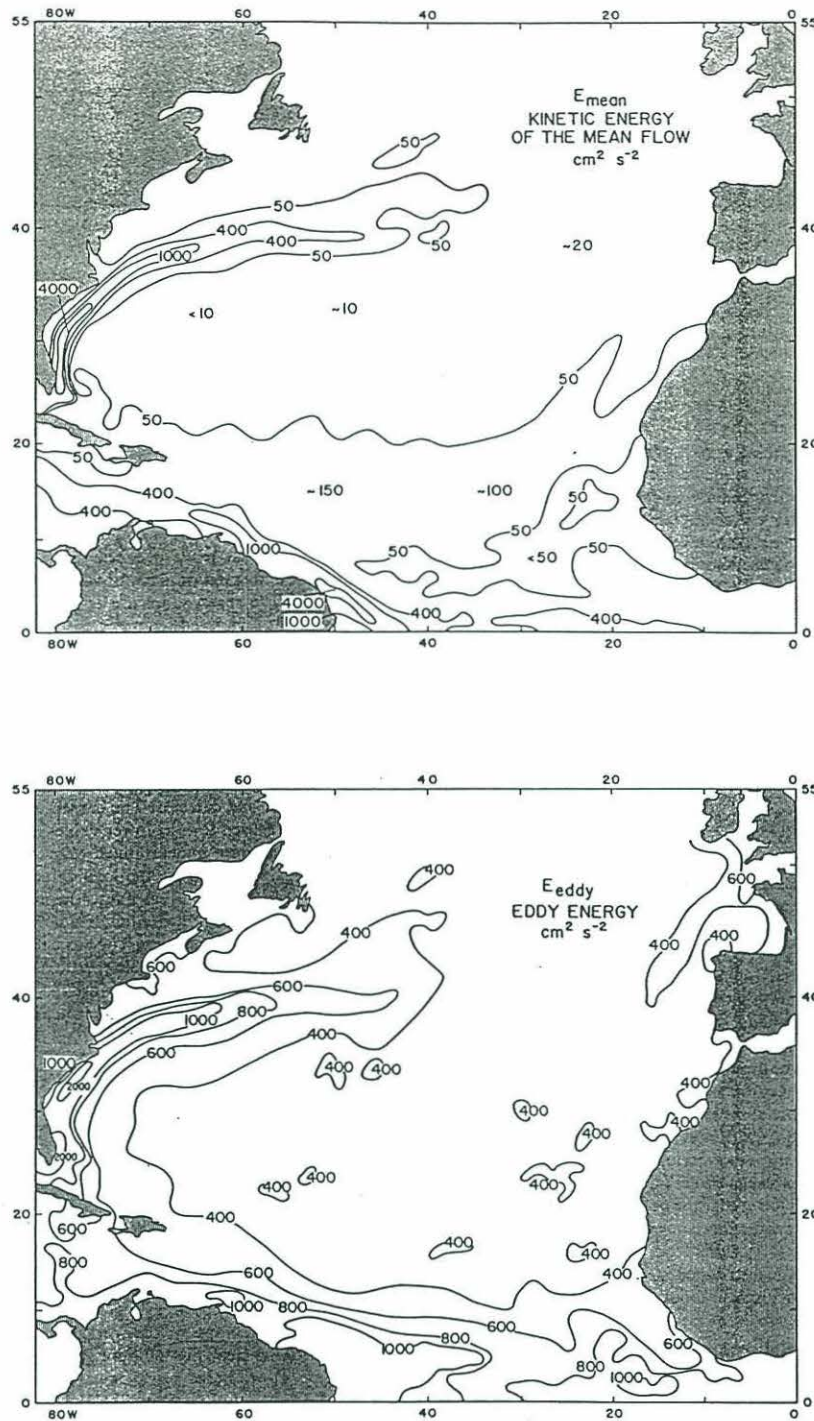


Figure 2.2: (top) Kinetic energy per unit mass of the mean flow for the North Atlantic Ocean based on 1° square averages, from Wyrтки *et al.*, (1976). (bottom) Eddy kinetic energy per unit mass for the North Atlantic base on 1° square averages, from Wyrтки *et al.*, (1976).

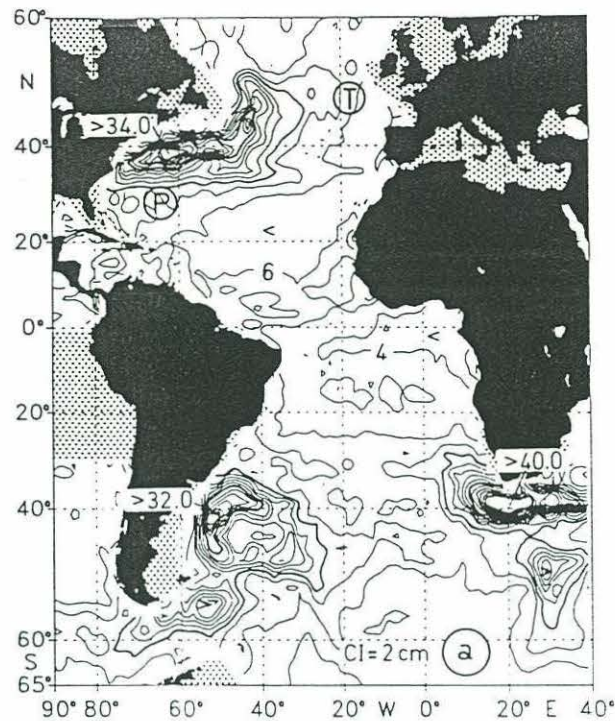


Figure 2.3: Rms sea surface variability determined from Geosat altimeter measurements from 32 months of data, from Stammer and Böning, (1992).

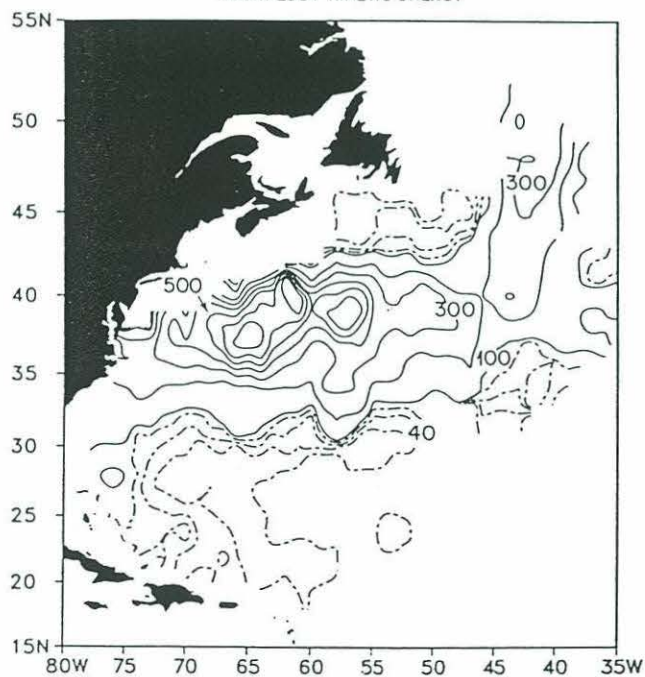


Figure 2.4: Horizontal distribution of eddy kinetic energy at 700 m depth in the western North Atlantic, calculated from SOFAR floats, from Owens, (1991).

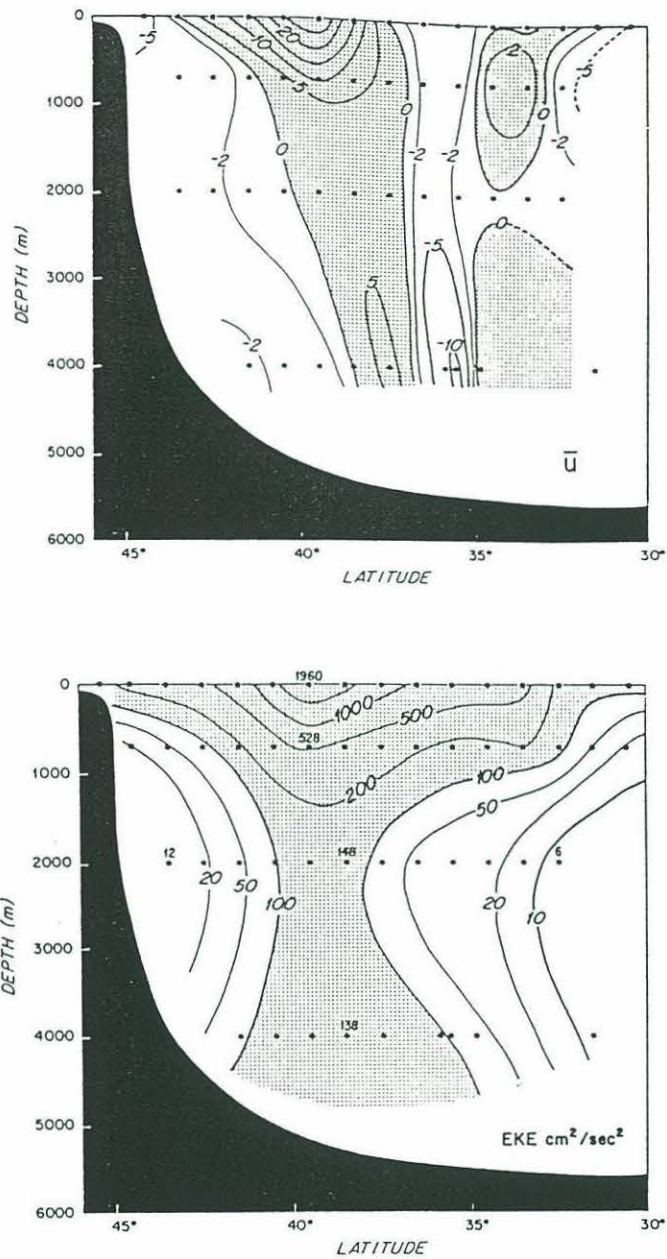


Figure 2.5: (top) Contoured zonal velocity section (cm s^{-1}) along 55°W and through the Gulf Stream from drifters, floats, and current meters, from Richardson (1985). Eastward velocity is shaded. (bottom) Contoured section along 55°W of eddy kinetic energy (per unit mass), from Richardson (1985). Units are $\text{cm}^2 \text{s}^{-2}$. High eddy kinetic energy and its gradient coincide with the mean Gulf Stream and bounding countercurrents.

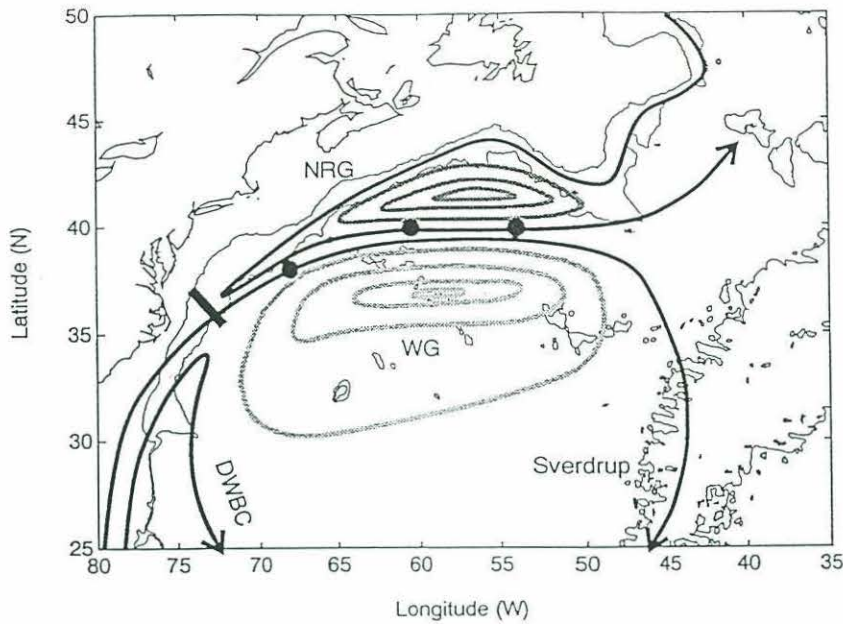


Figure 2.6: A scheme for the total transport in the western North Atlantic, from Hogg (1992). Each contour is approximately 15 Sverdrups. WG = Worthington Gyre (southern recirculation gyre), NRG = northern recirculation gyre, DWBC = Deep Western Boundary Current, and Sverdrup = wind driven interior.

A close inspection of Figure 2.5a shows an eastward flowing Gulf Stream flanked to the north and south by countercurrents. The countercurrents have weaker velocities than the Stream itself, but are nevertheless evident. One of the earliest suggestions of the presence of a southern countercurrent was provided by Worthington (1976). Using simple water mass and property arguments, Worthington surmised the existence of a southern recirculation gyre. The southern recirculation gyre acts to transport Gulf Stream water, which has been expelled to the south of the Stream, to the west and back into the Gulf Stream itself upstream of the seamounts. The recirculation leads to the downstream enhancement of the Gulf Stream transport which has been seen in many recent observations. A schematic of the Gulf Stream System, as suggested by Hogg (1992a), is shown in Figure 2.6. This figure is based on long-term velocity measurements throughout the region.

Strong recirculation gyres, both to the north and south of the Stream, are evident in Figure 2.6.

The physical oceanography of the southern recirculation gyre in the region just south of the Gulf Stream axis is dominated by the Gulf Stream and its variability. A representative description of the region, in terms of velocity and temperature time series, is shown in Figures 2.7 and 2.8. The data used for these two figures were obtained during the Polymode Array 2 Experiment. Both records were obtained from a mooring positioned at $37^{\circ}30'N$, $55^{\circ}W$. The passage of several energetic events is obvious in both the temperature and velocity records, particularly in July and November of 1975, and in February of 1976. The vertical coherence of the records is quite striking. A representation of the vertical structure with a barotropic mode and a surface intensified baroclinic mode captures most of the energy of the records. Temporal variability is dominated by mesoscale periodicities, of the order of one to two months.

The northern portion of the southern recirculation gyre is directly coupled with the large-amplitude meandering of the Gulf Stream. The genesis, growth, and expulsion of cold-core rings from the Gulf Stream are common occurrences in this near-field region. The subsequent westward propagation of cold-core rings dominates much of the variability in this part of the recirculation.

This section has purposely been descriptive in nature, focusing on the southern recirculation gyre. A more detailed characterization of the region, including a statistical description of the experimental site, will follow when the inverse results are discussed in Chapters 4 and 5 of the thesis.

POLYMODE 8 MOORINGS 564 - 577 - 606 CURRENT VECTORS

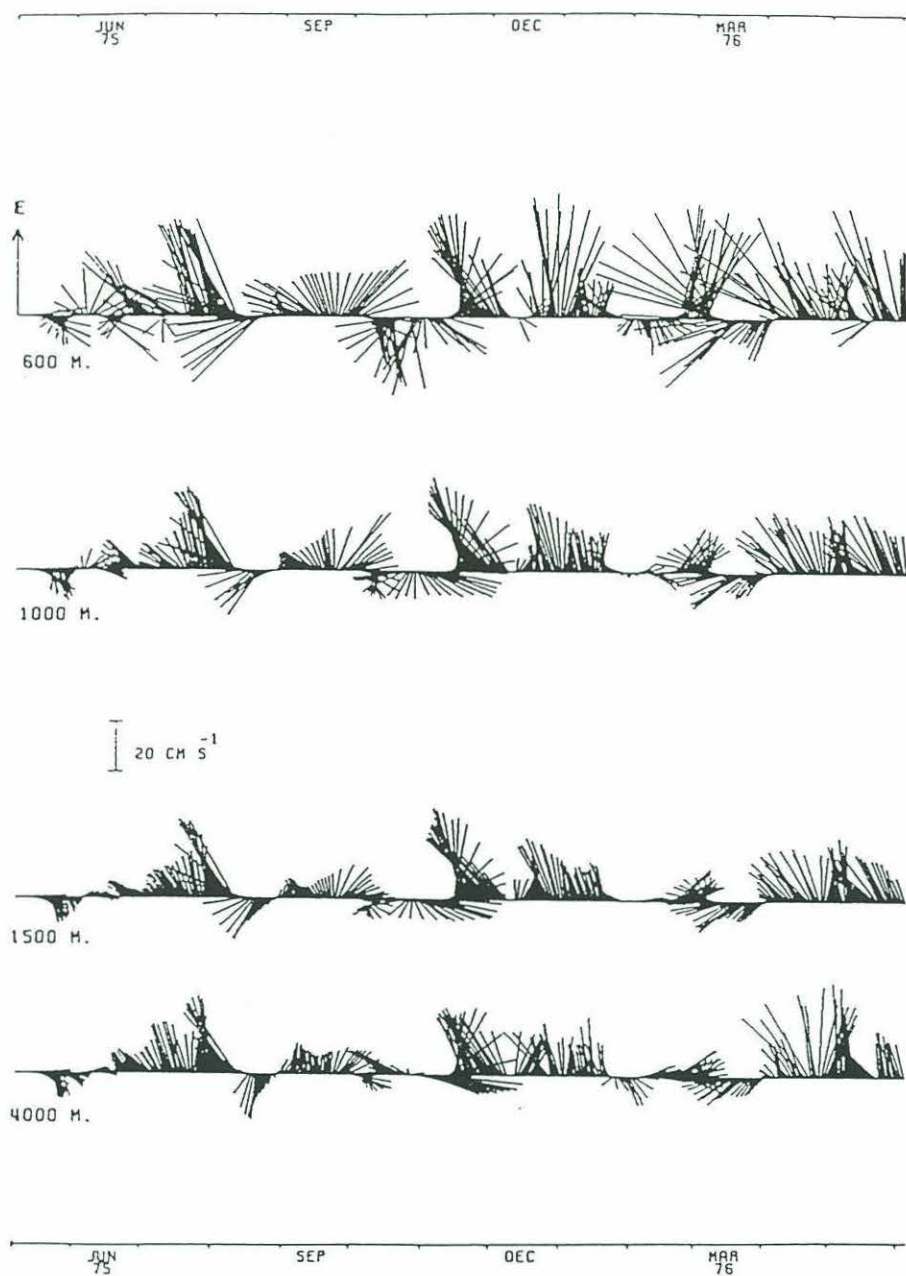


Figure 2.7: Velocity stick plot time series for mooring 8 of Polymode Array 2, from Tarbell *et al.* (1978).

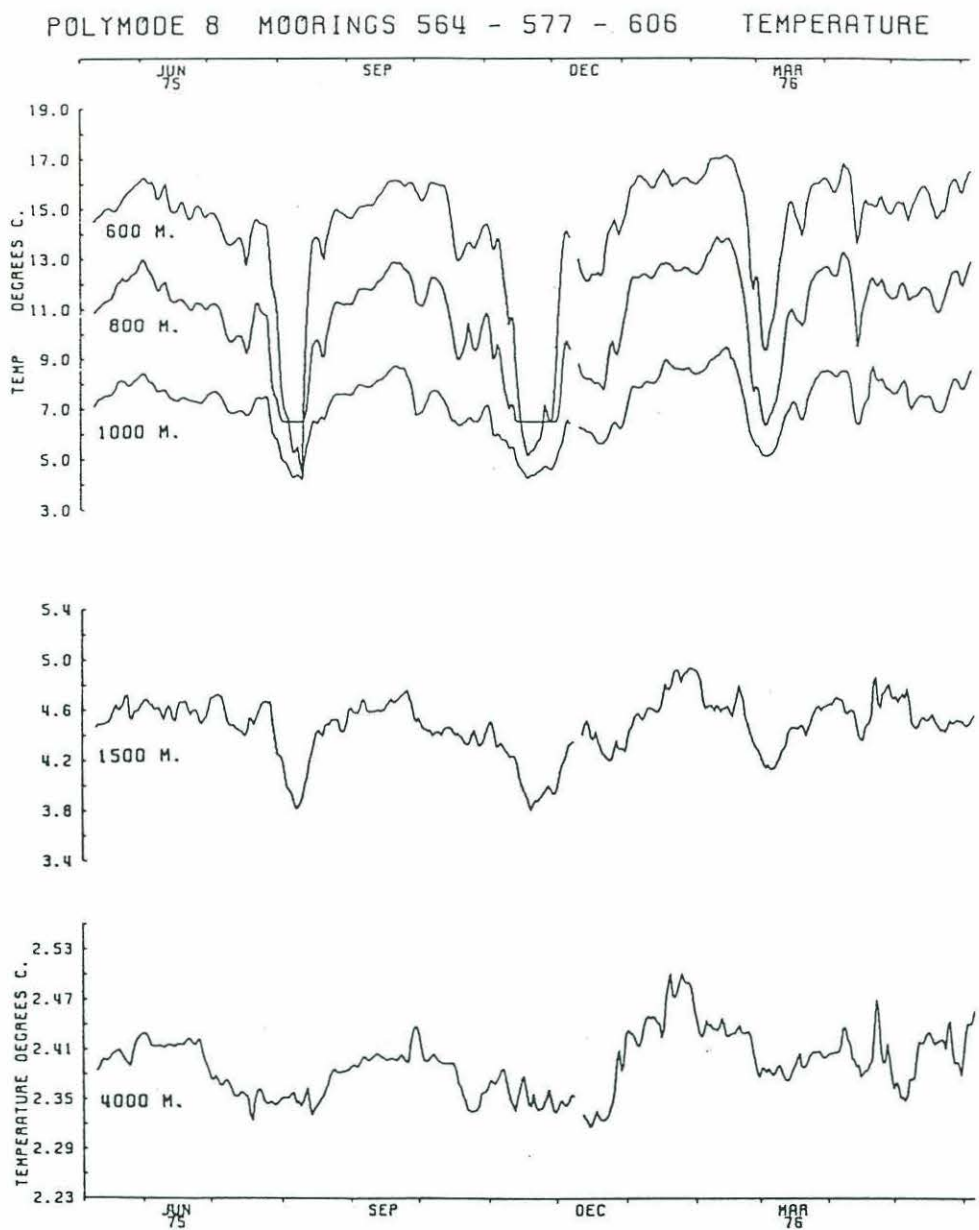


Figure 2.8: Temperature time series for mooring 8 of Polymode Array 2, from Tarbell *et al.* (1978).

2.2 Experimental Design

The Gulf Stream tomography experiment was one component of the SYNOP (Synoptic Ocean Prediction) observational program. The focus of SYNOP was directed at an enhanced understanding of the structure, variability, energetics and dynamics of the Gulf Stream System. In an effort to achieve this goal, three separate arrays of instruments were situated across the path of the Gulf Stream — an inlet array located off of the coast of Cape Hatteras, a central array straddling the Gulf Stream at 67°W, and an eastern array positioned at 55°W. A variety of instrumentation was utilized in the overall experiment, including CTDs, expendable bathythermographs, acoustic doppler current profilers, moored current meters, inverted echo sounders, RAFOS lagrangian drifters and acoustic tomography transceivers. We will primarily focus on the tomographic contribution to SYNOP.

The 1988/1989 Gulf Stream SYNOP acoustic tomography experiment consisted of a pentagonal array of transceivers (with units acting as both sources and receivers) centered at approximately 37°N, 55°W in the northern portion of the Gulf Stream southern recirculation gyre. The exact locations of the five moorings, along with contemporaneous current meter moorings, are displayed in Figure 2.9. Three transceivers were also deployed by the French group at IFREMER (led by Yves Desaubies) as part of the array, but will not be considered due to instrument failure. The tomographic moorings were deployed in October of 1988 and retrieved in August of 1989. All five transceivers were moored at a depth within 200 m of the sound channel axis, which is typically found at roughly 1200 m depth in this region. The sound channel axis is at a depth of nearly 4000 m above the seafloor of the Sohm Abyssal Plain, with a depth of 5300 m. The distances between the

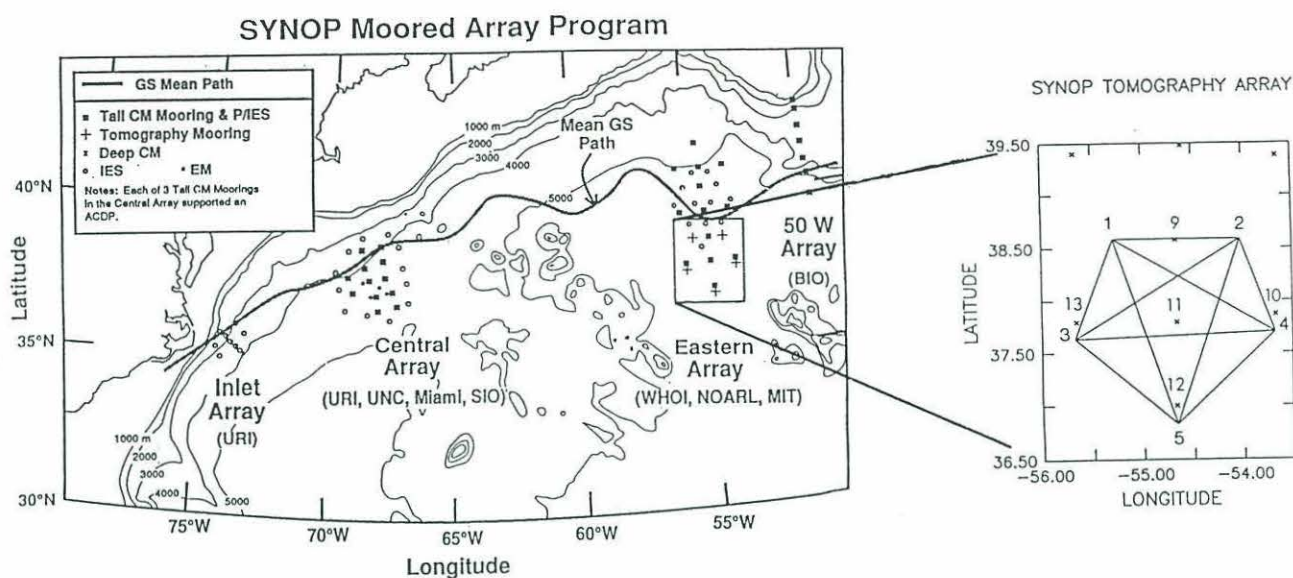


Figure 2.9: Observational plan of the SYNoptic Ocean Prediction Experiment (SYNOP), adapted from Shay and Bane (1992). A blowup of the southern portion of the eastern array, of which the tomographic array was one component, is illustrated to the right of the full plan. The location of contemporaneous current meter moorings are also included and labeled with small crosses.

instruments varied from 110 km along the periphery of the array to 203 km across the array. Instrument locations and dates of operation are given in Table 2.1

For the SYNOP tomography experiment, 400 Hz MIT/WHOI/Webb tomography sources were used. Good descriptions of the signal design and processing for the tomographic systems can be found in Spindel (1985) and Metzger (1983). A detailed description of the instrumental characteristics is provided for the interested reader. The source level for the MIT/WHOI/Webb tomography instruments was approximately 180 db re 1 μ Pa at 1 m (see Boutin *et al.*, 1989 and Chester *et al.*, unpublished manuscript). The transmitted signal consisted of a phase-encoded linear maximal pseudorandom sequence. For practical purposes, the signal may be thought of as a coded sequence of digits which exhibit pulse-like characteristics upon reception and cross correlation. The carrier frequency was 400 Hz. Pre-

Table 2.1: Instrument Locations

Mooring #	Latitude	Longitude	Depth (m)	Days of Operation
1	38°35.20'N	55°17.65'W	1073	Oct 24, 1988 – Aug 20, 1989
2	38°35.18'N	54°01.67'W	1173	Oct 24, 1988 – Aug 19, 1989
3	37°38.07'N	55°40.62'W	1172	Oct 24, 1988 – Aug 13, 1989
4	37°42.18'N	53°40.62'W	1294	Oct 24, 1988 – Aug 17, 1989
5	36°49.64'N	54°39.85'W	1071	Oct 24, 1988 – Aug 15, 1989

and post-deployment testing of the sources (Boutin *et al.*, 1989 and Chester *et al.*, unpublished manuscript) indicate that the effective bandwidth is approximately 100 Hz. Periodic pulses are transmitted and coherently averaged at the receiver to boost the signal to noise ratio. The repetition period of the transmitted signal (5.11 s) was greater than the total spread of multipath arrivals (typically 1–2 s, depending on range), so no ambiguity of arrivals occurred upon reception. A summary of the signal parameters for the SYNOP tomography experiment is given in Table 2.2.

Owing to the constraints of battery power (to energize the sources), tape capacity (to store the acoustic receptions), and the need to filter out high-frequency motion (tides and internal waves), the sampling scheme consisted of six transmissions per day, every four hours, every other day. The transmission schedule com-

Table 2.2: Signal Parameters

Carrier frequency	400 Hz
Bandwidth	100 Hz
Digits	511
Digit duration	0.01 s
Sequence duration	5.11 s
Repetitions	38 (3.24 min)

menced on October 24, 1988 (0000 UTC, or time 0) with unit 1 transmitting (for 3.41 minutes) to units 2–5, which received and processed the signal. Fifteen minutes later, unit 2 transmits to units 1 and 3–5. The time delay is necessary to allow for signal propagation and processing of the received signal. Fifteen minutes later (or 30 minutes from time 0), unit 3 transmits to units 1–2 and 4–5; 15 minutes later (or 45 minutes from time 0), unit 4 transmits to units 1–3 and 5; 15 minutes later (or 60 minutes from time 0), unit 5 transmits to units 1–4. The full transmission schedule, for all five instruments to transmit and listen to each other, lasted about one hour. The instruments then wait until the beginning of the next scheduled transmission, a wait period of approximately three hours, and then repeat the cycle.

Two important issues concerning the acoustic transmissions should be mentioned at this point. Firstly, it is assumed that there is little oceanic variability over the duration of the transmission, which lasts 3.41 minutes. Estimates of the signal decorrelation time scale are hard to obtain, but the minimum time scale resulting from internal wave scattering is generally considered to be 3–5 minutes (see Flatté *et al.*, 1979). Secondly, note that the time separating reciprocal transmissions varies from approximately 15 minutes to approximately 1 hour, depending upon which pair of transceivers is being considered. Thus reciprocal records do not contain truly reciprocal transmissions. However, the data show that the receptions are approximately reciprocal. More on this matter will follow in the discussion of the processed data set and the errors in the tomographic travel time measurement.

The receiving end of the system is now considered. The signal acquisition is initiated by the system controller at preset times, determined by adding the preprogrammed propagation delays to the source transmit times. Immediately prior to reception of the transmitted signal, the hydrophone is used to make an ambient noise measurement. A discussion of the ambient noise measurement is provided in Appendix A. The *in situ* calculation of ambient noise is performed in order to adjust the variable gain of the hydrophone preamplifier, to prevent the saturation of the receiver while sampling the signal. The receiver then processes 38 of the 40 transmitted sequences. The first and last sequences are chopped to avoid end effects. The received signals are amplified and bandpass filtered, then sampled at four times the carrier frequency.

To compress the received signal, complex demodulates are formed from the sampled receptions. Complex demodulation is simply a pulse compressing summation process. The demodulates are coherently averaged with subsequent se-

quences (summing 38 sequences, or the full 3.24-minute period), yielding a record of 1022 complex demodulate pairs (or 2044 demodulates). The demodulate pairs are then stored internally on data tapes. Correlation with a replica of the transmitted linear maximal pseudorandom sequence was not performed *in situ*. Also recorded internally are scientific measurements (external pressure, temperature), engineering measurements (such as variable gain setting and rms current input level to the digitizer), and various header information.

Upon returning to shore, the received signal was cross correlated with a replica of the transmitted pseudorandom sequence. The stored demodulates are converted to floating point arithmetic values, demeaned, and intensities are calculated by squaring the real and imaginary demodulate components (see Spindel (1985) for details). The result of this operation is a pulse response of 1022 intensities, with a sampling interval of 5 ms ($5.11 \text{ s} / 1022 \text{ samples}$). The same procedure was applied to all of the records.

The SYNOP tomography experiment generated a 300-day data set (more exactly, 150 days of bi-daily data due to the every-other-day transmission schedule), of reciprocal transmissions for all five instruments. This amounts to twenty individual pulse response records, or ten sets of reciprocal pulse response records. Unfortunately, the receiving end of one of the transceivers (mooring 1) malfunctioned for the majority of the experimental period. The exact cause of the malfunction is not completely understood at this time, but appears to be due to a strumming of the mooring which is excited by strong flows past the mooring. A detailed examination of the processed data is provided in Section 3.5.

2.3 Environmental Data

The tomographic experiment occurred simultaneously with the SYNOP program. A subsurface moored array of current meters was maintained in the immediate vicinity of the tomographic array for the entire duration of the experiment. Direct measurements of current velocities and temperature at several depths in the water column were recorded. The most instrumented levels were nominally 500 m and 4000 m, with a few moorings having instruments at 250 m, 1000 m, and 1500 m. Sample velocity stick plot and temperature time series are illustrated in Figures 2.10 and 2.11. The data in these records were obtained from a mooring situated in the center of the tomographic array. The structure and temporal variability of these records are quite similar to the Polymode Array 2 records presented in the first section of this chapter. Current meter records like those depicted in Figures 2.7 and 2.10 are available for all of the moorings in the tomographic region (see Figure 2.9 for a plan view of the mooring locations). The velocities of the northernmost moorings (north of 38°N) are more energetic in nature and have a tendency toward eastward flow, due to their proximity to the Gulf Stream. The moorings further to the south (south of 38°N) are located in a region of lower mean velocities and less energetic variability.

Satellite infrared imagery of the region is also available. The sea surface temperature maps are quite valuable in determining the location of the Gulf Stream and cold-core rings relative to the tomographic array. During the ten-month duration of the experiment, the infrared maps suggest that the Gulf Stream may have passed over the very northern portion of the array possibly once, at the outset of the experiment. The remainder of the experiment the array was situated on average

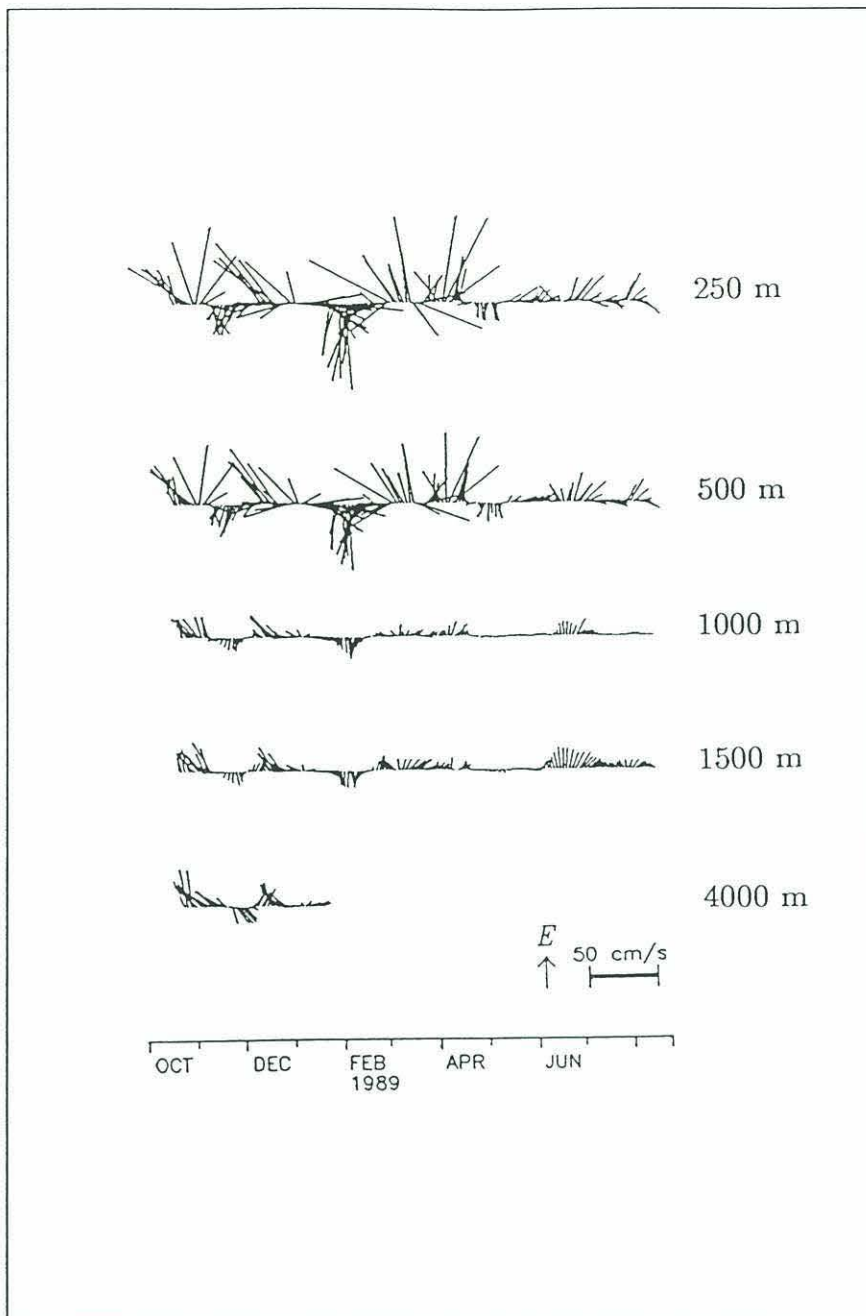


Figure 2.10: Velocity stick plot time series for current meter mooring 11 of the eastern array. Mooring 11 is located in the center of the tomographic array, at 37°48'N, 54°40'W.

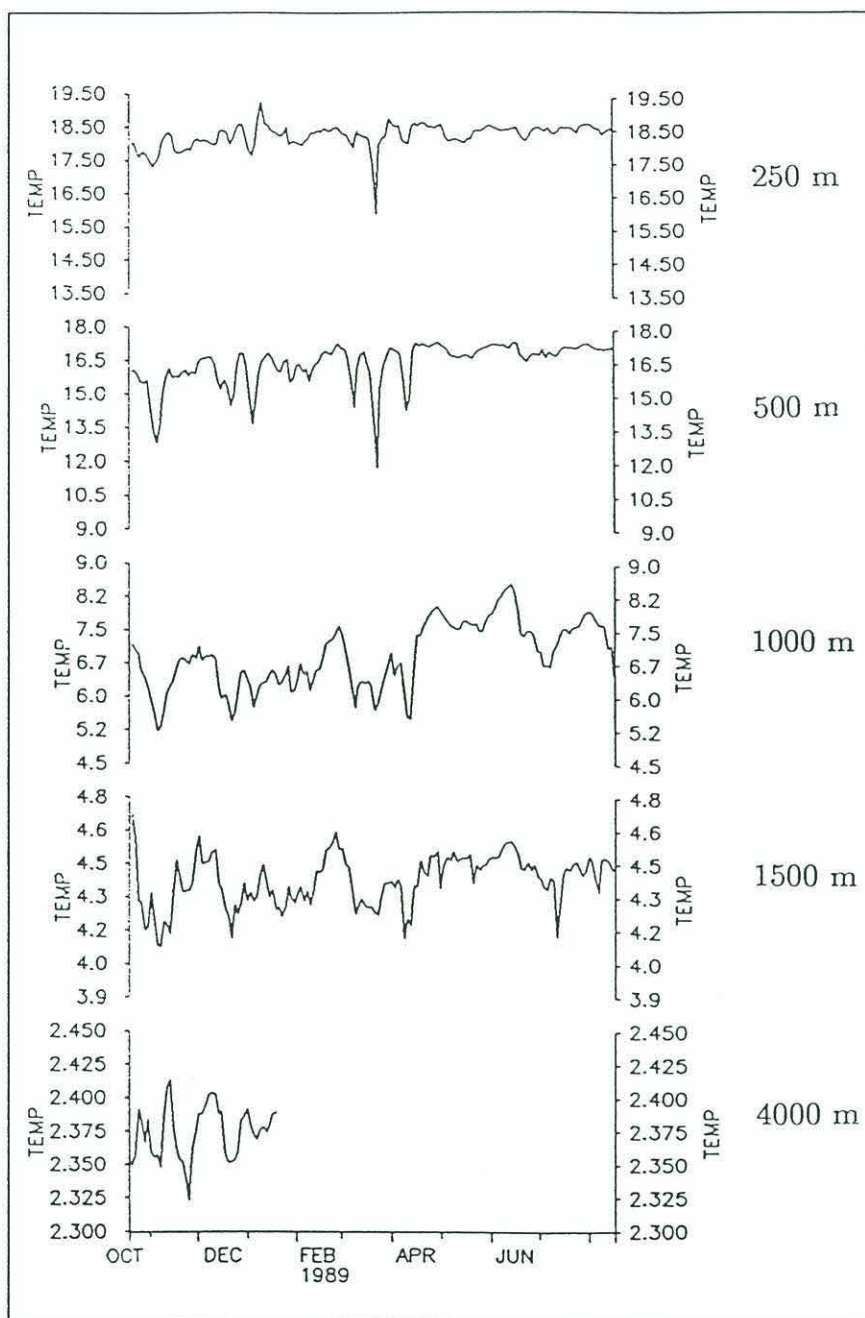


Figure 2.11: Temperature time series for current meter mooring 11 of the eastern array. Mooring 11 is located in the center of the tomographic array, at $37^{\circ}48'N$, $54^{\circ}40'W$.

about 100 km south of the axis of the Gulf Stream axis. However, westward translating cold-core rings propagated through the array during much of the experiment. CTD stations were also made during the deployment and retrieval of the array. The profiles obtained were quite similar to climatological profiles of the region, with the exception of a seasonal thermocline in the upper 250 m.

The tomographic instruments made temperature and pressure measurements at the depth of the transceivers. These measurements are useful. No tracking of the transceiver position or tilt was maintained during the experiment. Acoustic tracking of the instruments adds to the complexity and expense of the instrument, and it was anticipated that mooring motion could be eliminated by other means, such as through the inverse procedure. The mooring motion turns out, not unexpectedly, to be a large noise signal in the acoustic arrival time data, but it can largely be removed from the acoustic signal. The procedure used in this analysis to deal with the mooring motion, and its effect on travel time arrivals, will be discussed in the next chapter.

A detailed discussion of the concurrent local data will be presented in comparison with the inverse results in Chapters 4 and 5.

Chapter 3. Formulation of the Tomographic Inverse Problem

3.1 Introduction

As ocean acoustic tomography is still a relatively novel measurement system, part of this thesis will address issues which one may deem more of a technical nature. For the reader interested solely in the oceanographic results, the background provided in this introductory section should be adequate to proceed. Sections 3.2 through 3.6 are more technical in nature and may be skipped without loss of continuity.

The technology of acoustic tomography is now nearly fifteen years old. Due to the slow evolution of oceanographic instrumentation, and the complexity of the tomographic systems, tomographic sensors are not yet off-the-shelf instruments, as are the CTD and current meter. The principles of ocean acoustic tomography were originally described by Munk and Wunsch in 1979. By measuring the travel time of acoustic energy between two (or more) instruments, the sound speed structure for the intervening medium can be estimated through the inversion of the acoustic travel-time data. With reciprocal transmissions the velocity of the water in the plane connecting the two instruments can be measured. With an array of three or more instruments, the sing-around travel times along the periphery of a closed region can be used to estimate the areal-averaged relative vorticity via Stokes' theorem. Two advantages of the tomographic measurement over spot measurements are the geometric increase of information with each additional instrument deployed, and the spatial integration inherent in the measurement.

Previous tomographic experiments have given present-day practitioners the confidence in the method (see Spindel and Worcester, 1991 for a listing of all of the major tomographic experiments to date). The earliest tomographic efforts (*e.g.*, Spiesberger *et al.*, 1980 and The Ocean Tomography Group, 1982) were primarily tests of the instrumentation and acoustic transmission in the ocean, performing relatively crude mapping of the mesoscale sound speed field. Over the last decade the instrumentation has advanced to a state which is more adequate to address the original intent. Several experiments have demonstrated the success of acoustic tomography in monitoring the oceanic temperature field, current velocities, and vorticity field (*e.g.*, Howe *et al.*, 1987; ; Ko *et al.*, 1989; Chester *et al.*, 1991; Howe *et al.*, 1991; Spiesberger and Metzger, 1991; Worcester *et al.*, 1991;). Recent tomographic programs illustrate the evolution and versatility of the tomographic measurement. An experiment in the Greenland Sea investigated deep water formation in the Marginal Ice Zone (The Greenland Sea Tomography Group, unpublished manuscript). A moving ship tomography experiment in the southwest North Atlantic was conducted to assess the spatial resolution attainable over a large portion of the subtropical gyre (The Applied Tomography Experiment Group, 1991). The issue of global warming is also being addressed using trans-oceanic acoustic transmissions and the tomographic methodology (Munk and Forbes, 1989).

The goal of ocean acoustic tomography is to infer the structure of the oceanic medium by measuring properties of acoustic propagation through the ocean. Acoustic propagation is affected by variability of the sound speed and current fields. Many oceanographic processes are responsible for this, including mesoscale fluctuations, internal waves, and tides. Perturbations of the ocean sound speed and/or current field lead to changes in acoustic travel times, intensities, phases, and arrival an-

gles. To date, the measurement of acoustic travel time has been the primary datum used for analysis. A tomographic measurement system typically consists of a small array of sources and receivers, with the sources transmitting low-frequency pulses to the receivers. It is often the case that the sources and receivers are co-located, allowing for the reciprocal transmission of sound between instruments. The utility of such an arrangement will be discussed in the next section. The fundamental tomographic observables consist of a set of integrals over acoustic paths throughout the ocean. Thus, unlike conventional point measurement systems, such as a moored array of current meters, the tomographic measure gives a spatially-averaged view of the ocean.

The tomographic reconstruction problem can be separated into the forward problem and the inverse problem. The forward problem describes the dependence of the pulse travel times along a particular set of paths on the sound speed field of the ocean. The inverse problem can be thought of in the following manner: given measurements of arrival times of acoustic rays, and assuming a forward model of acoustic propagation, estimate the interior structure of the sampled medium.

The forward problem is discussed first. Modeling of acoustic propagation in an oceanic waveguide can be attacked in several manners, all of which involve solving the acoustic wave equation. Perhaps the simplest and most physically insightful method is an analysis in terms of acoustic rays, which have a direct analogue in the field of optics. Implicit in this approach is the assumption that the refractive properties of the medium change only slightly over an acoustic wavelength (this is geometrical optics, or the WKB approximation). Snell's law of refraction is the basis of this formulation by which the paths of energy propagation through the medium are explicitly specified. However, ray theory is not an exact solution for

the acoustic wavefield as it does not account for diffraction and other wave effects. Nevertheless, ray theory was used in this analysis as the acoustic rays were resolved in the pulse response data.

Before proceeding, two other theoretical approaches to solving the acoustic wave equation should be mentioned. Normal mode theory gives an exact solution to this wave equation based on the preferred acoustic vibrations (normal modes) of the waveguide. The normal mode picture becomes more complicated when the medium is range-dependent (due to irregular bathymetry and/or strong inhomogeneities such as fronts or eddies), and mode coupling might need to be considered. A second approach, the parabolic equation method, is based, in its simplest form, on the paraxial (small angle) approximation to the wave equation. The result is a model which is very useful for modelling propagation in a range-dependent waveguide, but does not readily yield ray or mode travel times.

The inverse problem is now introduced. The goal of the inverse procedure is to obtain the best possible estimate of the structure of the sampled ocean, using measurements which are noisy and which typically undersample the medium. As will be shown in the following section, the tomographic data can be approximated as linear functions of sound speed perturbations (and hence temperature to a good approximation) and current.

The remainder of this chapter is divided into five sections. Section 3.2 discusses the theory of the forward problem. The inverse problem is considered in Section 3.3. The acoustic propagation of the region in the context of ray theory is provided in Section 3.4. The processed acoustic data is presented in Section 3.5.

The final section is devoted to a discussion of the errors in the tomographic measurement.

3.2 The Forward Problem

The forward problem in acoustic tomography describes the dependence of the pulse travel time along a particular path on the sound speed field of the ocean. The formulation of the forward problem has been treated previously by several authors (see *e.g.* Munk and Wunsch, 1979; Cornuelle, 1983), so only the basic equations are presented here. The travel time T_i along a ray path Γ_i is expressed as

$$T_i(t) = \int_{\Gamma_i} \frac{ds}{c(\mathbf{x}, t) + \mathbf{u}(\mathbf{x}, t) \cdot \boldsymbol{\tau}} \quad , \quad (3.1)$$

where c is the sound speed field, \mathbf{u} is the current vector, s is arc length along the ray, and $\boldsymbol{\tau}$ is a unit vector tangent to the ray. The travel time of a given ray is dependent upon the path length, sound speed, and current velocity along the ray path.

Variations in sound speed and current lead not only to deviations in travel time, but also to changes in the ray path. Acoustic rays satisfy Fermat's principle, which states that the travel time along a ray path is an extremum (see *e.g.*, Officer, 1958). Thus, small perturbations in the ambient sound speed cause first-order changes in travel times, but affect the acoustic path length only through higher order terms. Hamilton *et al.*, (1980) show that there is a negligible change in travel time associated with this change in ray path. It is assumed, usually validly, that the ray path in the perturbed medium is almost identical to that in the unperturbed

medium. One can check the validity of this assumption a posteriori by tracing the ray path in the sound speed field calculated by the inverse, and then comparing with the path traced in the unperturbed medium.

The size of the terms in the denominator of the integrand of (3.1) are now examined more closely. A typical current speed is $u = 25$ cm/s and a typical sound speed is $c = 1500$ m/s, so $u/c = O(10^{-4}) \ll 1$. Typical values for the vertical shear of current and sound speed are $du/dz = 5$ cm/s /100 m = $O(10^{-3})$ and $dc/dz = 5$ m/s/100m = $O(10^{-2})$, so dc/dz is at least one order of magnitude larger than du/dz . This simple scaling analysis shows that the refraction of rays is dominated by the sound speed gradient, and that the current can be ignored in ray tracing simulations. A typical value for a sound speed perturbation δc is 10 m/s (roughly 2°C), so linearization about a reference sound speed field is a good approximation.

After linearization about a reference sound speed field c_o , we obtain

$$\begin{aligned} T_i(t) &= \int_{\Gamma_{oi}} \frac{ds}{c_o(\mathbf{x})} - \int_{\Gamma_{oi}} \frac{\delta c(\mathbf{x}, t) + \mathbf{u}(\mathbf{x}, t) \cdot \boldsymbol{\tau}}{c_o^2(\mathbf{x})} ds \\ &= T_{\Gamma_{oi}} + \delta T_i. \end{aligned} \quad (3.2)$$

Γ_{oi} represents a ray which has traveled in the reference sound speed field, and $T_{\Gamma_{oi}}$ is its associated travel time. The perturbation travel time is

$$\delta T_i = - \int_{\Gamma_{oi}} \frac{\delta c(\mathbf{x}, t) + \mathbf{u}(\mathbf{x}, t) \cdot \boldsymbol{\tau}}{c_o^2(\mathbf{x})} ds \quad (3.3)$$

and for the reciprocal transmission

$$\delta T_i^r = - \int_{\Gamma_{oi}} \frac{\delta c(\mathbf{x}, t) - \mathbf{u}(\mathbf{x}, t) \cdot \boldsymbol{\tau}}{c_o^2(\mathbf{x})} ds . \quad (3.4)$$

The negative sign associated with the current in the numerator of the integrand of (3.4) arises in the reciprocal transmission since the unit tangent vector is now directed in the opposite ($-s$) direction.

Forming sums and differences of the reciprocal transmissions, and keeping only the leading order term, we find that

$$\delta T_i^+ = \frac{\delta T_i + \delta T_i^r}{2} = - \int_{\Gamma_{oi}} \frac{\delta c(\mathbf{x}, t)}{c_o^2(\mathbf{x})} ds , \quad (3.5)$$

$$\delta T_i^- = \frac{\delta T_i - \delta T_i^r}{2} = - \int_{\Gamma_{oi}} \frac{\mathbf{u}(\mathbf{x}, t) \cdot \boldsymbol{\tau}}{c_o^2(\mathbf{x})} ds . \quad (3.6)$$

The problem has now separated. The sum of the reciprocal travel time perturbations is linearly related to the sound speed perturbation δc , while the difference is linearly related to the current $\mathbf{u} \cdot \boldsymbol{\tau}$ along the ray path. Sound speed is directly proportional to temperature (θ), with an approximate empirical relationship given by (Munk and Wunsch, 1979)

$$\frac{\delta c}{c_o} = \alpha \delta \theta , \quad (3.7)$$

where $\alpha = 3.2 \times 10^{-3} (\text{°C})^{-1}$. Sound speed is also a function of the salt content of the water, but the salinity effect on sound speed is an order of magnitude less than that for temperature. Thus, (3.5) can be considered a linear relationship between

the sum of reciprocal travel time perturbations and perturbations in temperature. Equations (3.5) and (3.6) constitute the acoustic forward problem for temperature and current velocity, respectively.

With a triangular array of transceivers, relative vorticity may also be determined. Using Stokes' theorem, the circulation around a closed region is equivalent to the areal-averaged relative vorticity. Equation (3.6) shows that the line integral of fluid velocity between two points is directly proportional to the difference in travel time of two signals transmitted in the opposite direction. The line integral of the velocity around a triangle is then

$$\oint \bar{\mathbf{u}} \cdot d\tau = \sum_{i=1}^3 \bar{\mathbf{u}}_{i,i+1} S_{i,i+1} = - \sum_{i=1}^3 c_{oi,i+1}^2 \delta T_{i,i+1}^- , \quad (3.8)$$

where S_i is the ray path length, and the summation is cyclic. Using Stokes' theorem

$$\oint \bar{\mathbf{u}} \cdot d\tau = \iint \mathbf{n} \cdot (\nabla \times \bar{\mathbf{u}}) dx dy = A \bar{\zeta} , \quad (3.9)$$

where \mathbf{n} is a unit normal in the vertical direction, A is the planar surface area, and $\bar{\zeta}$ is the average relative vorticity. The areal-averaged relative vorticity can thus be written as

$$\bar{\zeta} = -\frac{1}{A} \sum_{i=1}^3 c_{oi,i+1}^2 \delta T_{i,i+1}^- . \quad (3.10)$$

3.3 The Inverse Problem

The inverse problem is to solve (3.5) and (3.6) for sound speed perturbations and current velocities, given acoustic travel time measurements. From the data, in this case travel time measurements of acoustic pulses, we must estimate the sound speed perturbations and current velocities. When discretized, (3.5) and (3.6) represent a linear system of equations. A full arsenal of linear inverse methods is available to attack the problem.

There are many estimation techniques available to solve the problem, and a vast literature (*e.g.*, Lawson and Hanson, 1974; Liebelt, 1967). Here, the inverse solution to an arbitrary system of linear equations will be presented. This solution will then be tailored to our specific problem when the ocean model chosen for this exercise is introduced in Section 5.1. Proceeding, (3.5) and/or (3.6) can be cast as a linear system of equations

$$\mathbf{G}\mathbf{m} = \mathbf{d} , \quad (3.11)$$

where \mathbf{d} is a vector of observations, \mathbf{m} is a vector of unknown parameters, and \mathbf{G} is an operator matrix (the kernel) which represents the background model.

The inverse of (3.11) can then be written symbolically as

$$\hat{\mathbf{m}} = \mathbf{G}^T \mathbf{d} , \quad (3.12)$$

where \mathbf{G}^T is a left inverse of \mathbf{G} . Noise is invariably present in the system, and is included additively as

$$\mathbf{G}\mathbf{m} + \mathbf{n} = \mathbf{d} , \quad (3.13)$$

where \mathbf{n} is a vector of observational noise. The goal is to obtain a best estimate $\hat{\mathbf{m}}$ of the true model parameter vector \mathbf{m} . The singular value decomposition is used to solve the problem. The singular value (or spectral) decomposition is a factorization of the operator matrix into a set of orthonormal eigenvectors and associated eigenvalues. The value of this re-parameterization is the ease with which it lends itself to the quantitative ranking of information content of the system. Thorough discussions of the SVD can be found in Lanczos (1961), Wiggins (1972), Jackson (1972), Wiggins *et al.*, (1976), and Wunsch (1978), and will not be reproduced here. This procedure yields an estimate which minimizes the squared Euclidean norm of both the data residuals and the estimated model parameters.

The minimum variance-biased estimate of \mathbf{m} , given in (3.13), is (see *e.g.*, Liebelt, 1967)

$$\hat{\mathbf{m}} = \mathbf{G}[\mathbf{G}\mathbf{G}^T + \sigma^2\mathbf{I}]^{-1} \mathbf{d}, \quad (3.14)$$

where σ^2 is the ratio of the noise variance to the solution variance and \mathbf{I} is the identity matrix. The selection of the noise and solution matrices is made *a priori*, and is discussed in more detail in Section 4.1. This particular estimator minimizes the objective function $(\mathbf{G}\mathbf{m} - \mathbf{d})^T(\mathbf{G}\mathbf{m} - \mathbf{d}) + \mathbf{m}^T\mathbf{m}$. In other words the SVD minimizes the size of both the data residuals and the solution in a least squares sense. Formal statistical errors can also be calculated for the solution. It is important to

point out that the solution is dependent on the choice of the ocean model and assumed *a priori* noise variances, and its sensitivity to the specific choices must be considered.

3.4 Acoustic Considerations

Before presenting the processed data, we consider the local acoustic environment. The region of interest is typical of a mid-latitude region in terms of its acoustic properties — acoustic propagation in this type of channel has been well documented. The sound channel acts as a waveguide to confine acoustic energy within the sound channel axis due to refraction via Snell's law. A climatological sound speed profile, derived from Levitus (1982) climatological data, is shown in Figure 3.1. Profiles from CTD stations occupied in the area during deployment and recovery of the tomographic instrumentation have also been constructed. Del Grosso's empirical algorithm for the conversion of temperature, pressure and salinity to sound speed has been utilized in the sound speed profile calculations (see Del Grosso, 1974). The minimum in the sound speed profile, the sound channel axis, is located at a depth of approximately 1200 m. The climatological sound speed profile is very similar to the CTD-generated profiles, the only discernible difference being in the upper 300 m of the water column. This difference can be simply attributed to the presence or absence of a seasonal mixed layer.

As mentioned previously, the forward problem of modeling acoustic propagation will be addressed using ray tracing. Most ray tracing programs use constant sound speed gradient segments to approximate a continuous sound speed profile. Different sound speed profiles can be specified at various ranges for the range-

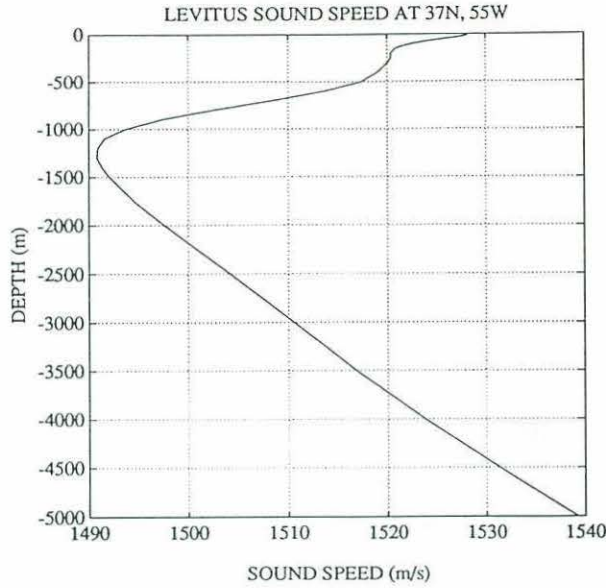


Figure 3.1: Levitus climatological sound speed profile at 37°N, 55°W.

dependent case. Interpolation between successive locally range-independent sound speed profiles gives the sound speed as a function of range. The ray paths are then calculated by integration of the ray path equations, as specified by Snell's law (see *e.g.*, Officer, 1958). The ray is assumed to travel in a vertical plane connecting the source and receiver. Out-of-plane effects which produce horizontal sound speed gradients are generally shown to be small (see *e.g.*, Newhall *et al.*, 1990). The sound speed profiles are such that only a few ray paths actually connect a given source and receiver. These paths are called eigenrays. Ray tracing programs typically send out a fan of rays, with slightly offset launch angles, and march along in range in accordance with Snell's law to the range of the receiver. The eigenrays are the paths which 'hit' the receiver.

In the present analysis, we use the range-dependent eigenray program MPP (Multiple Profile Program) developed by C. W. Spofford (1969). The climatological sound speed field is linearly interpolated in both depth and range in specified triangular sectors. Output of the program includes eigenray arrival times and

transmission loss, calculated from geometrical spreading and losses due to boundary reflections, along with a history of the eigenray trajectories. Travel times and ray paths generated with MPP have been shown to be in excellent agreement with analytical calculations (Spiesberger and Worcester, 1983; Spiesberger, 1985).

We now proceed to the ray tracing for the October SYNOP tomography experiment. Figure 3.2 shows range-independent ray traces for separation ranges of 103 km and 203 km (the distance between moorings 2 and 4, and 2 and 5, respectively). These two ray trace examples are illustrative of the range-independent ray traces computed for the entire array. Only purely refracted eigenrays are shown. Surface and bottom reflected arrivals are also obtained with the ray trace, but are not shown here. Note that no acoustic paths sample the near surface region or depths much greater than 4000 m. A typical loop distance (distance to complete both an upper loop and a lower loop) is of the order of 50 km for the two cases. More eigenrays exist for the legs with greater distances separating the transceivers. Also note that the ray tracing plots are vertically exaggerated. The steepest eigenrays have initial source angles with respect to the horizontal of less than 15° .

The ray tracing picture is not complete without a discussion of the arrival sequence of eigenrays. Each acoustic eigenray has an associated arrival time, and travel time patterns for the eigenrays (multipaths) of Figure 3.2 are depicted in Figure 3.3. Also included in these plots, interspersed with the refracted arrivals, are surface reflected rays with less than five surface interactions. The earliest arrivals correspond to the steepest refracted rays. Later arrivals correspond to small angle, axial (paraxial) refracted rays. A strong cluster of paraxial rays arrives nearly simultaneously (at 69.05 s and 136.15 s) for the two sequences.

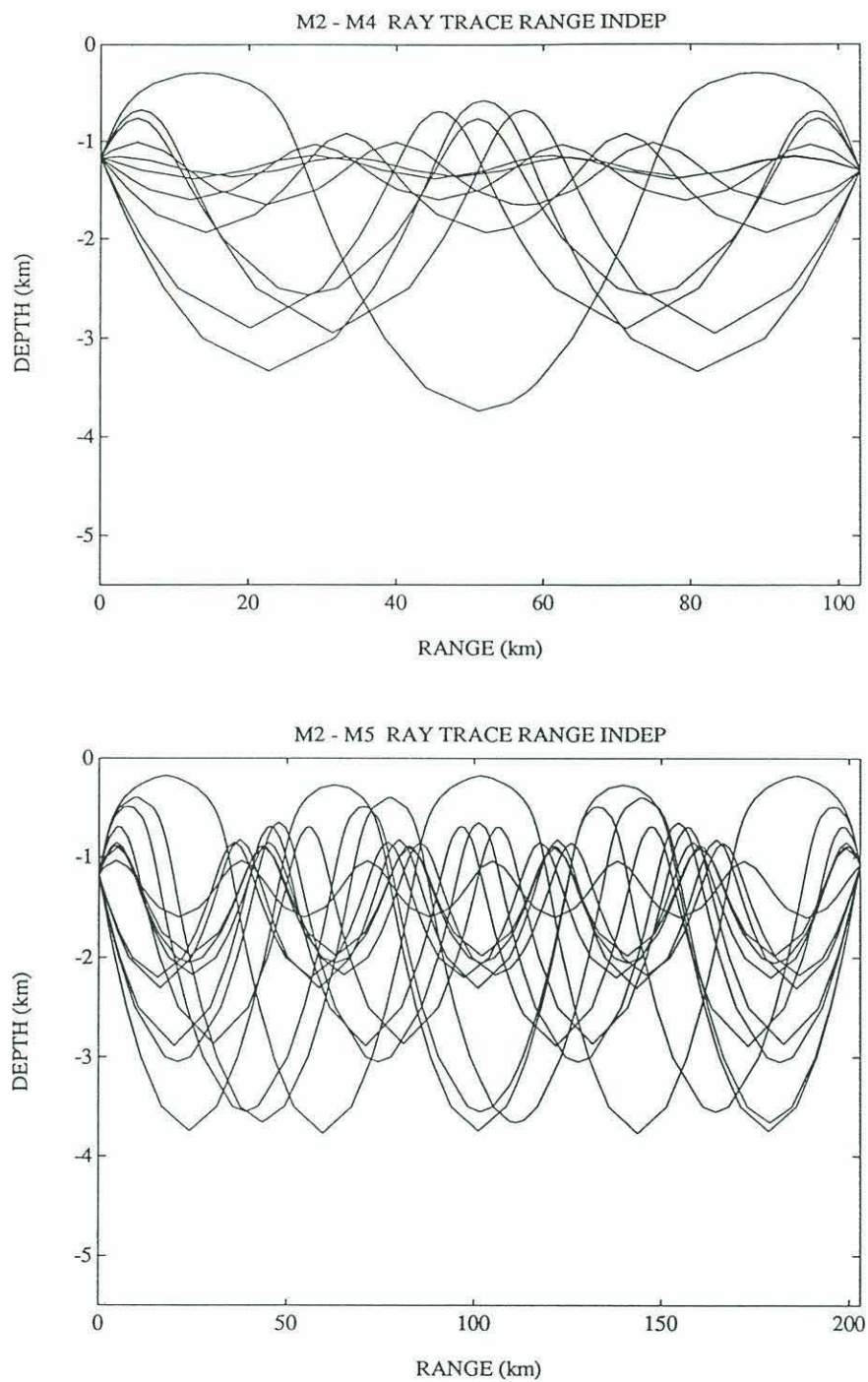


Figure 3.2: Range-independent ray traces for (top) moorings 2 to 4 and (bottom) moorings 2 to 5. The ranges of separation are 103 km and 203 km, respectively.

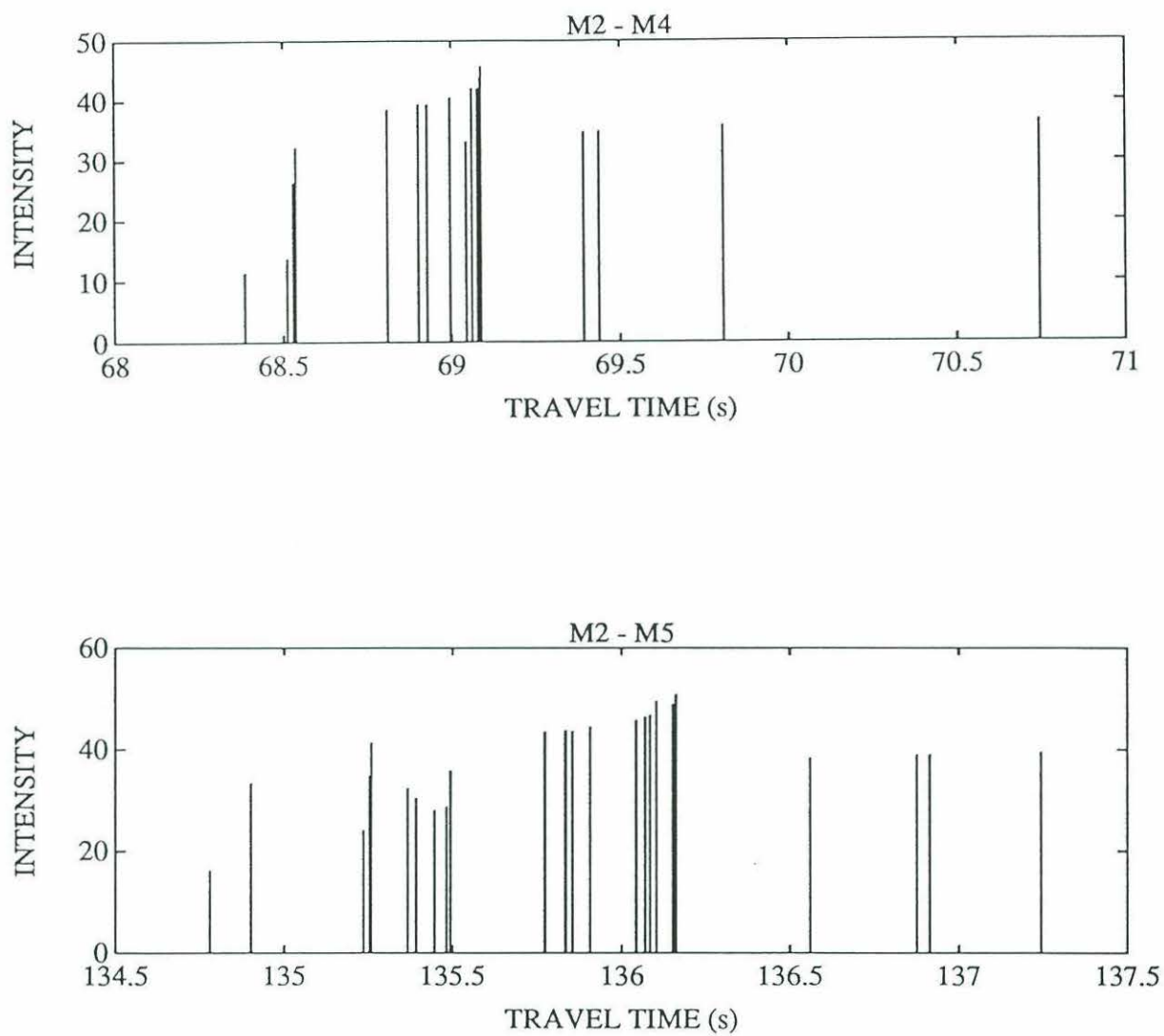


Figure 3.3: Arrival time sequences for the eigenrays depicted in Figure 3.2. Surface reflected ray arrivals with less than five surface interactions are also included in the travel time patterns.

The eigenray travel time is a function of both path length and sound speed. From the eigenray arrival sequences, it is seen that rays traveling in the higher sound velocity regions (near the surface and at great depths) arrive earlier than the axial rays despite a longer path length. This trend can also be observed in a plot of eigenray travel time as a function of initial angle (see Figure 3.4). The eigenrays with larger initial angle arrive earliest, up to the point where the ray path length increase more than compensates for the increased average speed of sound for rays with a large number of reflections at 68.5 and 135.30 s. The near-axial arrivals, with initial angles ranging from -10° to 10° , all arrive at nearly the same time (69.0 s and 136.1 s).

Range-dependent ray traces were also computed for the region. Sound speed profiles were constructed from Levitus (1982) climatological data and CTD profiles obtained during the deployment and recovery of the tomographic transceivers. The sound speed profiles were linearly interpolated in range and used as input to range-dependent ray traces. The results differed very little from the range-independent ray traces. Ray traces with slightly altered ranges and depths were also investigated, and the calculated rays again were quite similar to those obtained in the range-independent case. This leads us to treat the range-independent results as representative for this experiment.

By matching the actual acoustic multipath arrival times with the arrival times calculated using the ray tracing model, we are able to infer the paths of propagation. This is the critical connection between the forward and the inverse problem. The identification of the arrivals will be discussed in Section 4.1.

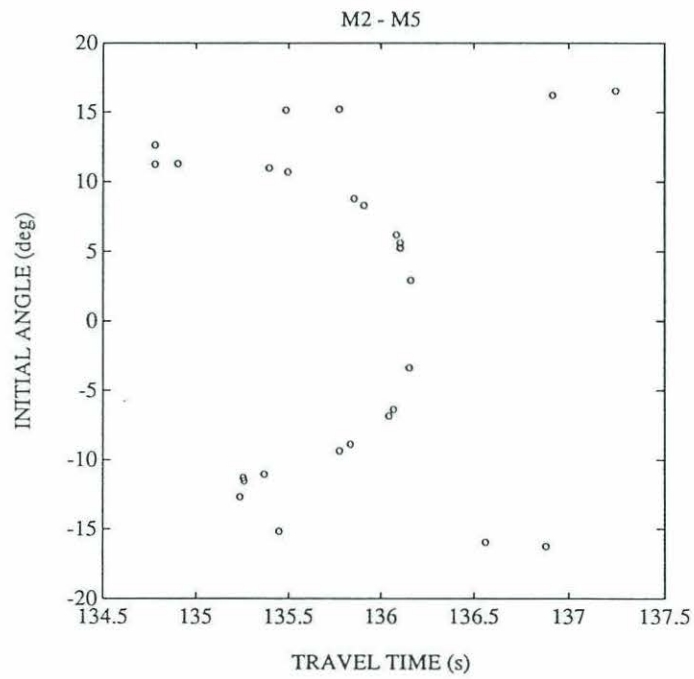
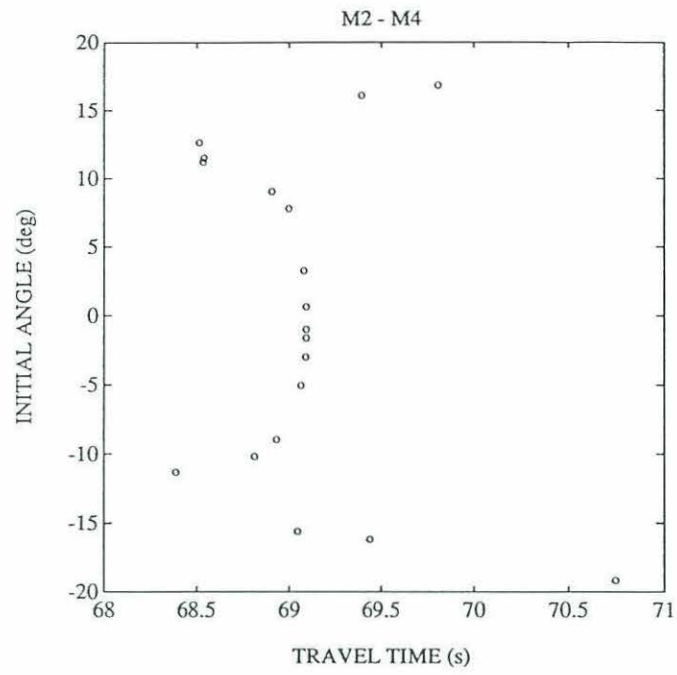


Figure 3.4: Order of ray arrivals.

3.5 The Processed Tomographic Data

The SYNOP tomography experiment generated twenty individual pulse response records (ten sets of reciprocal pulse response records) over 300 days. Acoustic data were recorded six times per day, every four hours, on an every-other-day basis. Herein, we will refer to the data records as S2R5 (signifying transmission from mooring 5 to mooring 2), S5R2 (signifying transmission from mooring 2 to mooring 5), and so forth. A typical subsample of the data, for S2R5, S5R2, S4R5 and S5R4 is provided in Figure 3.5. In these figures, the acoustic intensity is plotted as a function of absolute travel time between the given instruments. Consecutive receptions, at four hour intervals, are then offset by a constant amount to aid in viewing. The arrival pattern for both cases is distinct, with several weak early arrivals, and a late cluster of arrivals, culminating with a strong late arriving peak. The early arriving rays correspond to shallow and deep turning rays, and the latest arriving, most intense portion of the record corresponds to the near axial arrivals. Looking closely at Figure 3.5 we see that identification of individual multipaths is not a simple task. The appearance and disappearance of multipaths is attributed to the influence of tides, internal waves, and multipath interference effects. It is also evident that the pulse responses from reciprocal transmissions are not identical. It should be noted that the records are not exactly reciprocal, owing to medium changes during a 45 (15)-minute time delay between the reciprocal transmissions between S2R5 and S5R2 (S4R5 and S5R4).

The intensities of the acoustic peaks in Figure 3.5 vary from 10 to 30 dB. The earliest arriving peaks typically have intensities in the range of 10–15 dB, the latest arrivals approximately 30 dB. The measured intensities compare well with

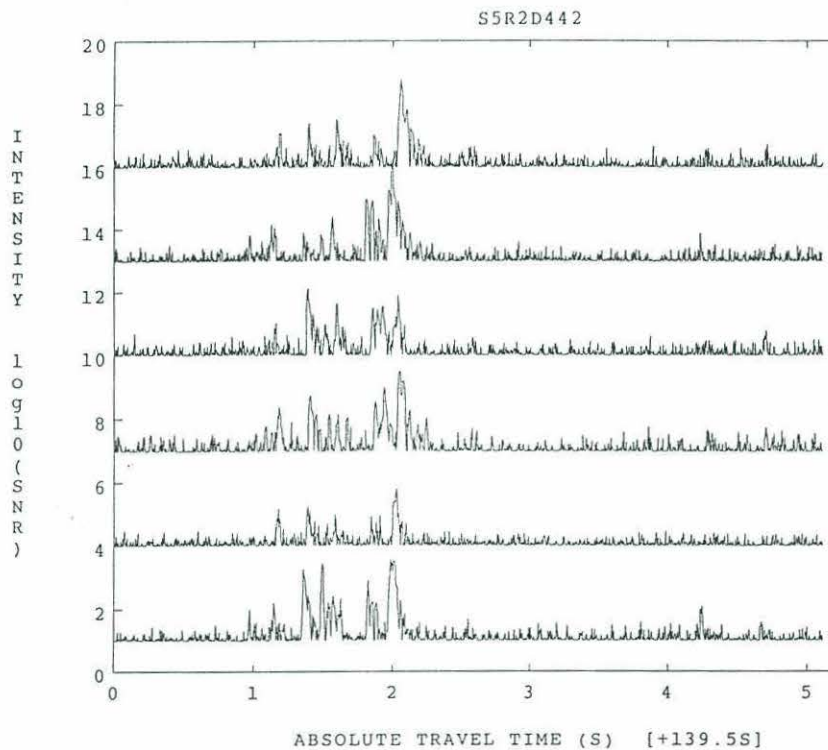
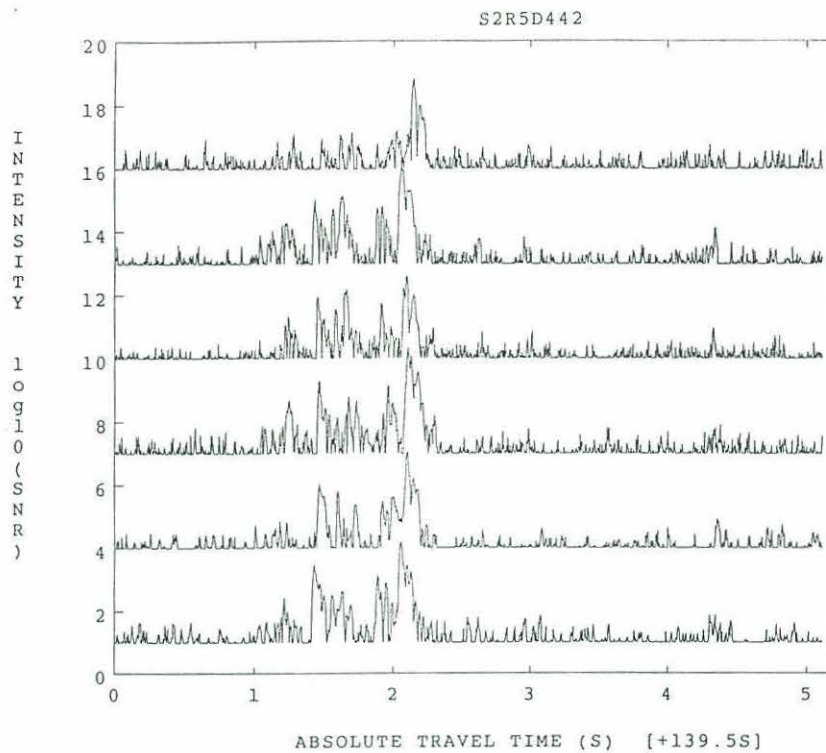


Figure 3.5: Raw pulse response records for S2R5 and S5R2. The y -axis label is the intensity for the first record. Subsequent records are offset to aid in viewing. The sampling interval is four hours.

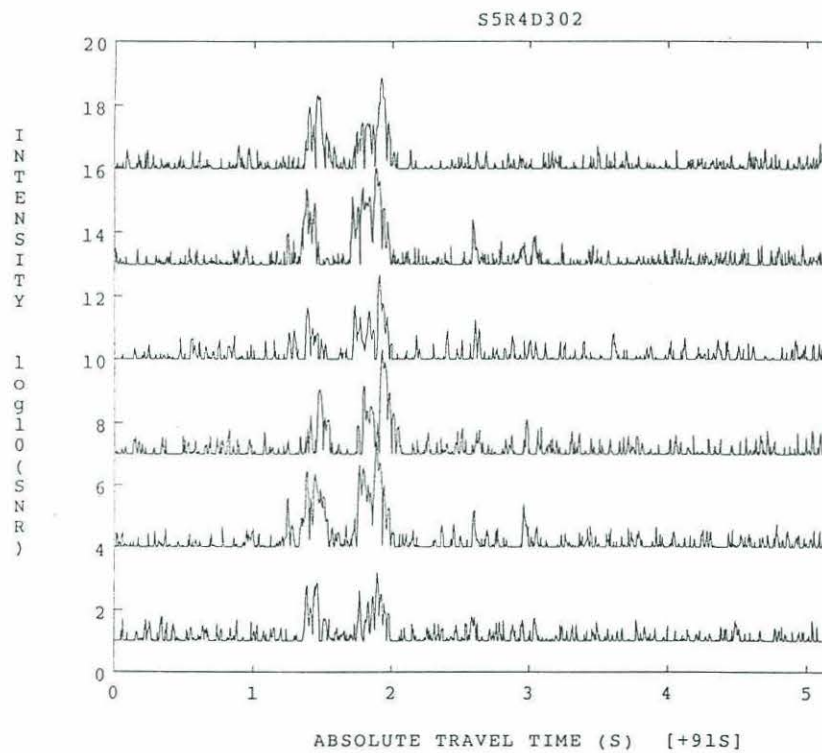
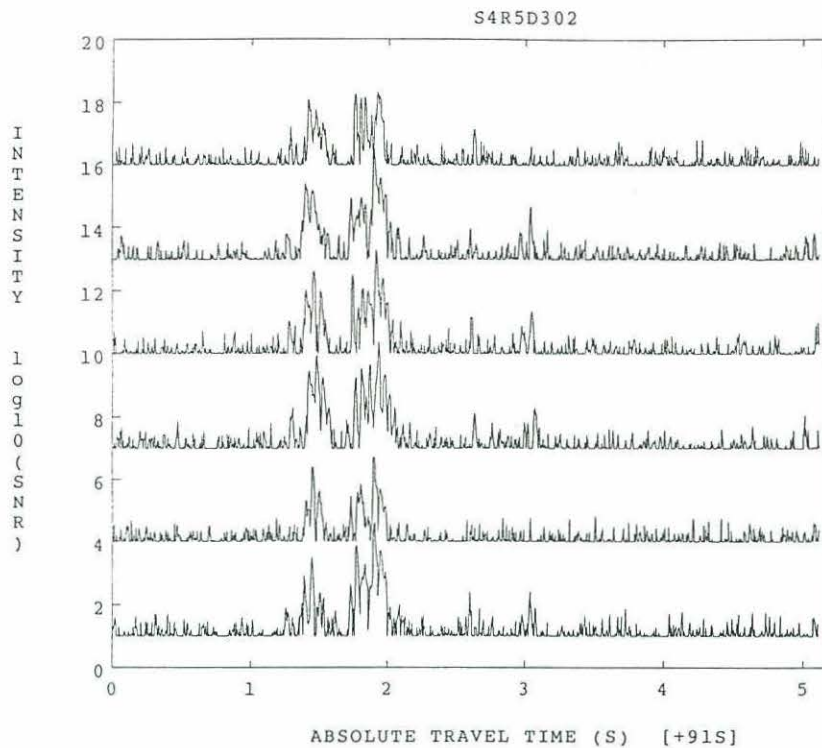


Figure 3.5: Raw pulse response records for S4R5 and S5R4. The y -axis label is the intensity for the first record. Subsequent records are offset to aid in viewing. The sampling interval is four hours.

those predicted from a sonar equation approach. The expected signal level of an average pulse response is about 25 dB (see Table 3.1).

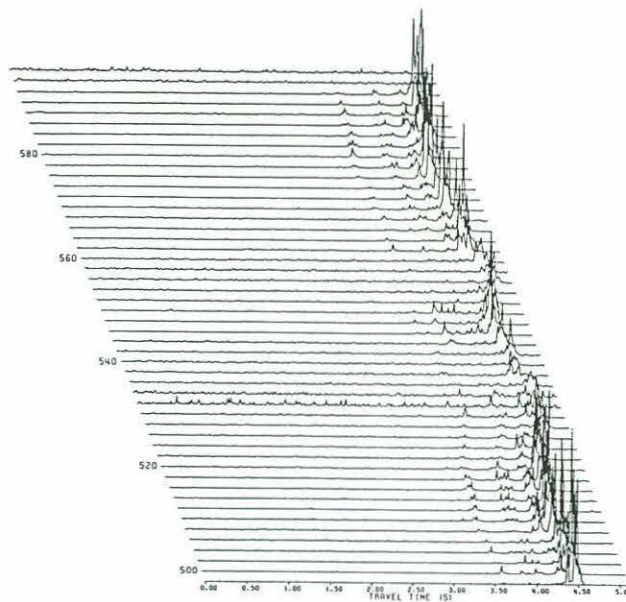
The acoustic arrivals are more stable and resolvable after daily averaging six pulse responses. By doing this we reduce the high-frequency tidal and internal wave signals and decrease the random noise level. Data records of daily averaged pulse responses are shown in Figure 3.6 for cases S2R5, S5R2, S2R4 and S4R2. Several features are prominent in all of the plots. The most obvious signal is a large peak which is seen as the latest arrival in all records. This peak always exists, although the shape (multipath structure) varies slightly between receptions. The pulse responses of daily averaged reciprocal transmissions are very similar, with only small-scale differences evident. A typical current velocity would only shift one of the records (relative to its reciprocal partner) a few milliseconds, which would not be discernible to the eye in the scale of these figures.

Cross-correlations of reciprocal receptions and successive receptions separated by four hours were performed on the individual data records. Cross-correlations of reciprocal records test the reciprocity of the acoustic paths. The maximum cross-correlation value of reciprocal records occurs at some lag, which is indicative of the current acting between the two instruments. This is a somewhat biased estimate of the barotropic current as the most intense peaks, leading to greater weighting, correspond to near-axial refracted rays. Cross-correlations of successive arrivals test the stability of the acoustic paths at four hour intervals. The maximum cross-correlation value occurs at some lag relative to the earliest record. This lag is primarily caused by internal waves, tides, mooring motion, and temperature effects on the travel time signal. Record mean correlation coefficients for the various data records are given in Table 3.2. From Table 3.2 we see that the correlations computed

Table 3.1: Signal-to-Noise Ratio

Loss/Gain Mechanism		Loss/Gain (dB)
Source level (re 1 μ Pa at 1 m)		180
Transmission loss		
Spherical spreading $-20 \log_{10} R$	(100 km)	-100
	(200 km)	-106
Attenuation loss .0168 dB/km	(100 km)	-2
	(200 km)	-3
Received signal level	(100 km)	78
	(200 km)	71
Noise (1 Hz band)		-70
Bandwidth (100 Hz)		-20
Received signal-to-noise ratio	(100 km)	-12
	(200 km)	-19
Processing gain		
Coherent averaging gain $(10 \log_{10} (\text{number of pulses} - 2))$		16
Pulse compression gain $(10 \log_{10} \frac{\text{sequence duration}}{\text{digit duration}})$		27
Total signal processing gain		43
Signal-to-noise ratio of pulse	(100 km)	31
	(200 km)	24

S2R5 DAY 498-596



S5R2 DAY 498-592

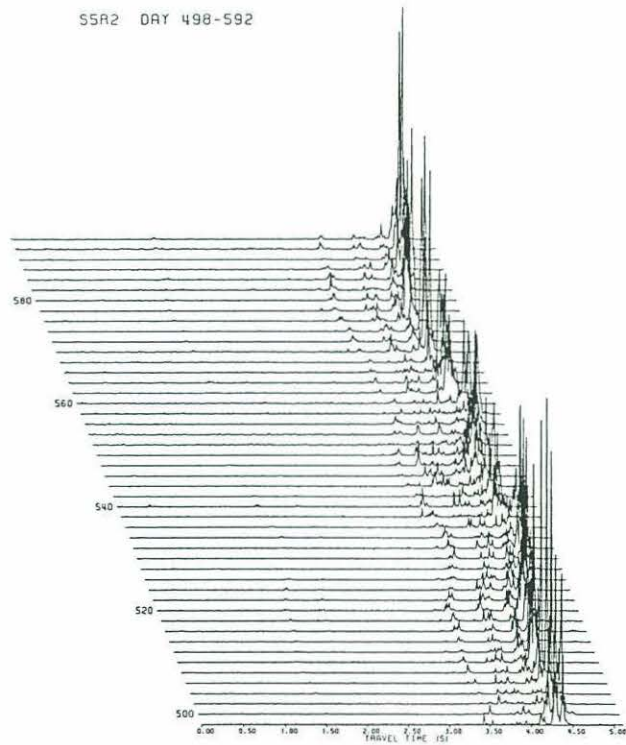
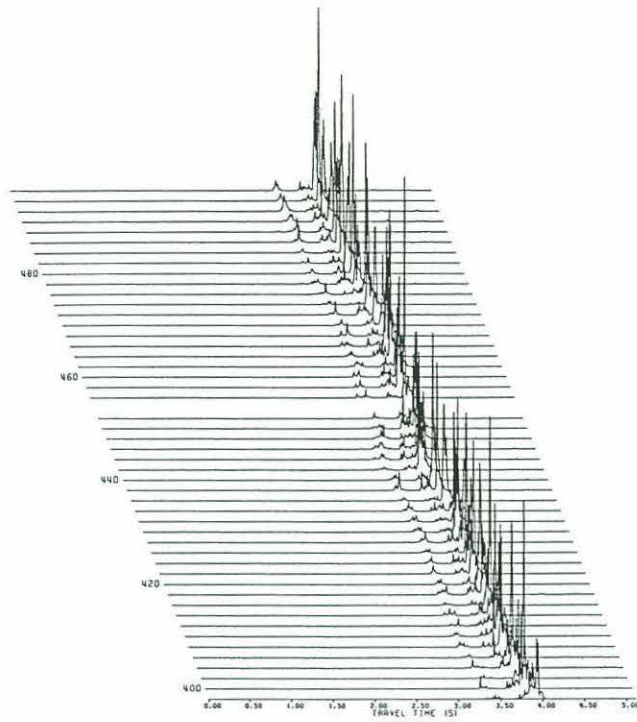


Figure 3.6: Daily-averaged pulse response records for S2R5 and S5R2. The height variable is intensity in arbitrary units. Subsequent records are offset to aid in viewing. The sampling interval is two days.

S4R5 DAY 398-496



S5R4 DAY 398-496

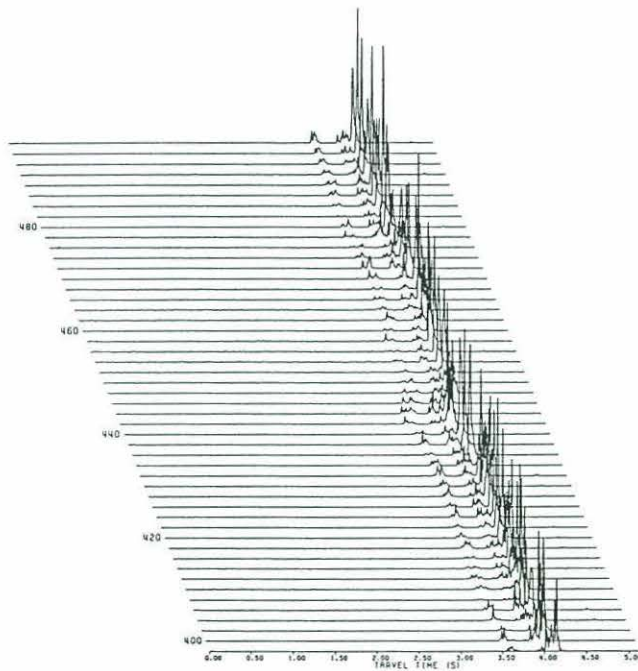


Figure 3.6: Daily-averaged pulse response records for S4R5 and S5R4. The height variable is intensity in arbitrary units. Subsequent records are offset to aid in viewing. The sampling interval is two days.

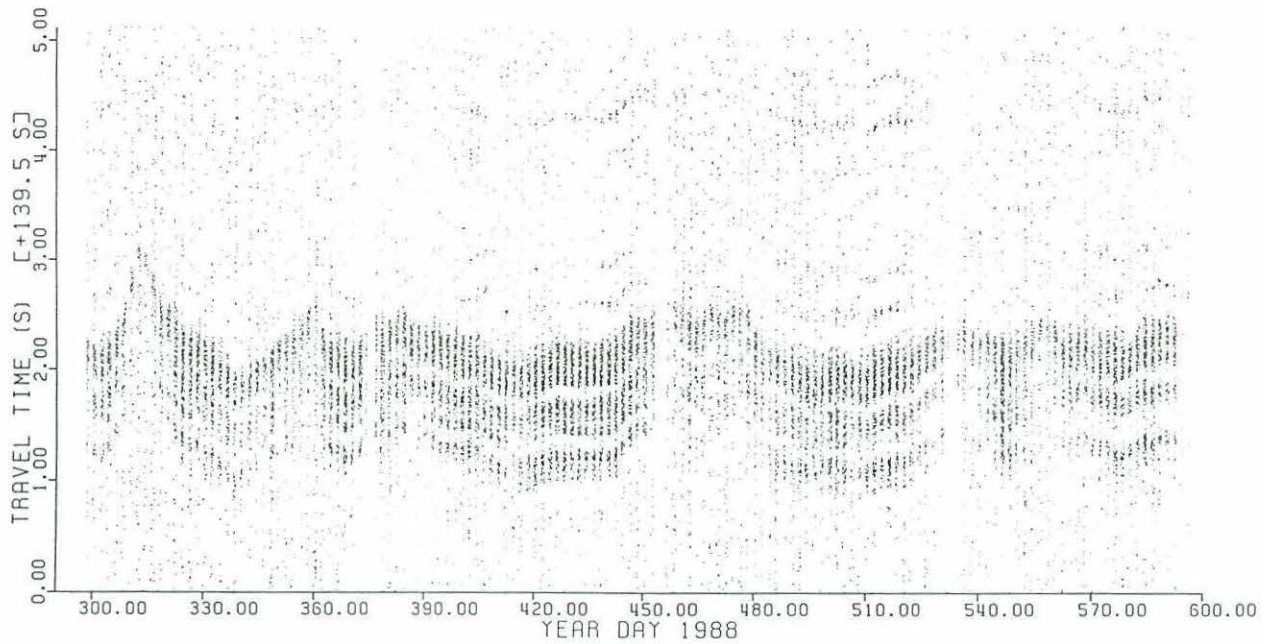
Table 3.2: Cross-Correlation Statistics

Record	Correlation Coefficients	
	Successive Receptions	Reciprocal Receptions
M1R2 M2R1	.31 .71	.35
M1R3 M3R1	.33 .53	.33
M1R4 M4R1	.25 .66	.27
M1R5 M5R1	.28 .70	.31
M2R3 M3R2	.72 .49	.58
M2R4 M4R2	.69 .76	.70
M2R5 M5R2	.68 .73	.69
M3R4 M4R3	.31 .70	.43
M3R5 M5R3	.55 .77	.63
M4R5 M5R4	.76 .75	.74

for reciprocal transmissions (15–60 minutes apart in time) are less than correlations computed pulse to pulse for one-way transmissions with a four-hour time interval. The smaller correlations of the reciprocal transmissions are most likely due to non-reciprocity resulting from current gradients. The low cross-correlation coefficient values obtained from the receptions at mooring 1 are due to the receiver at mooring 1 malfunctioning intermittently, so more appropriate values are estimated using only the portion of the record when data is available. The low cross-correlation values for the receptions at mooring 3 are due to a noisy hydrophone.

From the individual acoustic data, we need to construct time series of travel time arrivals for all of the stable and identifiable peaks. The procedure used is a crude pattern recognition approach. The first step is to identify all of the peaks in the record, and discard all values with a signal-to-noise ratio less than a threshold of 7 dB. Peaks with a signal-to-noise ratio less than 7 dB are too difficult to extract from the background noise. Peaks for S2R5, S5R2, S4R5 and S5R4 are displayed in Figure 3.7. This step typically reduces the data from 1022 demodulates per reception to about 50 demodulates per reception. Following this procedure arrivals were aligned to aid in the peak-picking process. Several approaches were attempted, including alignment by the intense late arriving peak, and alignment by the correlation of successive receptions. Both procedures yielded similar results when the shifted data were compared. A template made up of windows in travel time space is specified after carefully choosing the best resolved days of travel time data. The template is marched forward in time, and all of the peak arrivals falling in the specified windows are kept. The template window widths are set to account for routine fluctuations (deriving from oceanic variability and mooring motion) in the arrival

M2R5 DAY 298-596 INDIV RECPT SNR > 5



M5R2 DAY 298-592 INDIV RECPT SNR > 5

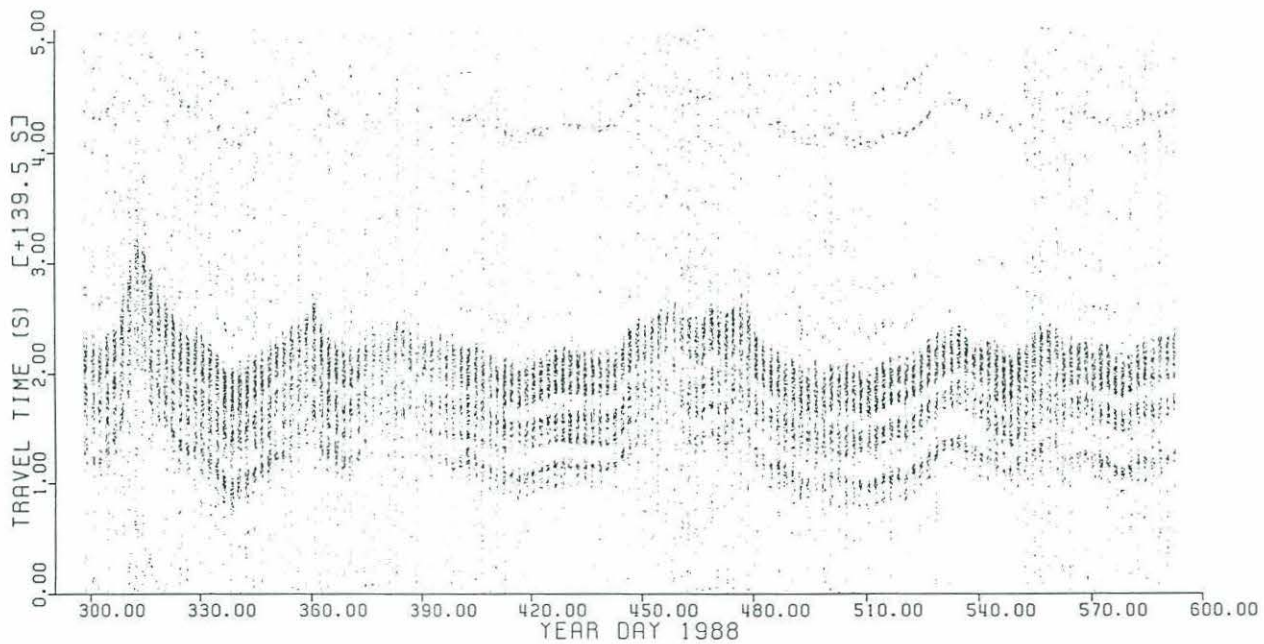
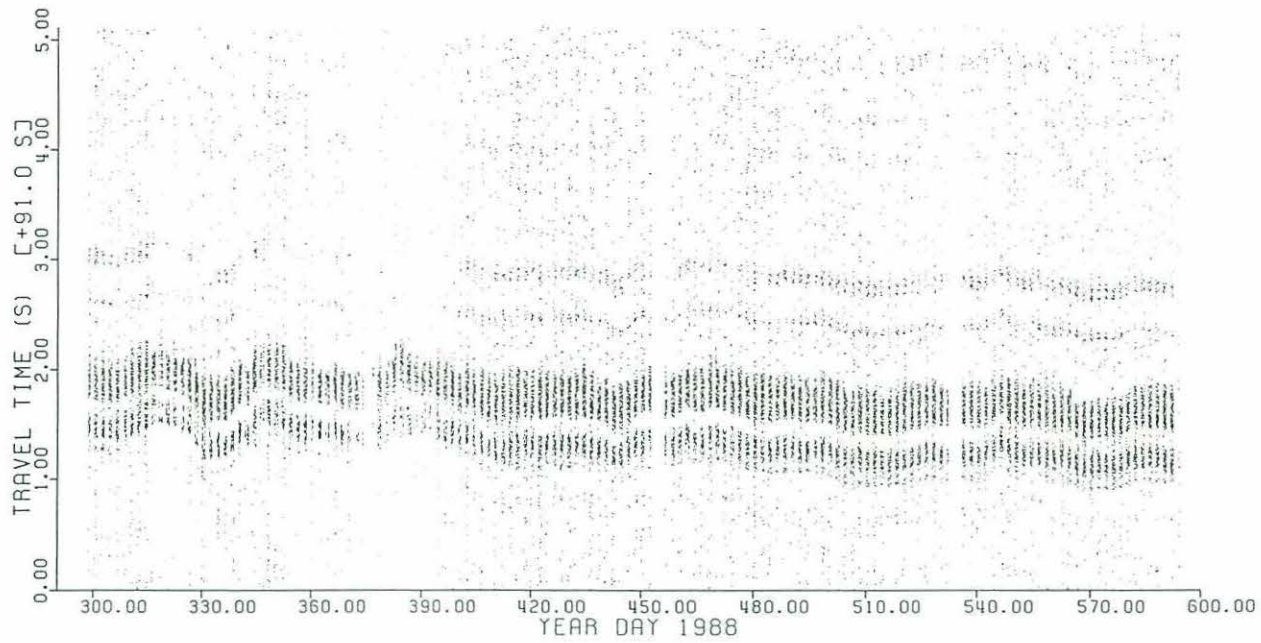


Figure 3.7: Peaks for S2R5 and S5R2. Each 'dot' is a line whose length is proportional to the signal-to-noise ratio. Only peaks with a signal-to-noise ratio greater than 7 dB are included.

M4R5 DAY 298-594 INDIV RECPT SNR > 5



M5R4 DAY 298-592 INDIV RECPT SNR > 5

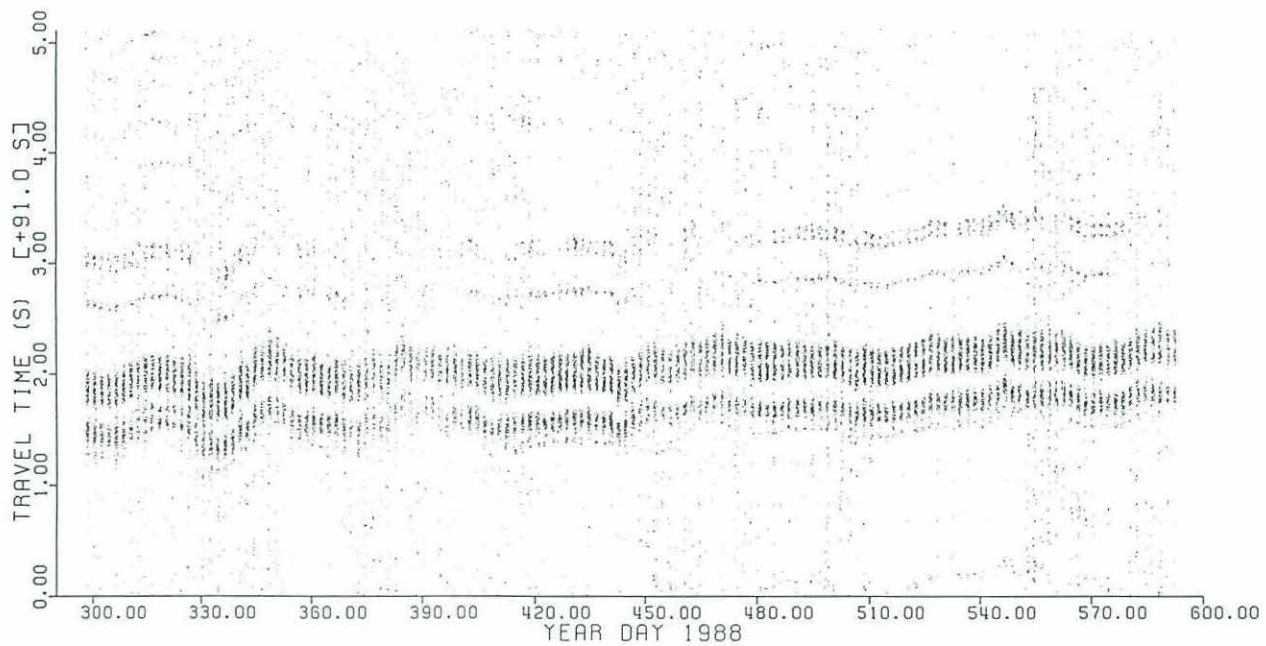


Figure 3.7: Peaks for S4R5 and S5R4. Each 'dot' is a line whose length is proportional to the signal-to-noise ratio. Only peaks with a signal-to-noise ratio greater than 7 dB are included.

time from one reception to the next. The prescribed window widths were set at 50 ms.

For the stable peaks (typically two to five), estimates of the arrival time are obtained by taking the center of mass of the peak values and the three demodulates immediately preceding and following the peak. For a full record, typical tracked paths range from 30–100% complete. The intense late arriving peak is robust, and present in all of the records more than 95% of the time. Earlier arriving peaks suffered sporadic dropout, depending on the pair considered.

Sum and difference data were calculated from the tracked peaks, and outliers were discarded from both series. The outliers were most evident in the difference series. It was often the case that no reciprocal peak was tracked for a source/receiver pair, so sums and differences could not be calculated. Final time series were typically only 50% complete for most of the tracked peaks for both sums and differences. However, sum and difference series constructed from the intense late arriving peak were still at least 95% complete in all cases. From the sum and difference series, high-frequency variances of the data, due to internal waves, tides and instrumental noise, can be obtained and are discussed in detail in the following section. The focus herein is to investigate lower frequency phenomena, with periods greater than several days, so the individual data are low-pass filtered. The tracked data are convolved with a cosine-bell function with a total width of four days, corresponding to a 3 dB cutoff at a period of two days. The low-pass filtered data set of the peaks are 50–80% complete, and the late arriving peak is nearly 100% complete for all records. Each source/receiver pair typically has two to six stable and identifiable tracked peaks.

3.6 Errors

3.6.1 Introduction

The errors encountered in the tomographic measurement are the focus of this section. The reader who is not interested in technical details can read the introduction and discussion sections to obtain an adequate background.

Errors in the tomographic measurement can be divided into two classes — measurement errors and resolution errors. The measurement errors are the sources of noise which limit the accuracy of the estimate of acoustic travel times. The dominant error sources consist of mooring motion, internal wave effects, clock drift, and peak estimation errors arising from finite signal-to-noise ratio. A description of all of the errors contained in the estimation of the acoustic travel time signal is provided in Section 3.6.2. One of the larger sources of error in the tomographic measurement is due to unknown instrument position, and an entire section is devoted to a discussion of the correction for mooring motion-induced errors. Resolution errors arise from inadequate sampling of the medium due to a limited number of acoustic multipaths connecting each source/receiver pair. A typical tomographic experiment will have anywhere from one to ten stable and identifiable acoustic multipaths to sample the vertical structure of the water column. The resolution errors can formally, and readily, be estimated from the inverse solution. Herein, they are considered in the context of the singular value decomposition. Overall error estimates for the estimated fields of temperature, current velocity and areal-averaged relative vorticity are provided in the final section of this chapter.

Before focusing on the errors themselves, we consider the size of the expected oceanographic signal. The signals of interest are the fluctuations in the sound speed (temperature) field and the current velocity. A typical mesoscale event may have temperature deviations from the mean state of a few °C and associated velocities of 20–50 cm/s. A temperature deviation of 1°C yields a change in acoustic travel time of about 200 ms (400 ms) over a range of 100 km (200 km). Current-induced fluctuations in travel time are much smaller. A 20 cm/s current acting over a range of 100 km (200 km) will alter the travel time by only 5 ms (10 ms).

The largest error source is due to unknown instrument positioning and time-varying mooring motion. Uncertainty in the absolute range between transceivers due to GPS or Loran accuracy in the positioning of the source and receiver leads to a bias in the estimate of the sound speed (temperature) field. Subsurface moorings were used to moor the tomographic transceivers during the Gulf Stream tomography experiment. Water depths were nominally 5300 m, and the moorings extended upward to about the 1000 m level. A vertical excursion of the transceiver of only 10 m leads to a horizontal excursion of roughly 300 m. This change in the range between the two transceivers leads to a travel time deviation of 200 ms. This positioning indeterminacy can easily dominate the expected oceanographic signal if not accounted for properly. Fortunately the mooring motion-induced travel time deviation drops out almost completely from the reciprocal measurements, so the small signal due to current velocity is not overwhelmed by mooring motion. Other error sources, such as internal waves and clock drift, have a lesser effect on the expected oceanographic signal. A complete accounting of the various error sources is given in the following sections. The conclusion is that for daily-averaged travel time estimates, the measurement errors in the travel time estimate can be reduced

to order 1 ms, and the errors in the field estimates are comparable with those obtained using conventional instrumentation. The precision with which we can measure temperature, current velocity and vorticity is presented in the discussion section.

3.6.2 Travel Time Variance

The basic datum in tomography has been the travel time of acoustic multipaths. Acoustic intensities have also been used, but have been shown to add very little additional independent data (Brown, 1984). The accuracy of the estimated oceanographic fields depends directly on the precision with which the travel time measurement is made. In this section we investigate the various sources of noise which contaminate the estimate of the arrival time of the acoustic multipaths.

For the simplest case of a constant range R_0 and a constant (in space and time) sound speed field c_0 , the travel time between a source and receiver is given by $t_{c_0} = R_0/c_0$. Now consider the more realistic case where the sound speed field varies with time, the moorings are not stationary, and currents are present. The linearized one-way travel times in opposite directions may be written

$$\begin{aligned} t^+ &= t_{c_0} + \Delta t_{\Delta c} + \Delta t_u + \Delta t_{bias} + \Delta t_{\Delta R} + \Delta t_{\delta R}^+ + \Delta t_{iw}^+ + \Delta t_{clock} \pm \varepsilon , \\ t^- &= t_{c_0} + \Delta t_{\Delta c} - \Delta t_u + \Delta t_{bias} + \Delta t_{\Delta R} - \Delta t_{\delta R}^- + \Delta t_{iw}^- - \Delta t_{clock} \pm \varepsilon , \end{aligned} \quad (3.15)$$

where

t^+ and t^- are the measured reciprocal travel times,

t_{c_0} is the travel time in the reference state c_0 at a range of R_0 $O(10^5 \text{ ms})$,

$\Delta t_{\Delta c}$ is the travel time deviation due to changes in the reference sound speed field $O(100 \text{ ms})$,

Δt_u is the travel time deviation due to currents $O(10 \text{ ms})$,

Δt_{bias} is the travel time bias due to unknown reference range $O(100 \text{ ms})$,

$\Delta t_{\Delta R}$ is the travel time deviation due to transceiver movement from the reference range $O(50 \text{ ms})$,

$\Delta t_{\delta R}$ is the travel time deviation due to receiver movement during the transmission $O(1 \text{ ms})$,

Δt_{iw} is the travel time deviation due to internal wave effects $O(1 \text{ ms})$,

Δt_{clock} is the travel time deviation due to clock drift $O(1 \text{ ms})$, and

ε is the travel time deviation due to sources not accounted for, such as background noise, insufficiently resolved multipaths which arise due to multipath interference, and signal interpolation $O(1 \text{ ms})$.

We next form sums and differences of the reciprocal measurements. The sum of the reciprocal travel time measurements in (3.15) gives

$$\frac{t^+ + t^-}{2} = t_{c_0} + \Delta t_{\Delta c} + \Delta t_{bias} + \Delta t_{\Delta R} + \frac{\Delta t_{\delta R}^+ - \Delta t_{\delta R}^-}{2} + \frac{\Delta t_{iw}^+ + \Delta t_{iw}^-}{2} \pm \varepsilon . \quad (3.16)$$

Note that travel time deviations due to both current velocities and clock drift drop out of the summed travel time measurements for simultaneous reciprocal transmissions. The last three terms on the right-hand side of (3.16), the transceiver shift during the transmission, internal wave effects, and the miscellaneous error term, respectively, are much smaller than the remaining terms on the right-hand side of (3.16). The sum travel time measurement is then given by

$$\frac{t^+ + t^-}{2} \approx t_{c_0} + \Delta t_{\Delta c} + \Delta t_{bias} + \Delta t_{\Delta R} . \quad (3.17)$$

The travel time deviations from the reference state are dominated by perturbations in sound speed (temperature), absolute positioning indeterminacy, and mooring motion.

The difference of the reciprocal travel time measurements in (3.15) gives

$$\frac{t^+ - t^-}{2} = \Delta t_u + \frac{\Delta t_{\delta R}^+ + \Delta t_{\delta R}^-}{2} + \frac{\Delta t_{iw}^+ - \Delta t_{iw}^-}{2} + \Delta t_{\text{clock}} \pm \varepsilon . \quad (3.18)$$

Note that the travel time deviations due to a fluctuating sound speed field and the absolute range, including unknown mooring positioning, cancel in the differential travel time measurements for simultaneous reciprocal transmissions. This is fortunate as these errors, or noise, would swamp the expected differential travel time signal. The second term on the right-hand side of (3.18), deviations due to transceiver shifts during transmission, typically $O(0.1 \text{ ms})$, is much smaller than the other terms on the right-hand side of (3.18). The differential travel time measurement is then given by

$$\frac{t^+ - t^-}{2} \approx \Delta t_u + \frac{\Delta t_{iw}^+ + \Delta t_{iw}^-}{2} + \Delta t_{\text{clock}} \pm \varepsilon . \quad (3.19)$$

Before looking in greater detail at the various terms in (3.15), (3.17), and (3.19), one specific detail about the experimental setup needs to be discussed. The exact mooring positioning is only known to an accuracy of $\pm 300 \text{ m}$, with the position being obtained by GPS interpolation of the anchor position. The unknown separation between the transceivers means that we cannot solve the reference field ($c_0 = t_{c_0}/R_0$, with R_0 having large uncertainty), unless we include the absolute range as an unknown in the inversion. This is not a major drawback, however. The reference field could be determined from the mean estimated over the experimental duration (if the period is long enough to yield an adequate mean estimate).

Alternatively, climatological data, such as from Levitus (1982), could be used to supply an adequate reference state. The latter approach was used in this study. We did not choose to solve for the absolute range in the inversion procedure for two reasons. First, the mean field is fairly well mapped in this region. Second, only a few multipaths were resolved and identifiable for each source/receiver pair, and solving for another unknown, the absolute range, takes away from the limited amount of information available to construct the estimated fluctuating sound speed (temperature) field. Again, it is important to point out that the absolute range drops out of the differential travel time (current) measurement.

The time-dependent mooring positioning was not monitored in this experiment. The only available data regarding transceiver positioning were pressure gauges on the instruments themselves. Pressure records indicate the amount of vertical excursion the moorings experienced during the experimental duration. However they do not provide the horizontal excursions the moorings experience as they tilt from the vertical. Vertical excursions of over 100 m in depth were seen by three of the instruments. Excursions of this magnitude are accompanied by large horizontal excursions (order 1 km), which consequently lead to large deviations in travel time arrival estimates. The discussion of mooring motion is postponed until the next section.

It is also worthwhile to note that the reciprocal transmissions between source/receiver pairs were not truly reciprocal. Transmission delays in opposite directions between various source/receiver pairs ranged from 15–60 minutes. This temporal delay leads to non-reciprocity of ray paths owing primarily to the internal wave field. Nonreciprocity is also introduced to the problem by the presence of a non-zero current.

The error terms in (3.15), (3.17), and (3.19) are now discussed, excluding mooring motion. The terms $\Delta t_{\delta R}^+$ and $\Delta t_{\delta R}^-$ arise from transceiver movement during the time it takes the acoustic signal to travel the distance between each source/receiver pair. These two terms represent the velocity of the transceiver during the transmission. The acoustic travel times between instrument pairs range from one to two minutes, and in this time the transceiver positions change less than 5 m in horizontal range. These terms are quite small in this experiment owing to the short propagation ranges and can be neglected.

The terms Δt_{iw}^+ and Δt_{iw}^- arise from internal wave effects on the travel times of the acoustic multipaths. Superimposed on the reference sound speed field at any given time is a finestructure field, which is largely made up of the internal wave field. The internal wave field acts to vertically stretch and strain the acoustic multipaths. Thorough discussions of the effect of internal waves on the travel time measurements can be found in Flatté and Stoughton (1986); Stoughton *et al.*, (1986) and Howe *et al.*, (1987). Much of the internal wave-induced variance cancels due to the destructive interference of positive and negative shifts of the internal wave field. From the 1983 reciprocal tomography experiment which was conducted near Bermuda, the internal wave-induced variance was estimated to be about 10 ms^2 (Stoughton *et al.*, 1986). The transmission range for the 1983 experiment was 300 km, which is larger than the transmission ranges for this experiment, which are 200 km and less. The internal wave-induced variance is quadratically related to the rms phase delay along the acoustic ray path, which is roughly proportional to range (see Flatté *et al.*, 1979). A smaller variance due to internal wave effects is expected in this experiment owing to the shorter transmission ranges. The internal wave-induced variance is estimated to be less than 5 ms^2 for the present

experiment. The internal wave noise is random in nature, and hence can be reduced by daily averaging over six receptions, yielding an rms error of < 1 ms.

The internal wave-induced variance tends to cancel substantially in the reciprocal transmissions when the oppositely directed transmissions occur within the internal wave correlation time (assumed to be about five minutes). For the 1983 tomography experiment conducted off of Bermuda, Stoughton *et al.*, (1986) find that the reciprocal paths are separated by a few tens of meters in the vertical. The non-coincidence of the ray paths leads to the imperfect decorrelation of the two internal wave-induced travel time variations. For time scales greater than the internal wave correlation time, there is no cancellation of the internal wave-induced travel time deviations. The reciprocal transmissions in this experiment occurred 15–60 minutes apart, so an upper bound of 5 ms^2 , (corresponding to complete signal decorrelation (the worst case scenario), is used for internal wave-related variance for differential travel time measurements also. A daily average over six receptions reduces the error level to < 1 ms. For the purpose of making low-frequency inversions, the paths are reciprocal.

Clock drift is a non-reciprocal error which is due to a clock at one of the instruments being fast relative to a clock at another instrument. Accumulated clock drifts of individual instruments over the full duration of the Gulf Stream tomography experiment are quite large, and of order 300 ms. The clock drift is nearly linear in nature, as verified by calculating a regression fit for the drift with time, so a linear detrending removes most of this error. The residual clock error is estimated at < 0.3 ms rms. The received tomographic signal is digitized in 5 ms intervals. To determine the arrival peak location, it is necessary to interpolate the received signal. In this experiment, the peak arrival time is estimated using a centroid method and

Table 3.3: Travel Time Variance

Matched filter receiver precision (σ_τ variance) $\sigma_\tau = [2\pi(\delta f)_{rms}(\frac{2E}{N})^{\frac{1}{2}}]^{-1}$	0.25 ms ²
Interpolation error variance	0.05 ms ²
Clock error	0.09 ms ²
Internal wave-induced variance	5 ms ²
Total variance	5.39 ms ²
Daily mean variance	0.96 ms ²
Daily averaged rms travel time error	~ 1 ms

keeping three demodulates immediately preceding and following each peak. The travel time error due to this interpolation procedure is estimated to be $\sim .1$ ms rms. Similar values are obtained with a Gaussian interpolation scheme. Finally, a small error arises due to the finite signal-to-noise ratio for multipath arrivals in the presence of background noise. The matched filter receiver precision is a function of the signal bandwidth and the signal-to-noise ratio (see *e.g.*, Spindel, 1985), and is estimated to be < 0.5 ms rms.

Table 3.3 gives the estimated travel time variance for the measurement of the acoustic travel times for the conditions and instrumentation used in the Gulf Stream tomography experiment. The daily averaged travel time measurement is estimated

to have an rms error of about 1 ms. This value is exclusive of mooring motion-induced errors, which are important only in the sum travel times. The estimated error variances in the Gulf Stream tomography experiment are similar to those reported in the 1983 reciprocal tomography experiment (Flatté and Stoughton, 1986).

In the previous error descriptions, little has been said about the structure of the noise. Measurement noise has a particular covariance structure, as does mooring motion, internal waves, clock drift, and so on. For example, mooring motion and clock errors are highly correlated between multipaths arriving at the same receiver. On the other hand, internal wave effects are not correlated between multipaths. Judicious usage of the covariance structure of the various noise sources can be used to reduce the overall errors in the system through the inverse framework. A good discussion of the covariance structure of the errors is given by Cornuelle (1983).

3.6.3 Mooring Motion

Mooring motion effects on the travel time can dominate the actual signal arising from variability of the sound speed field. The arrival time signal expected from the fluctuating ocean is of the order of a few hundred milliseconds. A 10 m vertical dip of the mooring leads to a horizontal excursion of 300 m for a stiff mooring. This change in the effective path length leads to a travel time fluctuation of 200 ms, the same order as the expected oceanographic signal. The travel time fluctuation due to the vertical excursion of the transceiver is much smaller. One might suspect that the shifting transceivers, and the change in the effective propagation range, may lead to a different set of acoustic multipaths connecting each source/receiver

pair. However, Cornuelle (1985) and Gaillard (1985) show that a change in the propagation length of a few kilometers or less does not compromise the multipath arrival structure, but only leads to a first-order translation in the actual arrival times.

During the tomographic experiment, the two northern moorings and the mooring situated furthest west (moorings 1, 2, and 3) underwent large vertical excursions, of more than 100 m in depth, leading to horizontal excursions of greater than 1 km. The corresponding travel time deviation would be the equivalent of a temperature deviation of 3°C over the entire leg, so it must be accounted for. Pressure records for tomographic moorings 2 and 4 are provided in Figure 3.8. The mooring 2 pressure record is typical of moorings 1, 2 and 3, and the mooring 4 depth record is typical of moorings 4 and 5. One extremely energetic event, evident near yearday 300, causes the transceiver of mooring 2 to dip almost 200 m in the vertical over a period of days. On several other occasions, vertical excursions of 30–50 m take place. On the other hand, mooring 4 remains relatively taut, with rms vertical excursions of less than 5 m over the experimental duration.

Several means are available to remove the unwanted mooring motion in the data records. In this study a static mooring motion model is used to estimate the location of the mooring during the experiment. Before discussing the model, a few comments concerning deep-sea moorings are made. Taut deep-sea moorings are in static equilibrium with horizontal currents for time scales of an hour or longer (Mark Grosenbaugh, personal communication). For low-frequency variations of a day or longer, the mooring can be assumed to be in static equilibrium at all times. If the current profile with depth is known from direct measurements, the mooring shape and motion can be inferred using a simple static equilibrium mooring model.

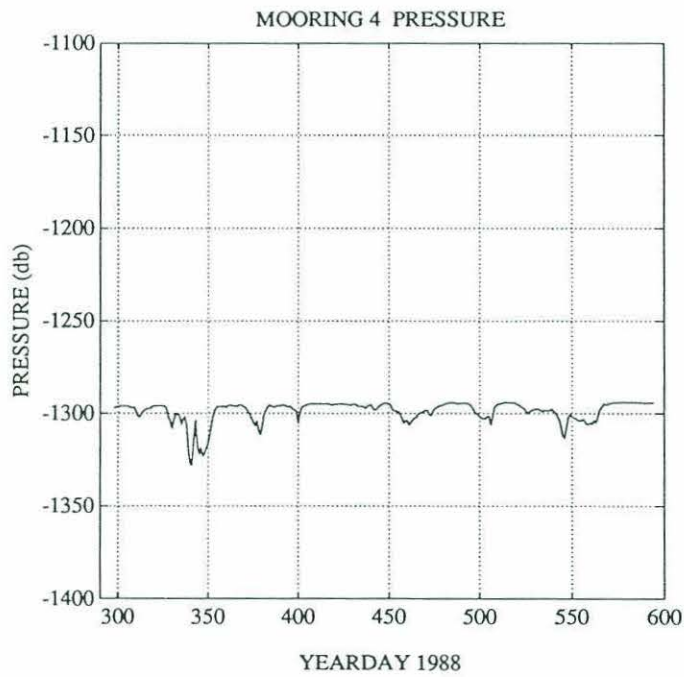
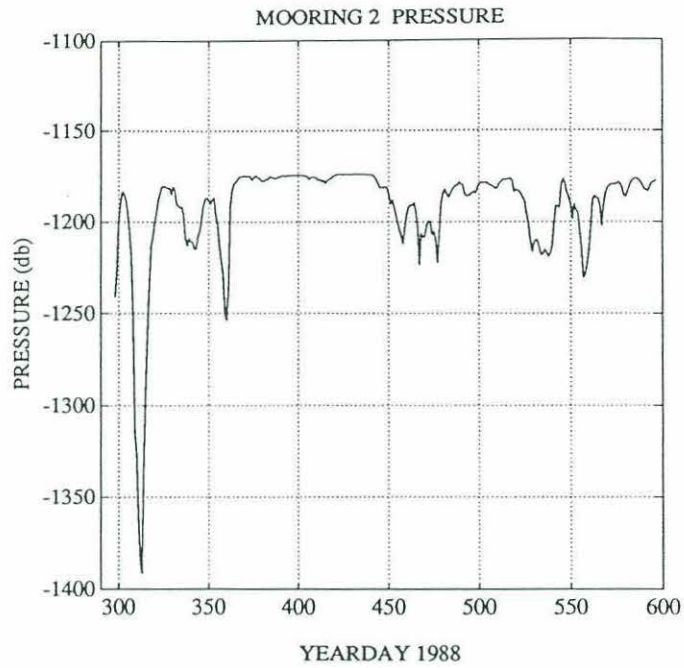


Figure 3.8: Tomographic pressure records for moorings 2 and 4. The data have been daily averaged from bihourly measurements.

A model applicable to the subsurface moorings used in deep ocean measurements at WHOI has been developed by Berteaux (1976) and Moller (1976). The mooring is specified by its individual components, which are in turn described by their length, buoyancy, and area. Drag coefficients are designated for the normal component and the tangential component of velocity. Each mooring component is acted upon by the tension vector of the component above and by the buoyancy and drag forces on the component itself. Static equilibrium is attained by a balance of the tension vectors and the buoyancy and drag forces at each component level.

A profile of the current velocity acting on the mooring is also required as input. For the velocity profile, contemporaneous current meter measurements from nearby current meter moorings are used. The location of the current meter moorings in relation to the tomographic moorings is provided in Figure 2.9. The current meter moorings are situated 10–20 km from the tomographic moorings. Only two levels were typically sampled by the current meters, with an upper instrument at 500 m and a deep instrument at 4000 m. Some of the current meter moorings also had instruments at 250 m, 1000 m, and 1500 m. The tomographic moorings were the subsurface type, with the tops extending to 1000 m beneath the ocean surface. They were thus completely isolated from the strong current velocities present in the upper thousand meters. Daily-averaged pressure records from current meter moorings compared favorably with nearby (within 15 km) tomographic mooring records. Thus, current velocities at the local current meters are assumed to be representative of the actual velocities experienced by the tomographic moorings.

Current meter velocities were linearly interpolated in depth to yield a current velocity profile over the full water column. The velocities were linearly interpolated in both magnitude and direction. The resulting profile was then used as input for

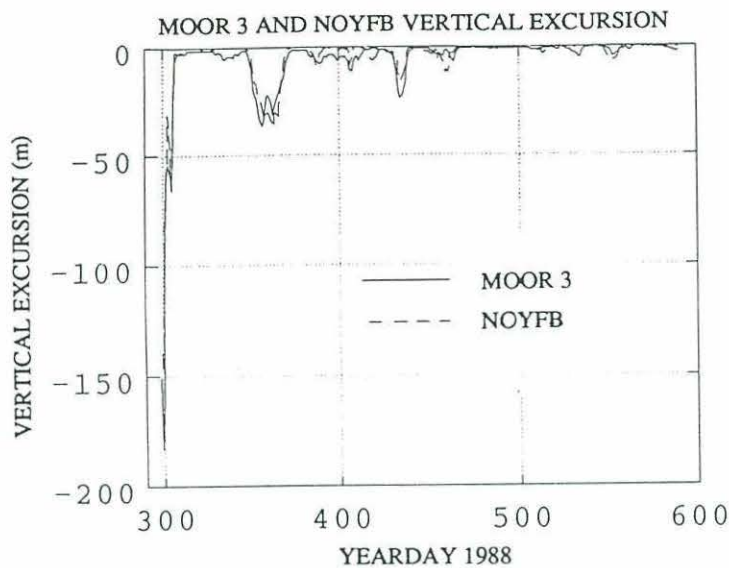


Figure 3.9: Comparison of observed mooring 3 transceiver depth excursion with NOYFB model predictions. The actual excursion is given by the solid line and the model prediction is given by the dashed line.

the mooring motion model. The model-output depth time series were compared with pressure gauge measurements from the tomographic transceivers. The agreement is fairly good over most of the record, as can be seen in Figure 3.9 for the case of mooring 3. However, the mooring motion program generally underpredicts the vertical dip for the very large excursions (greater than fifty meters in depth). The difference between the predicted mooring depth and the actual measured depth is more illuminating, and is shown in Figure 3.10. Excluding the large event at the outset of the experiment (yearday 300), the rms difference between the mooring motion-predicted depths and the actual measured depth is about 3 m. The more important measurement is the horizontal excursion. This is not measured *in situ*, but can be predicted by the mooring motion model. To the extent that the model accurately predicts the motion of the mooring, as is revealed by the goodness of fit of the predicted to the measured depths, we then have confidence that the model horizontal excursions are representative of the horizontal excursions actually experienced by the tomographic transceivers.

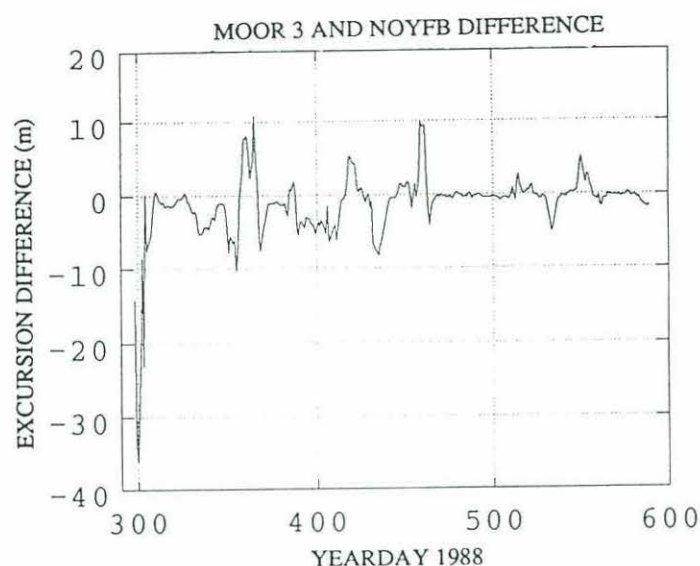


Figure 3.10: Difference of mooring 3 transceiver depth excursion and NOYFB model predictions. The rms difference between the model predictions and the observed vertical excursions is 3 m.

After running the model for all of the various moorings, it was found that all of the moorings behaved similarly under various current regimes. The moorings configurations are all nearly identical, with the instrument depths only varying by a few hundred meters in the vertical. For top-to-bottom (1000–5000 m) current velocities of less than 20 cm/s, the entire mooring remains essentially taut. For more energetic current velocities the mooring tilts from the vertical. The mooring remains almost vertical at the top. A regression curve was fit to the model-predicted depth excursion versus the model-predicted horizontal excursion for all of the moorings. This curve is shown in Figure 3.11, and is valid for the full range of velocity profiles encountered during the experiment for all of the moorings. The regression curve only tells us the radius of the watch circle. It is also necessary to know the direction that the mooring is pointed to pinpoint its location on the watch circle. The current measurements indicate that the velocities act in nearly the same direction from 1000 m depth to 4000 m for this region. The difference in the direction of the current meter velocities at 1000 m, and 4000 m was typically less than 20°. The

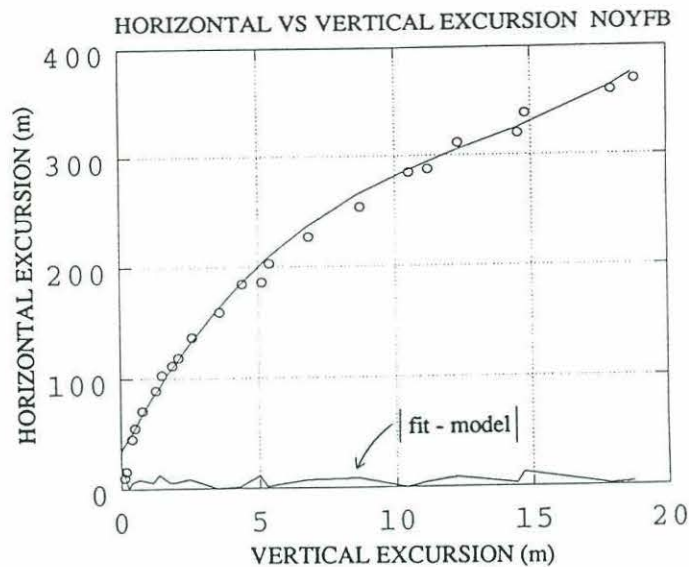


Figure 3.11: Mooring motion model-predicted regression curve for horizontal excursion versus vertical excursion. The circles represent model-predicted horizontal excursions as a function of vertical excursion. The curve represents a polynomial fit of the third degree to the data. The lower curve shows the absolute value of the difference between the fit and the model-predicted horizontal excursion.

direction of the transceiver on the watch circle can then be pinpointed to within a swath of 20° using only the measured current velocities at 4000 m. The subsequent error of the mooring motion-induced travel time signal is thereby decreased by an order of magnitude.

There is still some residual mooring motion error left in the data, but the signal is greatly reduced. Much of the mooring motion error is high-frequency, and daily averaging reduces the error level. The estimated daily averaged rms residual error in travel time due to mooring motion is roughly 10 ms after the correction. For the larger vertical excursions (> 40 m in the vertical) the residual error can be an order of magnitude larger than this, so the error bars for these days are correspondingly larger. This value must be added to the rms error of 1 ms when considering sum travel times, and hence the estimation of temperature, but does not enter in the estimation of differential travel times, or currents. Satellite navigation

systems are now capable of estimating positioning to a precision of approximately 1 ms (Steve Liberatore, personal communication).

3.6.4 Inverse Solution Errors — Resolution and Variance

Errors in the tomographic problem include not only errors due to the precision with which the travel time measurement can be made, but also resolution errors which arise from sampling of the medium by a limited set of acoustic multipaths. Only a few acoustic multipaths (typically one to seven) are resolvable and identifiable, and this small set of multipaths is used to characterize the full vertical structure of the water column. Resolution refers to the ability of the complete tomographic system, which includes both the measurements and the inverse procedure, to reproduce the true state. The observational system acts as a filter, oblivious to some structures of the true state while distorting and amplifying other features. The solution to the inverse problem is dependent on both the choice of the ocean model and the specified noise variances.

The resolution of the tomographic measurement is conveniently dealt with in the context of the singular value decomposition. The assumed ocean model used in this study consists of a layered ocean, which will be discussed in detail in Chapter 4. The inverse procedure acts to distribute the limited observations throughout the full model ocean in a consistent manner. For a given measurement error, the inversion tends to magnify the error in some layers while reducing it in others. The formal expected variance of the inverse solution (3.14) can be expressed as

$$\langle \hat{e}_i^2 \rangle = \sigma_i^2 \sum_{j=1}^k \frac{v_{ij}^2}{\lambda_j^2}, \quad (3.20)$$

where i is the layer number, j is the rank of the system, σ_i^2 is the variance of the observation, and v and λ are respectively the eigenvectors of the model parameter space and the eigenvalues. The uncertainty in the estimated model parameters is due to both errors in the measurements and the lack of resolving power of the system. The traditional tradeoff between resolution and variance is also exhibited. The resolution of the system is enhanced as smaller and smaller eigenvalues are kept (more high-frequency structure in the solution) at the expense of increased variance in the system. The variance of the estimated solution should be roughly the same size as the expected variance (see Wiggins, 1972). Estimates of the errors after passing through the inverse filter are typically the same order as the travel time measurement error, or ~ 1 ms for this experiment.

3.6.5 Discussion

We conclude this section with a discussion of the total error in the tomographic measurement, and the precision with which we can estimate the field variables, specifically temperature, current velocity and vorticity. The daily-averaged error in the travel time measurement is about 1 ms, excluding the mooring motion-induced error. Sum and difference estimates are formed from the reciprocal arrivals. The sum of the measurements is used in the estimation of sound speed (temperature) [see (3.5)]. The difference of the reciprocal measurements is used in the estimation of current velocity and relative vorticity [see (3.6) and (3.10)]. Mooring motion-induced errors are important in the sum travel times, and add an additional rms error of 10 ms to each travel time measurement. The inverse-estimated experimental errors are typically the same size as the travel time measurement errors.

Table 3.4 gives the precision with which the tomographic measurements of temperature, current velocity and relative vorticity are made for the SYNOP Gulf Stream tomography experiment. The errors in Table 3.4 are for range-averaged and daily-averaged estimates. Temperature can be estimated to an rms precision of only 0.1°C owing to the large residual mooring motion. Current velocities can be estimated with a precision of 3–5 cm/s, which is comparable to measurement errors in other instruments, such as the current meter. Areal-averaged relative vorticity can be measured to a precision of about 10^{-6} , which is more exact than any measure to date. Remember that the tomographic measurements considered in this study are indicative of range averages (over 100 to 200 km for each leg of the array), and are not estimates at a single point in space. Some portions of the tomographic records (less than 10%) have larger error bars owing to residual mooring motion error. Error bars for the various estimates will be provided in the following chapter.

Table 3.4: Precision of Tomographic Measurement

Temperature			
$\Delta \theta$ ($^{\circ}\text{C}$)	ΔTT_{θ} (ms)		
	L = 100 km	L = 200 km	
0.01	2.1	4.3	
0.05	10.7	21.3	
0.1	21	43	
1	213	427	
2	427	853	
Current Velocity			
Δu (cm/s)	ΔTT_u (ms)		
	L = 100 km	L = 200 km	
1	0.4	0.9	
2	0.9	1.8	
5	2.2	4.4	
10	4.4	8.9	
50	22	44	
Relative Vorticity			
$\Delta \zeta$ (1/s)	ΔTT_{ζ} (ms)		
	A = 10,000 km ²	A = 20,000 km ²	
10^{-7}	.22	.44	
10^{-6}	2.2	4.4	
10^{-5}	22	44	
10^{-4}	222	444	

Chapter 4. The Oceanographic Fields

4.1 The Ocean Model

The ocean model serves as the connection between the forward modeling of acoustic propagation and the inverse procedure of estimating the oceanic structure through measurements of acoustic multipath travel times. Equations (3.5) and (3.6) constitute the acoustic forward problem. Sum and differential travel times are calculated from continuous distributions of sound speed perturbations and current velocity, respectively. The corresponding inverse problem estimates the continuous fields from a discrete set of travel time measurements. This points out the underdetermined nature of the problem. It is convenient to parameterize the continuous fields with a finite number of parameters. An ocean model is chosen which will specify this parameterization in an oceanographically meaningful way. By using oceanographic prejudices (*a priori* information, dynamic constraints, reasonable length and time scales, *etc.*) to choose possible structures of the fields to be estimated, the indeterminacy of the problem is removed. The estimated solution is often somewhat sensitive to the choice of the ocean model and the assumed *a priori* variances, so care must be taken in their selection. The error estimates associated with the model are used to determine if the ocean model is consistent with the data.

For example, consider a simple range independent model of the ocean. The model parameters δc (or alternatively u) can be written

$$\delta c = \delta c(z) = \sum_j F_j(z) . \quad (4.1)$$

The $F_j(z)$ can be layers, empirical orthogonal functions, dynamic modes, such as quasi-geostrophic modes, *etc.* Substituting (4.1) into (3.5),

$$\delta T_i^+ = - \int_{\Gamma_i} \frac{\sum_j F_j(z)}{c_{oj}^2} ds . \quad (4.2)$$

For the layered case (4.2) becomes

$$\delta T_i^+ = - \frac{R_{ij}}{c_{oj}^2} F_j , \quad (4.3)$$

where R_{ij} is the arc length of ray i in layer j .

The choice of the ocean model leads to a specification of the inverse operator. The acoustic multipaths determined by ray tracing are matched with corresponding arrivals in the pulse response data. This procedure is generally referred to as ray identification. The ray identifications for case S2R5 is shown in Figure 4.1. Note that only a small subset of the predicted ray arrivals are stable and resolved well enough to be able to be identified. The rays arriving earliest correspond to the steepest refracted rays, cycling between near-surface depths and deeper portions of the water column. Later arriving rays tend to have shallower trajectories, and are confined to near-sound channel axis depths.

A range independent, layered model was chosen for the analysis in this thesis. The range independent model will only yield a single, average estimate of the horizontal structure of the slice connecting each source/receiver pair for each layer considered. The paucity of crossing paths and small number of resolved acoustic

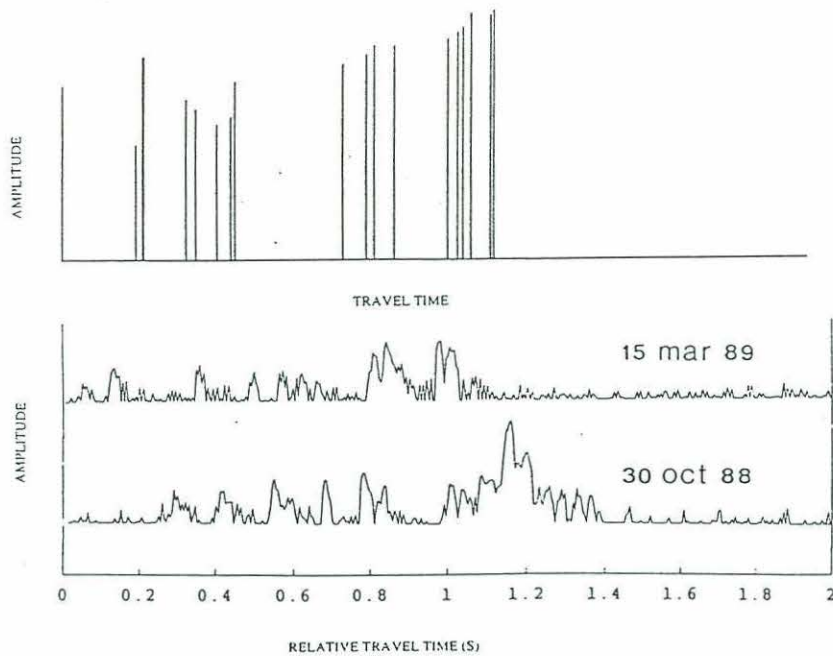


Figure 4.1: Ray identification for S5R2. The upper panel is the arrival time versus intensity pattern predicted by ray theory and the lower panel represents a sample of the daily-averaged actual acoustic arrival time versus signal-to-noise ratio data. The labeling above the ray theory prediction represents the depths of the upper and lower turning points of the calculated eigenrays.

multipaths for this experiment led to this choice. A model ocean of twelve layers has been assumed with closer spacing in the surface layers than at depth. The model ocean, with the identified multipaths connecting moorings 2 and 5, is shown in Figure 4.2. The vertical resolution in the upper 1000 m ranges from 100 m to 300 m with depth. Beneath 1000 m the resolution decreases from 400 m to 800 m at 4000 m depth. The inverse operator kernel is determined by the layered spatial coverage of the ray paths for a given source/receiver pair. Layer sound speed perturbations and current velocities are then estimated from the acoustic travel time measurements.

The next step in the inverse procedure is the specification of model and data covariances. The model covariance is considered first. The inverse procedure requires some knowledge of the structure of the solution. This parameterization is

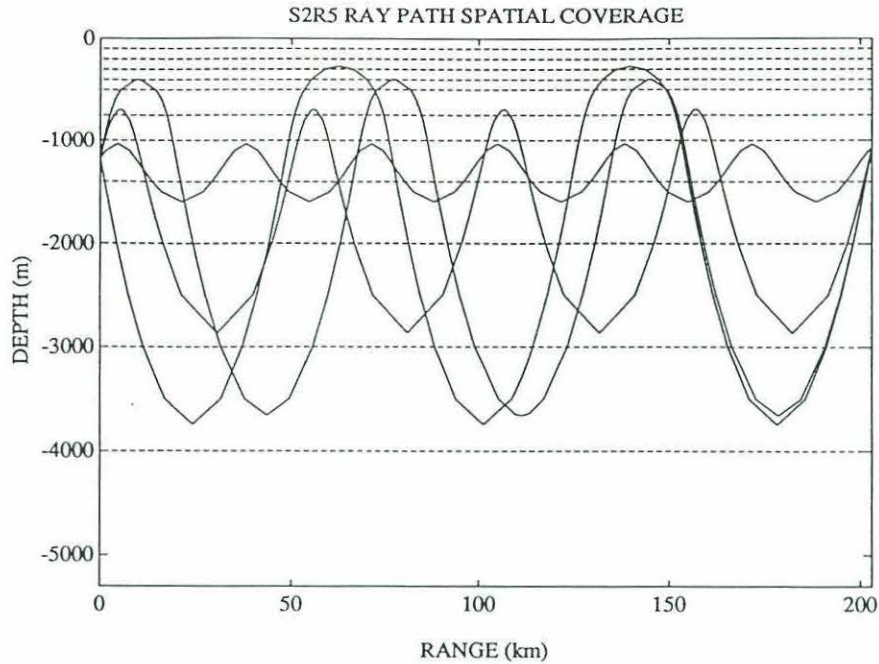


Figure 4.2: The ocean model and ray path spatial coverage for case S2R5. Four stable and identifiable eigenrays connect moorings 2 and 5 at a range of 203 km. Note that no rays penetrate the upper 100 m or depths beneath 4000 m.

generally based on *a priori* considerations. Most of the ocean eddy variability, and consequently the sound speed variability, is surface intensified in the upper 1000 m. We would thus expect an inverse solution to have a similar characteristic vertical structure. This structure can be imposed on the solution by specifying the model covariance matrix. Layers are weighted so that the vertical scale is not simply the geometric scale, z , but rather a dynamic scale determined by eddy motions.

This leads to an interesting issue in the tomographic problem. The refractive nature of mid-latitude sound channels leads to acoustic rays which cycle between the upper and lower ocean. Ray loops tend to be longer in the deeper ocean owing to less ray curvature (as the sound speed gradient is less than in the upper ocean). The paths are thus more sensitive to fluctuations beneath the sound channel axis, in the deeper water. However, typical oceanic fluctuations tend to be surface intensified. The mismatch between the shallow dynamic waveguide and the deeper acoustic

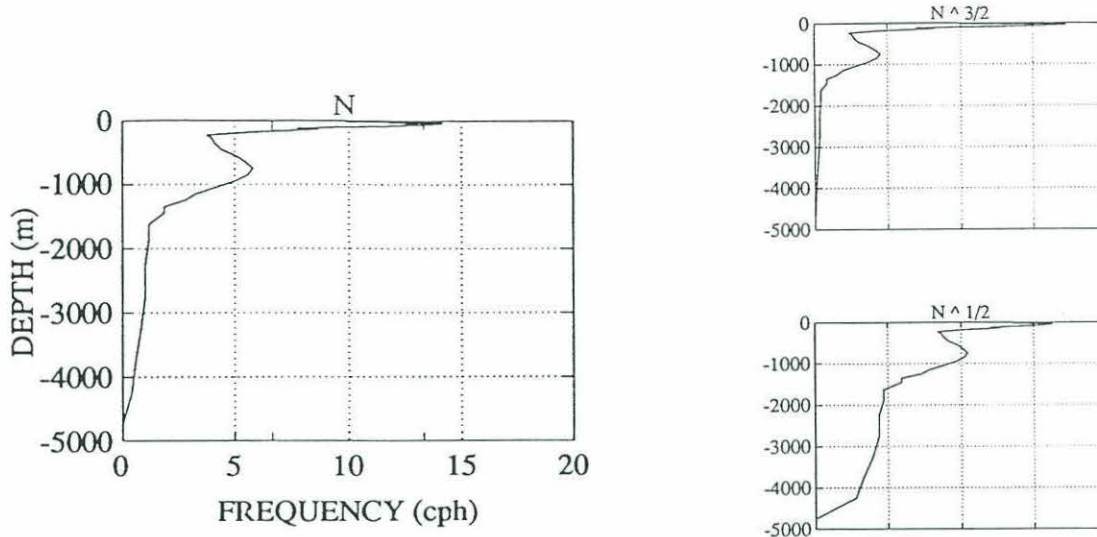


Figure 4.3: Buoyancy frequency profile $N(z)$ from Levitus climatological data. Profiles for $N^{3/2}$ and $N^{1/2}$ are also shown.

waveguide leads to interesting ramifications regarding vertical resolution [see Munk and Wunsch (1982)]. If no vertical weighting is imposed on the solution, the system yields unacceptably large errors in near-surface estimates. We thus adopt an a priori vertical weighting of the solution variance which expresses the belief that more variability is expected in the surface and thermocline depths than in deeper regions.

Most of the ocean eddy variability is confined to the surface and thermocline depths in the ocean. A convenient measure of such variability is the Brünt-Väisälä frequency, N^2 , which is proportional to $\partial\bar{\rho}/\partial z$ where $\bar{\rho}(z)$ is the average vertical density profile. The buoyancy frequency profile determined from the Levitus climatological data is given in Figure 4.3. The buoyancy frequency is surface intensified, with a subsurface maximum at thermocline depths. Beneath 1000 m the profile decays rapidly to near-zero values.

In order to accurately model the real ocean, we have imposed an $N^{3/2}$ ($N^{1/2}$) weighting for the vertical structure of the expected noise variance for temperature (current velocity). Profiles for $N^{3/2}$ and $N^{1/2}$ are shown in Figure 4.3. This vertical structure is in accordance with WKBJ scaling theory (Richman *et al.*, 1977). Alternatively, we could have constructed vertical modes (dynamical modes or empirical orthogonal functions) to describe the vertical structure of the field. Inversions have been performed using empirical orthogonal functions (the empirical orthogonal functions corresponding to the barotropic and first two baroclinic modes contain roughly 95% of the variance in this region), and yield results quite similar to those using the buoyancy-scaled weighting. The absolute energy level of the weighting of the model covariance matrix is not important — it is the relative weighting in each layer that is important.

Both the model covariance matrix and the data covariance matrix have been assumed to be diagonal for the inversions considered herein. The data covariance matrix simply consists of the travel time error variances. The inverse operator kernel and the data covariance matrices are tailored to each day for a given source/receiver pair. Some days have more identified multipaths than others, and error variances vary from day to day, mostly due to residual mooring motion errors. The inverse operator is therefore specific to each day considered, even though the covariances were specified without time dependence. Data and model parameters are assumed uncorrelated from day to day. Mesoscale features in the ocean certainly have correlation time scales longer than the two-day separation of the inverse estimates. The inversions can be improved by including time dependent covariance functions and using Kalman filter techniques [see *e.g.*, Ghil *et al.*, (1981)]. This has not been done

in this study as the specification of realistic time dependent covariances is not a trivial exercise.

4.2 Temperature

Estimates of range average temperatures are considered in this section. The temperature structure in the vertical slice is calculated from the sum of reciprocal travel times. The linear relationship between the sum of reciprocal travel time measurements and sound speed perturbations is given by (3.5). The conversion of sound speed to temperature will be considered below. Absolute travel times can be used to estimate the complete sound speed field. Perturbation travel times, referenced to the basic sound speed state of the ocean, yield estimates of the fluctuations of the sound speed field about this state. As mentioned in the previous chapter, the absolute travel time measurements often contain large errors owing to large uncertainty in the precise location of the un navigated transceivers. However, the reference sound speed state is well known for the region so this poses little problem. In addition, the mesoscale variability of the region is of more interest to us than the exact mean field.

Sound speed is a non-linear function of temperature, pressure and salinity, increasing with an increase in any of these variables. A linear relationship between temperature and sound speed, such as that given in (3.7), is valid over large portions of the ocean. The temperature effect on sound speed is more pronounced than that of salinity. A 1°C change in the temperature of the water is roughly equivalent to a 5 m/s change in the sound speed. A 1 psu change in salinity only alters the speed of sound by ~ 1 m/s. A linear relation given by $\delta c = 4.6\delta\theta$ was used

for the conversion of sound speed to temperature. The estimated conversion factor varied from 3.5 to 4.8 for the temperature range encountered during the Gulf Stream tomography experiment, with the mean constant of proportionality being 4.6.

Estimated temperature anomalies for leg 2↔5 of the tomographic array are presented in Figure 4.4. Temperatures are representative of daily-averaged range average temperatures spatially integrated over a range of 180 km. Leg 2↔5 of the tomographic array is situated predominantly in the north-south direction. Only the upper 2500 m of the water column is shown. Resolution beneath 2500 m depth is very poor and the estimated structure shows very little variability. The full time series spans nearly ten months. The temperature anomaly field has a fairly simple structure, with much of the variability in periods of the order of one month. Most of the anomalous events are quite coherent with depth. Note the presence of strong cooling events, particularly those occurring in November, 1988 and April, 1989. These intense events coincide with the passage of cold-core rings which have been shed from the Gulf Stream and have migrated through the tomographic array. This result is supported by satellite infrared imagery for these periods (see Figure 4.5). The maximum temperature anomalies are of the order of 3°C in the surface waters. Temperature slice inversions for other source/receiver pairs show similar structure to that seen for leg 2↔5, with variability dominated by events with periodicities ranging from 20–50 d.

A comparison of the tomographic temperature measurement has been made with an independent measurement. Figure 4.6 shows a comparison of the estimated temperature for leg 2↔3 of the tomographic array with the temperature measured by the average of two temperature thermistors located on moorings 2 and 3. The temperature thermistors were situated at a nominal depth of 1200 m, so the tomo-

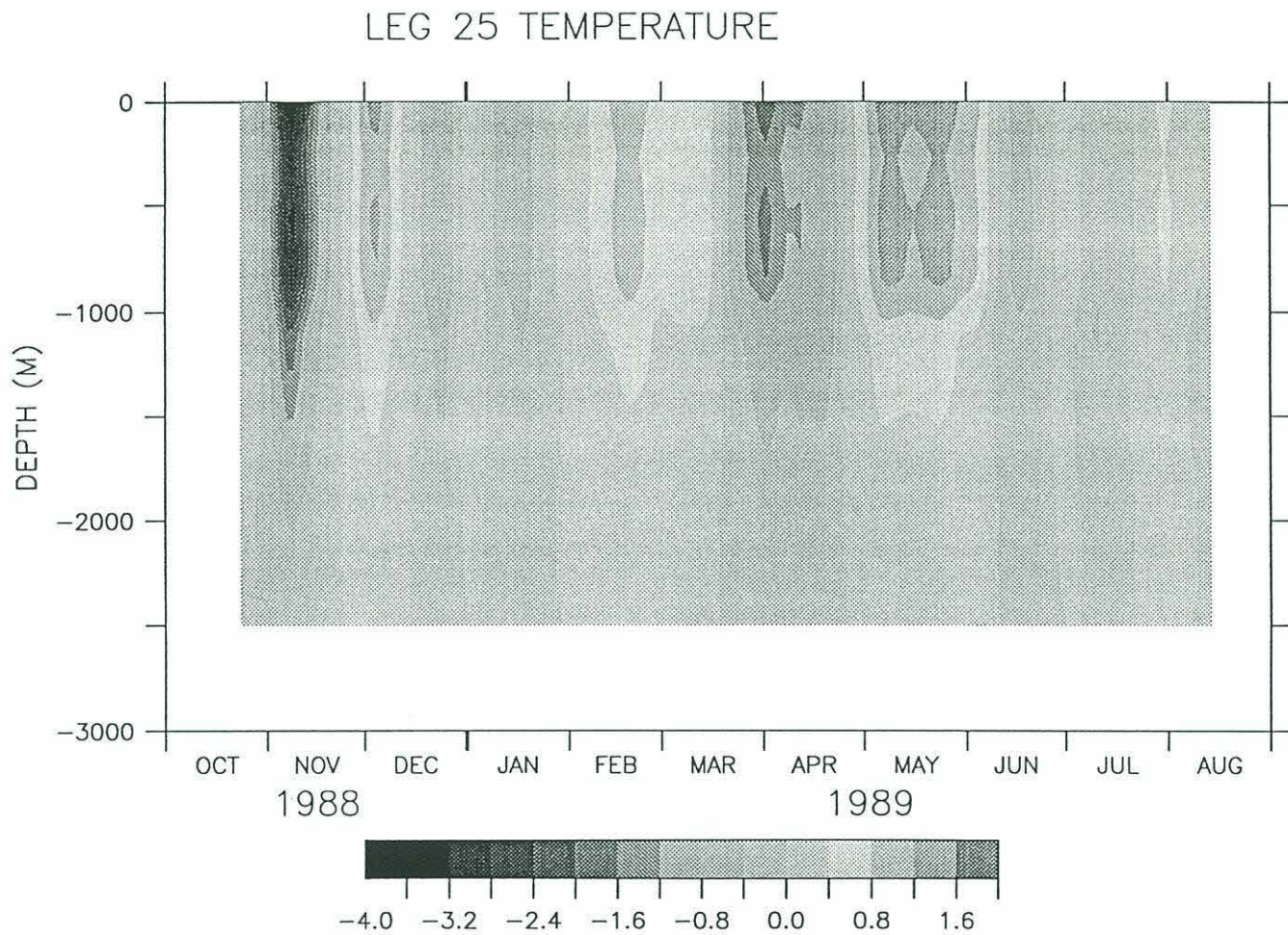


Figure 4.4: Estimated temperature anomaly for leg 2↔5. This leg is situated predominantly in the north-south direction and spans a range of 180 km

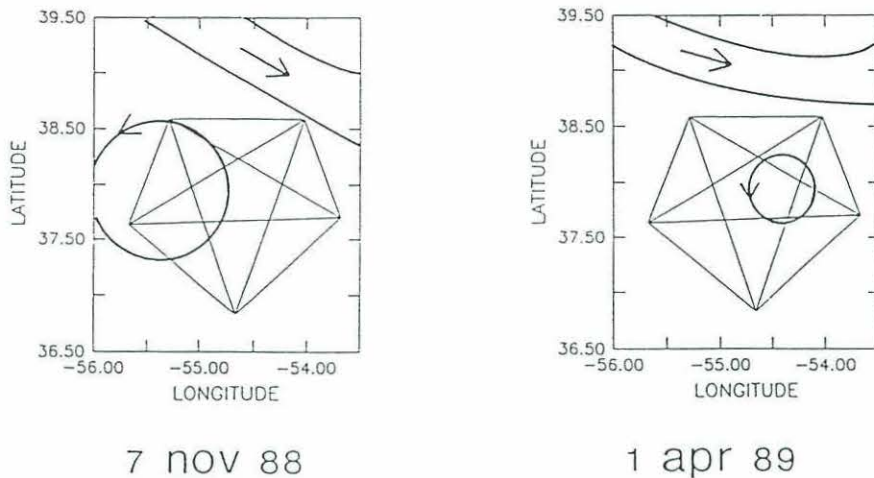


Figure 4.5: Satellite sea surface IR (temperature) maps for November 7, 1988 and April 1, 1989. The maps have been drafted from the surface maps generated by NOAA.

graphic estimated temperature for the layer between 1000 and 1400 m is used for comparison. The average for the thermistors is simply the arithmetic mean of the two records. The mean temperature field (5.9°C at this level) has been added to the estimated temperature anomalies to produce absolute temperatures. The comparison is favorable over most of the 300-day record. Error bars for the daily average of the two thermistor point measurements are estimated at $\pm 0.03^{\circ}\text{C}$. The error for the tomographic measurement varies with time, with larger errors corresponding to periods when larger residual mooring motion errors exist in the data. The rms error for the tomographic measurement is 0.1°C for daily average estimates.

An alternative view of the frequency content of the variability is obtained via the estimation of power spectra. Temperature power spectra are plotted in log-log form for both a tomographic estimate and a current meter temperature thermistor estimate in Figure 4.7. The 300-day records have been chopped into 128-day pieces, windowed with a Hanning filter, and overlapped. The spectra shown in Figure 4.7 are for the tomographic estimate of temperature at 1000 m depth for leg 2 \leftrightarrow 5, and

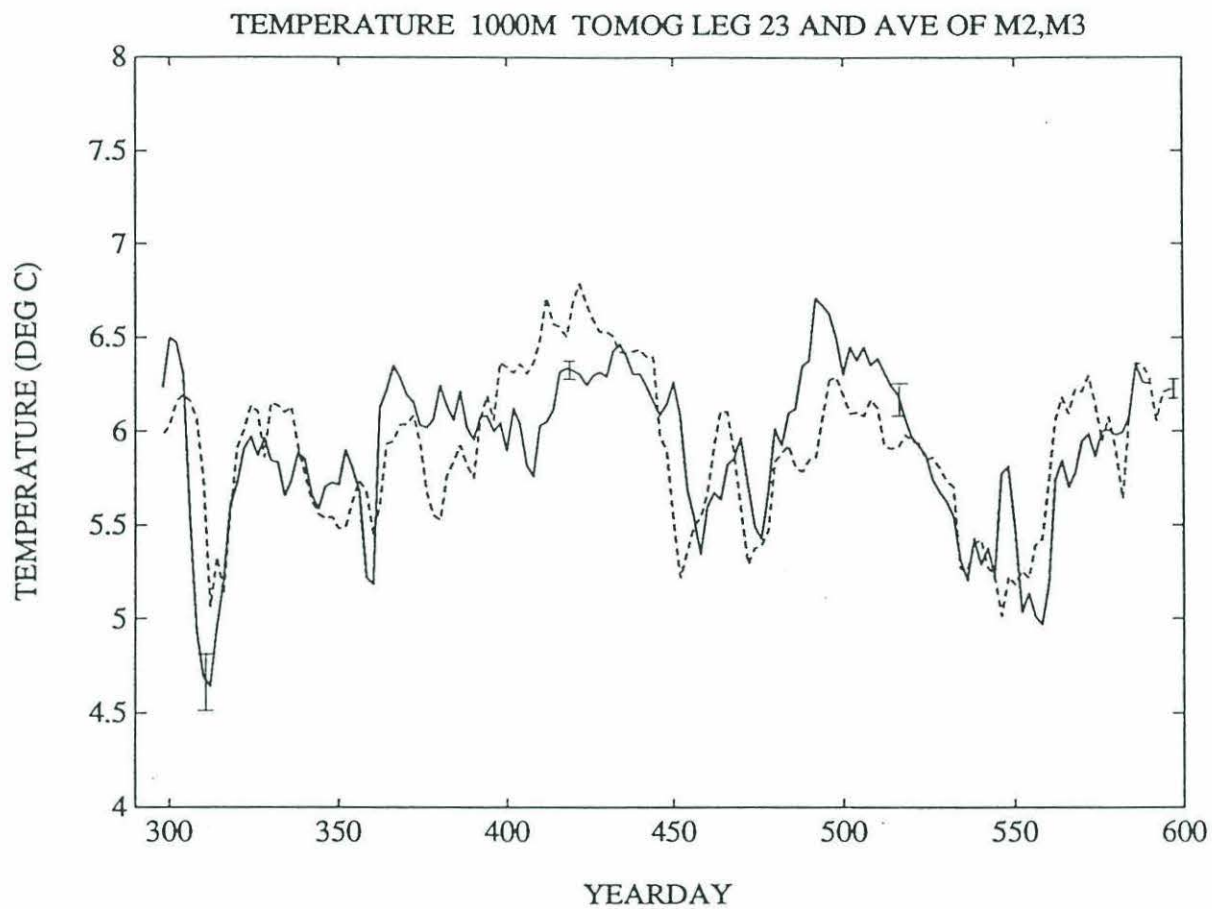


Figure 4.6: Comparison of inverse-estimated temperatures for leg 2↔3 of the tomographic array with the temperature measured by the average of two temperature thermistors at moorings 2 and 3, at a depth of 1200 m. The tomographic estimate is given by the solid line and the current meter measurement is given by the dashed line.

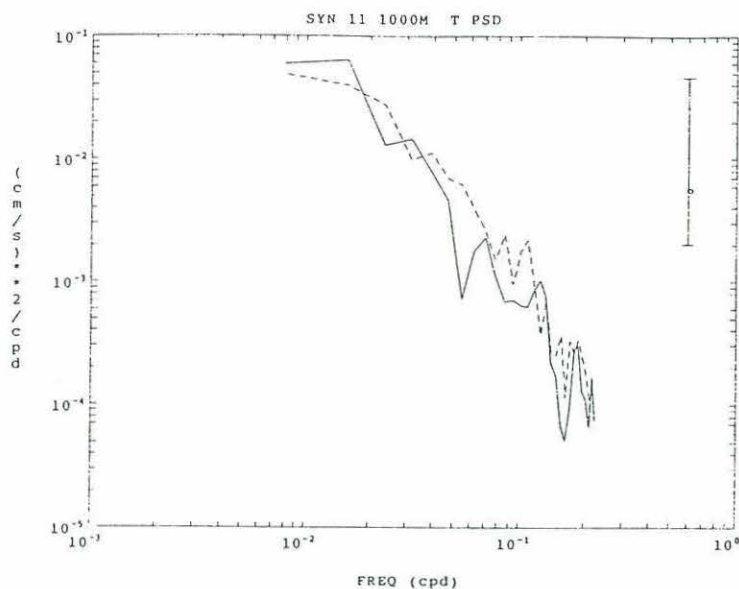


Figure 4.7: Temperature power spectra at 1000 m depth. The solid curve is the temperature power spectral energy from the tomographic measurement, and the dashed curve is that determined from current meter temperature measurement.

for the spectrum calculated from the current meter mooring positioned at the center of the tomographic array (mooring 11). Also included are 95% confidence limits. The confidence limits are quite large due to the limited number of degrees of freedom. The tomographic measure is a spatial integral over the field while the current meter measure is a point measurement. One expects the tomographic measurement to filter out small spatial scales of motion (small relative to the separation between transceivers). The spatial filtering leads to lower tomographic energy levels at the higher frequencies, which tend to be dominated by shorter scales of motion. The spatial covariance of the temperature field has typical correlation length scales of 100–150 km in the region (Bower and Hogg, 1991). Thus, the two different measurements do not differ appreciably in their energy content, except at high frequencies, where the point measurement contains more energy.

4.3 Current Velocity

Estimates of range average current velocities are considered in this section. The current velocity in the vertical slice is calculated from the difference of reciprocal travel times. The linear relationship between the difference of reciprocal travel time measurements and absolute current velocity is given by (3.6). It is important to point out that the tomographic measure is not sensitive to the full velocity field, but only the velocity in the plane of the slice connecting the source/receiver pair. Flow normal to this plane has no effect on the measured acoustic travel times.

Estimated current velocities for leg 3↔4 of the tomographic array are presented in Figure 4.8. Leg 3↔4 of the tomographic array was chosen as it is aligned with nearby current meter moorings 10, 11 and 13. Estimated current velocities are representative of the daily-averaged range average u -component of velocity spatially integrated over a range of 170 km. Leg 3↔4 of the tomographic array is situated predominantly in the west-east direction. Only the upper 2500 m of the water column are shown. The full time series spans nearly ten months. The velocities are coherent with depth over most of the record. The currents are most energetic in the near surface, with maximum velocities approaching 50 cm/s for the range-averaged estimate. As was the case with the temperature field, the variability is dominated by low frequency periodicities, with most of the energy occupying the mesoscale band with periods ranging from 30 d to 100 d.

A comparison of the tomographic estimate of velocity with current meter measurements at a nominal depth of 500 m is provided in Figure 4.9. The current meter estimate is representative of the average u -component of velocity at 500 m depth for three current meters aligned with leg 3↔4 of the tomographic

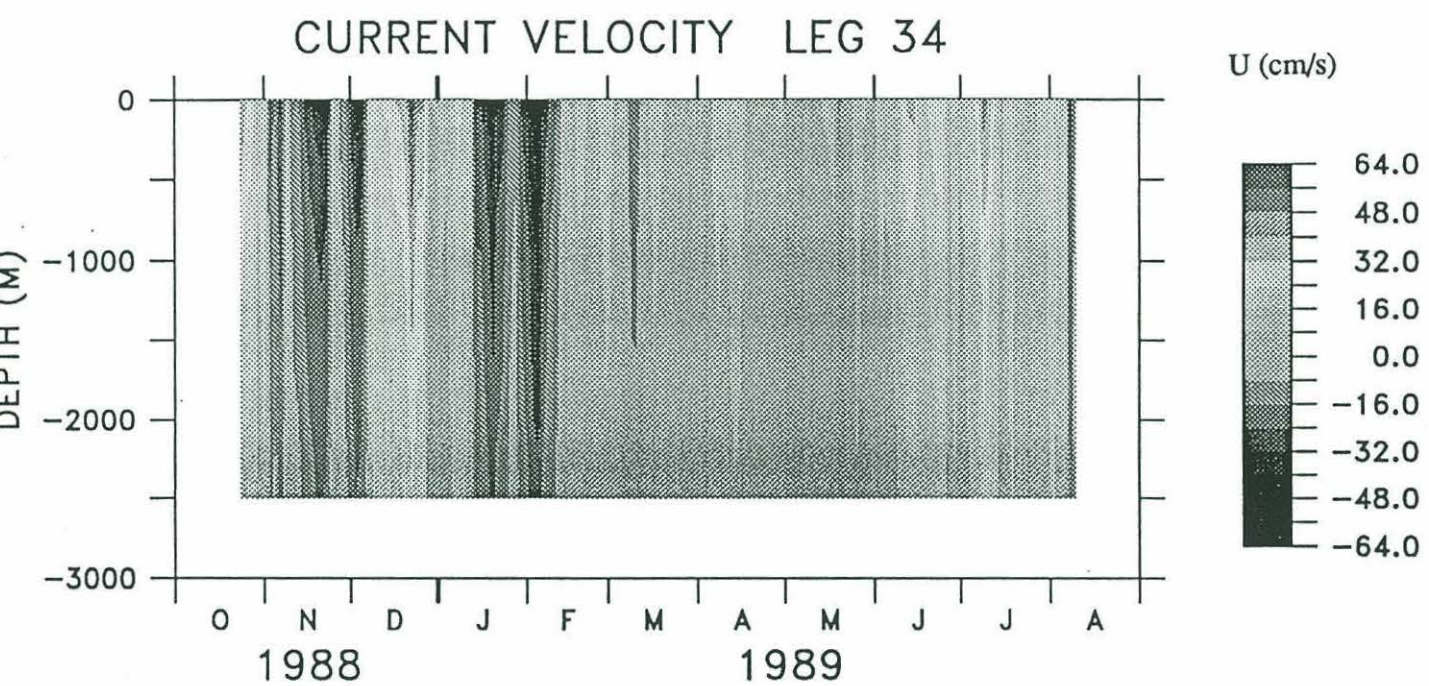


Figure 4.8: Estimated current velocity for leg 3 ↔ 4. This leg is situated in the east–west direction and spans a range of 170 km

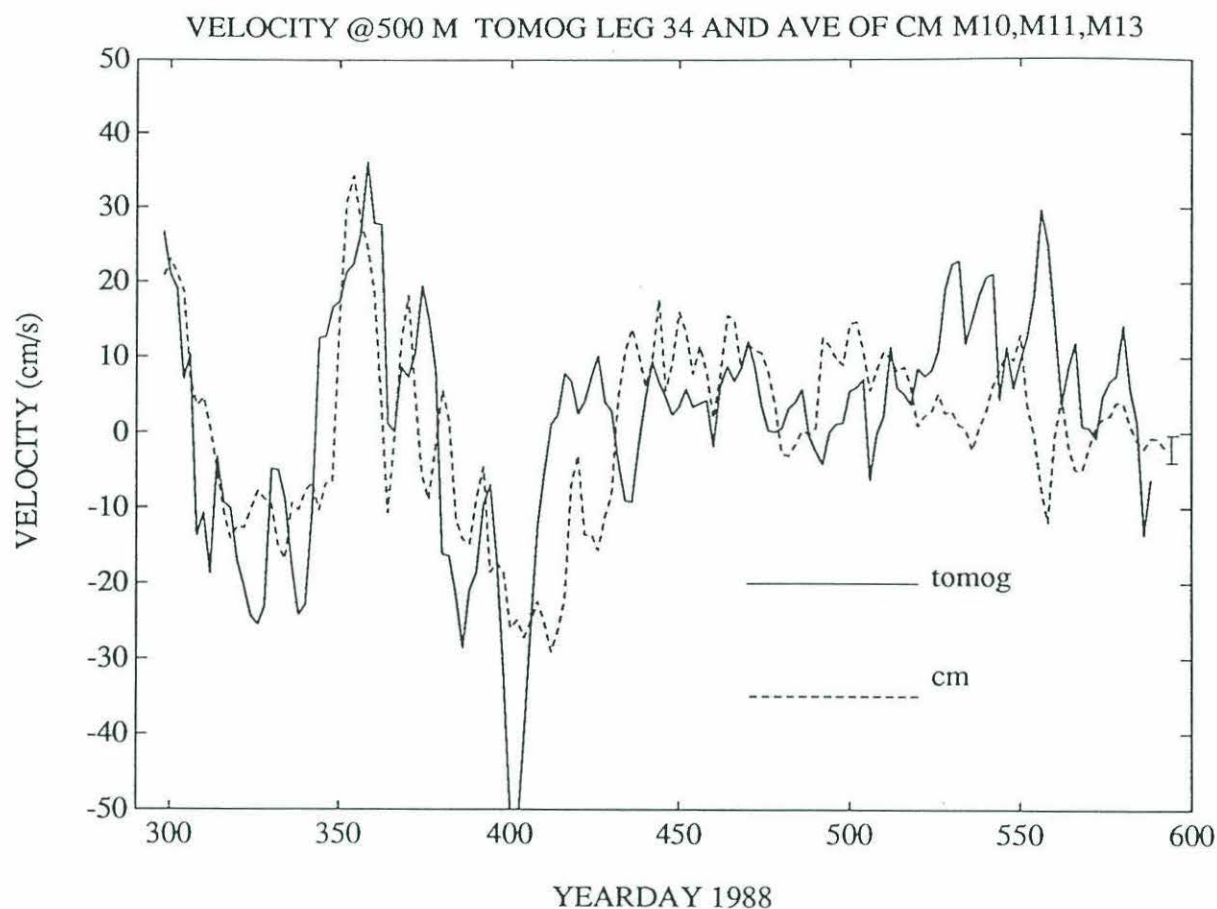


Figure 4.9: Comparison of tomographic measurement of velocity with an average of current meter velocity data. The comparison is made for leg 3↔4 (at a range of 170 km and situated in the west-east direction) and the u -component of velocity for the average of three measurements aligned with this leg, at a depth of 500 m. The tomographic estimate is given by the solid line and the current meter measurement is given by the dashed line.

array (moorings 10, 11 and 13). The two independent estimates of current velocity compare favorably over the entire record. The error in the tomographic estimate is nearly constant with time. The error is not constant over the full record due to sporadic dropout of identified ray paths. This leads to changes in the resolution error of the order of 1 cm/s. The rms tomographic error is 3 cm/s, which is comparable to that for the current meter velocity measurement (Hogg, personal communication). Comparisons with single point estimates of velocity are not as good. Figure 4.10 shows a similar comparison as in Figure 4.9, only this time the current meter at the center of the leg (mooring 11) is the only measure used for the comparison. This is a direct comparison of the spatially-integrated tomographic measurement of velocity and a point measurement. The current estimate from the tomographic measurement is less energetic than the estimate taken from the single current meter measure. The low-frequency variability is still similar for both measures. This is more clearly seen by looking at the coherence of the two independent measurements (see Figure 4.11). The two measurements are generally coherent at the 95% confidence level for motions with periodicities greater than 20 d, and typically less coherent at higher frequencies.

Velocity values generated from a numerical model are also used to compare with the tomographic estimates of velocity variability. The numerical model used in the comparison of the velocity and vorticity measurements with the tomographic data is a quasi-geostrophic, eddy-resolving regional model of the Gulf Stream system (Antonietta Capotondi, 1993). The model consists of five layers in the vertical, with inflow/outflow boundary conditions. The model is spun up to statistical equilibrium with the Hellerman and Rosenstein wind stress climatology. The model domain is shown in Figure 4.12, where the climatological (five-year) mean of the surface layer

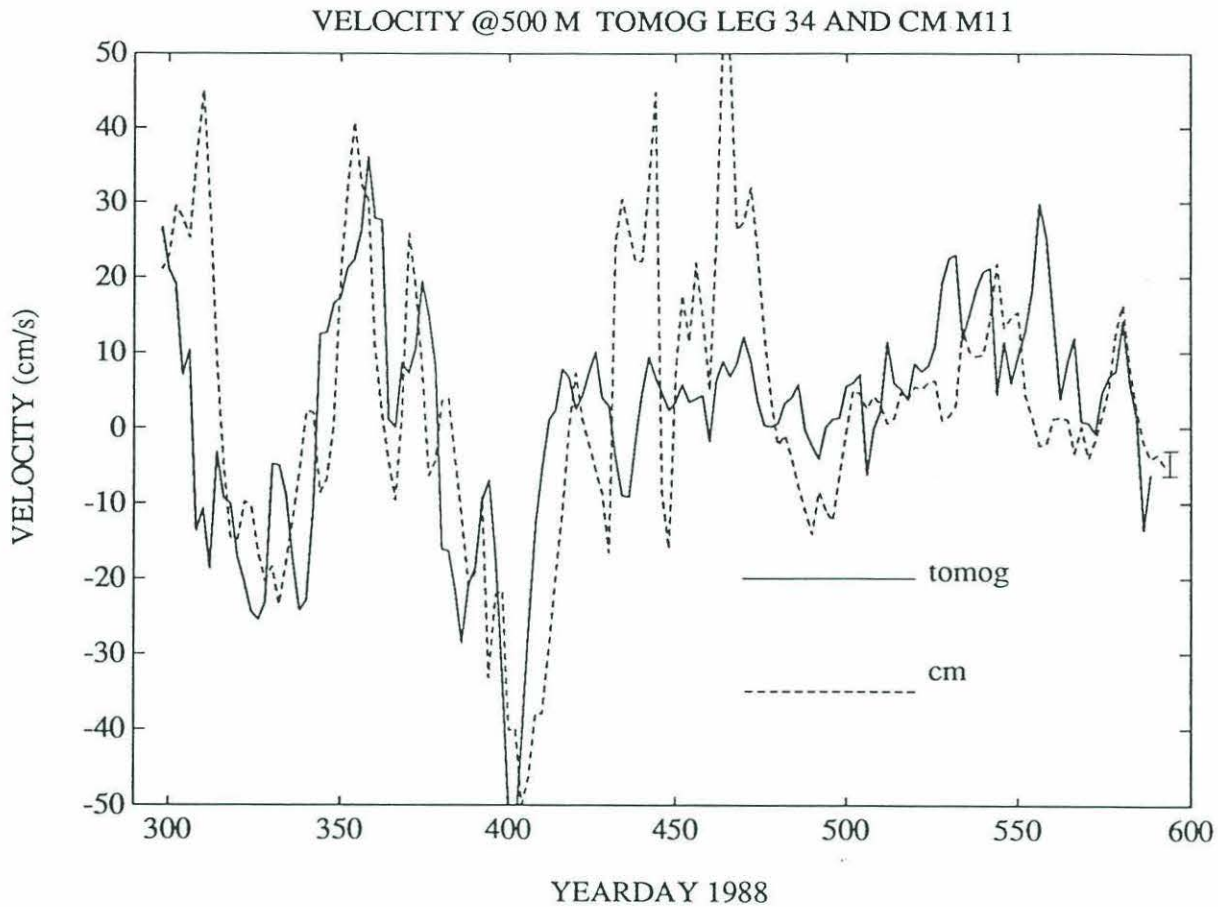


Figure 4.10: Comparison of tomographic measurement of current with a single current meter measurement. The comparison is made for leg 3↔4 (at a range of 170 km and situated in the west-east direction) and the u -component of velocity taken from the central current meter mooring, at a depth of 500 m. The tomographic estimate is given by the solid line and the current meter measurement is given by the dashed line.

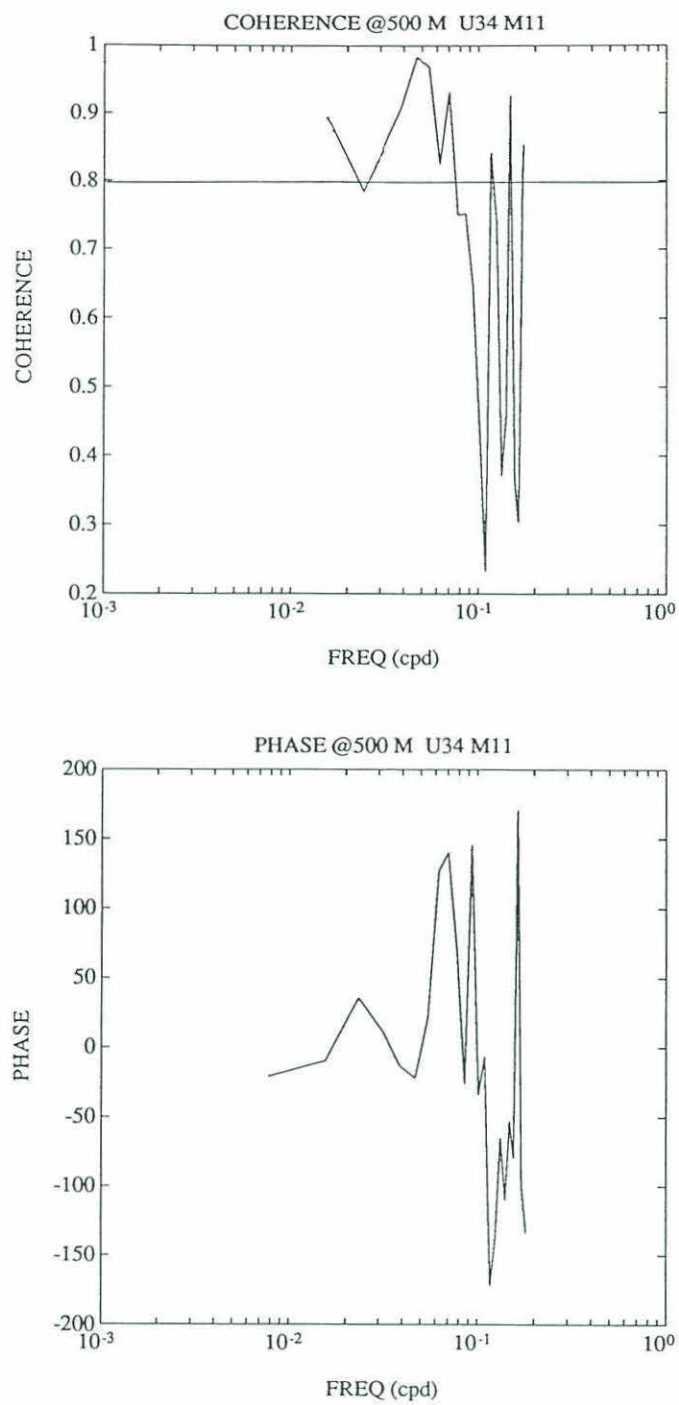


Figure 4.11: Coherence between the tomographic and current meter measurement of velocity, at a depth of 500 m. The comparison is made for leg 3↔4 and the u -component of velocity taken from the central current meter mooring. The 95% confidence limit is given by the solid line.

UPPER LAYER MEAN STREAMFUNCTION

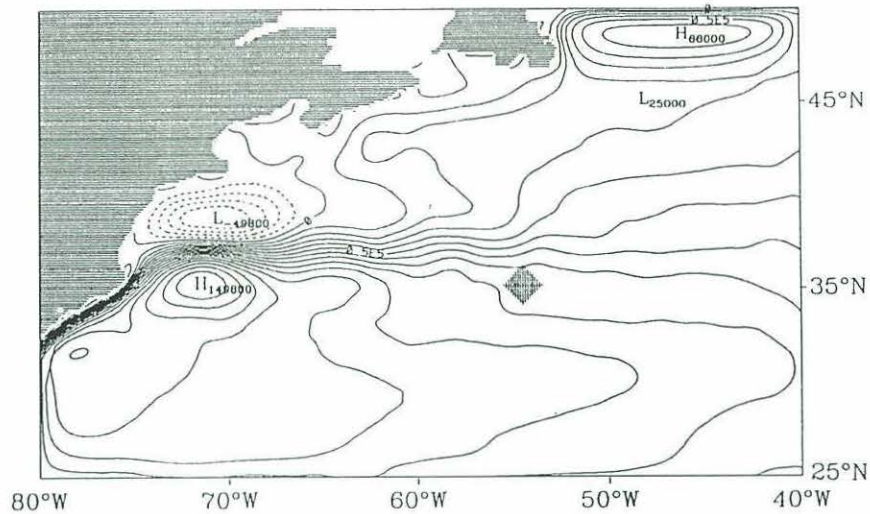


Figure 4.12: Surface streamfunctions for the quasi-geostrophic numerical model domain. The artificial tomographic array has been situated with the same proximity to the western boundary jet as in the real ocean.

streamfunction is presented. Also shown is the location of an artificial tomographic array in the model domain. The model has been used in assimilation experiments of the Geosat altimetric data set (Antonietta Capotondi, 1993). We chose to compare the model estimates of velocity and vorticity spectra with the corresponding field estimates as the numerical model has been shown to have quite realistic mesoscale statistics.

A spectral comparison of velocity variance from three independent measurements — the tomographic measurement, current meter measurements and numerical model values, is now considered. The specific comparison for the spectra of the u -component of velocity determined from the different measurements is shown in Figure 4.13 for a depth of 1000 m. The tomographic record is representative of the spatial average over a range of 170 km for leg 3↔4. The current meter record used in the estimate is that of the u -component of velocity for the instrument located at the midpoint of the leg (mooring 11). One-year-long (after spin-up) time series

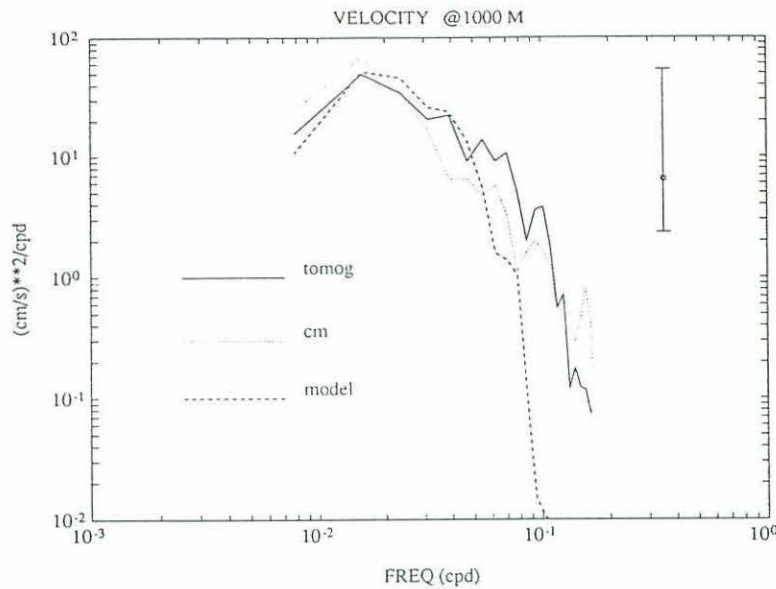


Figure 4.13: Velocity power spectra at 1000 m depth. The solid curve is the velocity power spectral energy from the tomographic measurement, the dotted curve is that determined from current meter record for the u -component of velocity, and the dashed curve is that determined from numerical model values of the u -component of velocity.

have been obtained in the model by evaluating daily averages of velocity components (u, v) at the model grid point in the center of the artificial tomographic array. The numerical model record consisted of a 300-day record of the u -component of velocity. The energy content of all three independent measurements is roughly comparable at low frequencies. The 95% confidence limits are again large owing to the limited degrees of freedom. Energies are peaked in the mesoscale band, with maxima at a period of 64 days. At higher frequencies the tomographic measurement is somewhat less energetic than the current meter measurement. The lower tomographic energy levels are attributed to the integrating nature of the measurement. For periods less than 10 d, the numerical model velocity variances are unrealistically small, most likely due to excessive dissipation in the system.

4.4 Vorticity

Estimates of areal average relative vorticity are considered in this section. The circulation about an enclosed region is obtained by summing the current velocities along the periphery of the region. From Stokes theorem, the line integral of fluid velocity is equal to the areal-averaged relative vorticity of the region. The linear relationship between the cyclic summation of the difference of reciprocal travel time measurements and areal-averaged relative vorticity is given by (3.10).

Estimates of areal-averaged relative vorticity for the region bounded by moorings 2, 3, 4 and 5 is presented in Figure 4.14. The estimated relative vorticity is representative of the daily-averaged areal average relative vorticity of an area comprising nearly 20,000 km². The relative vorticity field is dominated by energetic events which are fairly coherent with depth and have periodicities of the order of a month or so. There is less coherence with depth for the relative vorticity field than is evident in the velocity field. Also, enstrophy variability exists on shorter temporal scales than was evident with the temperature and velocity estimates.

A time series of relative vorticity at a depth of 1000 m is considered in further detail (see Figure 4.15). The record has a near-zero mean ($-1.1 \times 10^{-6} \text{ s}^{-1}$) with fluctuations about the mean being an order of magnitude larger. The ambient planetary vorticity at this latitude is $\sim 9 \times 10^{-5} \text{ s}^{-1}$. Two events (labeled 1 and 2) are specifically highlighted in the time series. While event 1 is only moderately strong, event 2 has the highest value of positive (cyclonic) relative vorticity throughout the ten-month record. Both of these events indicate the presence of cold-core cyclonic rings, as depicted in Figure 4.5. During event 1 the ring is exiting the array (as it migrates westward) and is only partially covered by the quadrilateral 2-3-4-5.

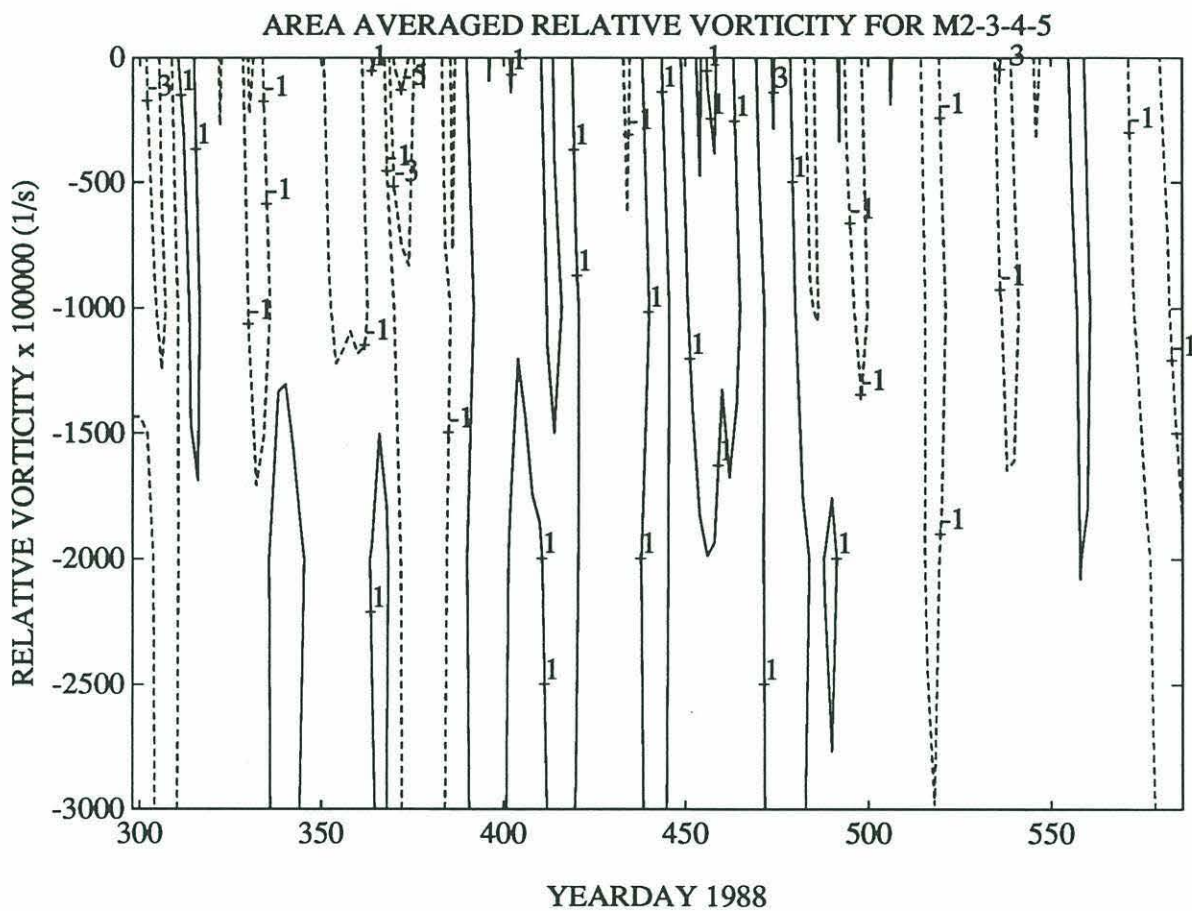


Figure 4.14: Estimated relative vorticity time series for the region enclosed by tomographic moorings 2, 3, 4 and 5. The area enclosed by this region is roughly 20,000 km².

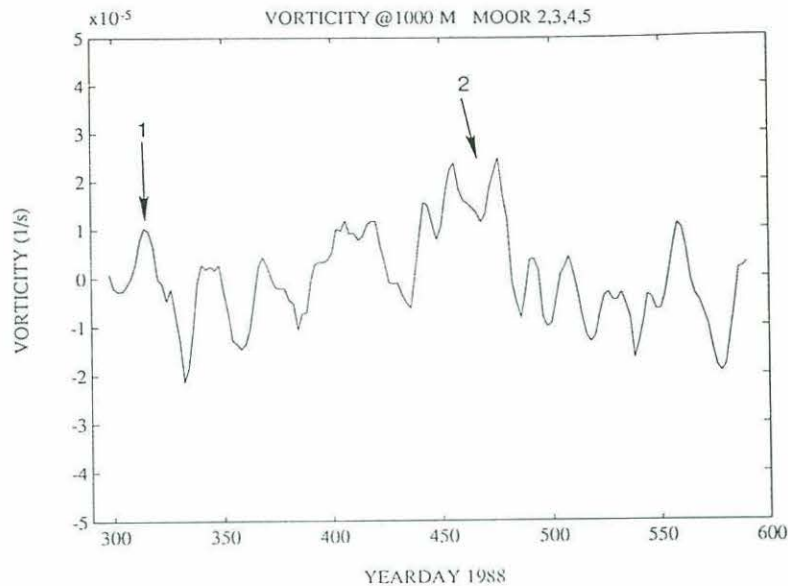


Figure 4.15: Time series of vorticity at a depth of 1000 m. The record shown is for the quadrilateral region comprised of moorings 2, 3, 4 and 5. Events labeled 1 and 2 correspond to anomalous cold events pointed out in Section 4.2.

During event 2 the ring is fully embedded in the quadrilateral, hence the stronger positive relative vorticity peak shown in Figure 4.15. Error bars for the relative vorticity signal are also included in the figure. The variations in the vorticity estimate are significant as the rms vorticity error level is $\sim 4 \times 10^{-6} \text{ s}^{-1}$.

The measurement of relative vorticity in the ocean has traditionally been a very difficult one to make. Two approaches are considered to evaluate the relative vorticity from current meter measurements. First, the vorticity is estimated from its definition, $dv/dx - du/dy$, by the finite differencing of the velocity components situated in a cross-pattern. This estimate contains large errors due to the differentiation of two terms which are of comparable magnitude, leaving a small residual. A comparison between the tomographic estimate and this current meter estimate of relative vorticity is illustrated in Figure 4.16. The two curves represent the tomographic estimate for the area encompassed by moorings 2, 3, 4 and 5, and the current meter estimate using the east-west and north-south pairs of instruments

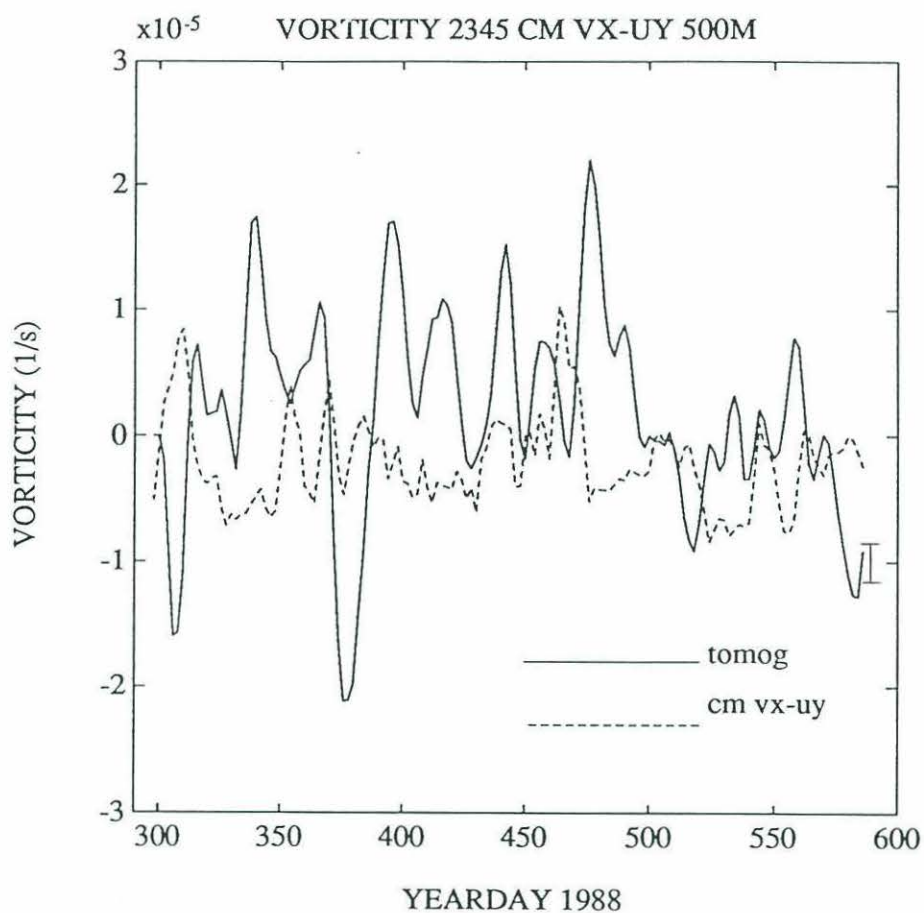


Figure 4.16: Comparison of tomographic estimate of relative vorticity with current meter estimate of $dv/dx - du/dy$. The tomographic estimate is given by the solid line and the current meter estimate is given by the dashed line. The rms error for the vorticity measurement is also provided to the right of the plot.

closest to the tomographic moorings (moorings 10, 13, 9, and 12). Current meter mooring 12 had no instrument at the 500 m level, but did have an instrument at 250 m. The 250 m depth velocity record at mooring 12 was scaled down using the shear calculated from the mooring 11 records at 250 m and 500 m. The net change was typically less than 1 cm/s. There is very little similarity between the two estimates of relative vorticity, and no significant cross correlation value.

A second procedure which more closely mimics the tomographic line integral is attempted with the current meter data. At the current meters located on the periphery of the tomographic quadrilateral (moorings 9, 10, 12, and 13) we project the velocity vector along the line joining the current meters. The entire circulation around the quadrilateral is then estimated from the measurement at four individual points. A comparison of the tomographic estimate of relative vorticity for the region bounded by moorings 2, 3, 4 and 5 and this second estimate using the four current meters at a depth of 500 m is provided in Figure 4.17. The two records have no significant correlation.

A spectral comparison of the various relative vorticity estimates is now made. The comparison is for the tomographic measurement, a current meter measurement, and relative vorticity calculated from the numerical model. The numerical model estimate is that of the average relative vorticity for the region within the model tomography array (see Figure 4.12). The spectral comparison is shown in Figure 4.18. The three spectra all have similar low-frequency enstrophy content. The numerical model spectrum has very little energy at frequencies less than 15 days in comparison with the tomographic and current meter estimates. The current meter estimate, based on the second estimate of relative vorticity from the current meter measurements, has more high-frequency energy content (greater than 15 d

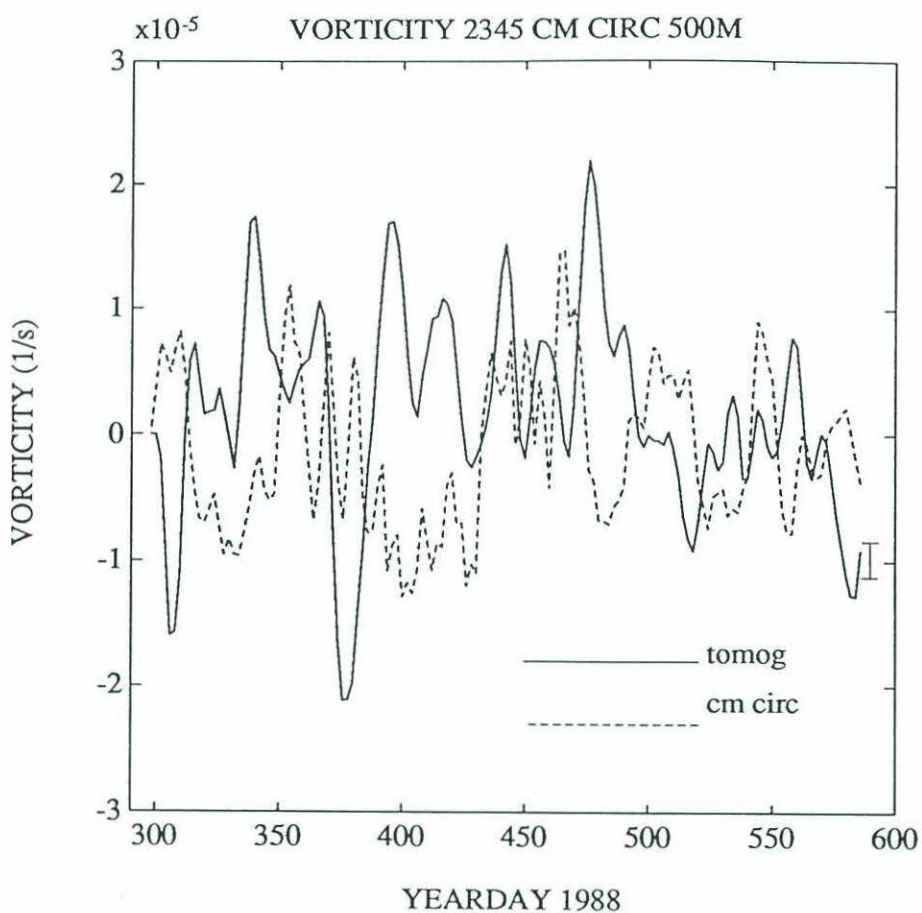


Figure 4.17: Comparison of tomographic estimate of relative vorticity with current meter estimate of the circulation. The tomographic estimate is given by the solid line and the current meter estimate is given by the dashed line. The rms error for the vorticity measurement is also provided to the right of the plot.

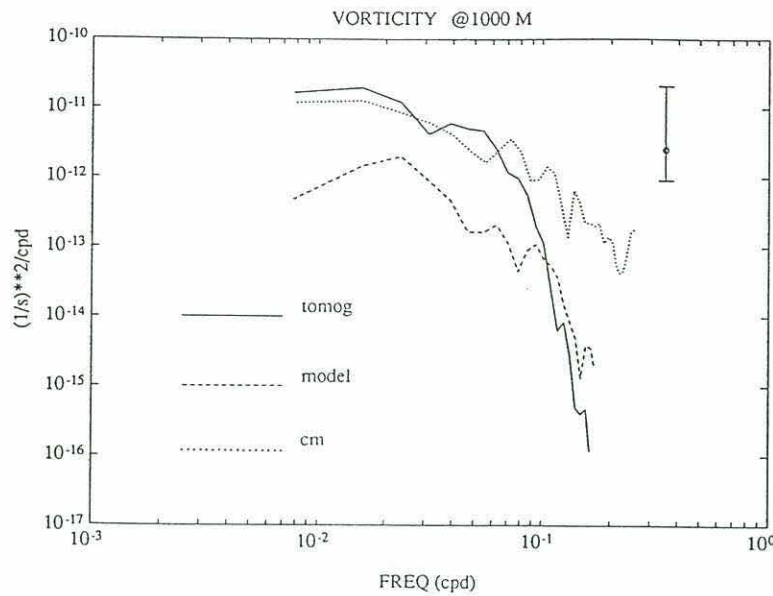


Figure 4.18: Spectral comparison of relative vorticity estimates obtained from tomography, current meter and numerical model.

periodicities) than the tomographic estimate. The spatial averaging inherent in the tomographic measurement suppresses the high-frequency energy which is not filtered by the projection of the current measurements at four individual points.

A few more remarks should be made regarding the comparison of the inverse-estimated vorticities with the numerical model estimates. Spectra have been compared at six levels in the vertical (from the surface to a depth of 2000 m). Spectral comparisons were made for both the average vorticity of a region the size of the tomographic array and a single model point measurement situated in the center of the artificial tomography array. The numerical model estimates have too little energy (in comparison with the tomographic estimates) in all layers except the surface layers, which are in direct contact with the surface forcing. This suggests that the coupling between the model layers is too weak, most likely attributable to excessively large dissipation used in the model.

4.5 Discussion

Tomographic estimates of temperature, current velocity and relative vorticity fields have all been shown to be quite energetic. Variability is dominated by scales of motion ranging from roughly 20 d to 100 d. This preponderance of low-frequency energy is clearly manifest in the spectral properties of the estimates. Spectra calculated at various levels in the vertical (from the surface to 4000 m) all exhibit the typical red nature of the spectrum, which is characteristic for motions in this region [see *e.g.*, Richman *et al.*, (1977)].

The tomographic estimates provide much better resolution of the vertical structure of the region than has been previously attained. The enhanced vertical resolution is attributed to the sampling of the water column by several ray paths (typically 2 to 5). Most of the energetic events have been shown to be quite coherent with depth. This has also been shown to be the case with current meter measurements. Cold-core rings are also present in the region for a substantial portion of the 300-day data record, and their signature is clearly present in temperature and vorticity estimates. This is an exciting result, and could be of use for periods when infrared satellite imagery is not available, such as occurs when cloud cover is present. In addition, rings or coherent structures without a surface expression are not detected by the satellite measurements, which only sample the very surface regions. On the other hand, the tomographic measurement samples most of the water column. The two measurements are truly complementary, and the utility of acoustic tomography in estimating the vertical structure of ring events, with good resolution, has been demonstrated.

Comparison of the tomographic measurement with contemporaneous data, primarily current meter data, and numerical model data, also points out some interesting results. The spatially-integrating tomographic measurement has similar energy content as other field estimates for motions with periodicities greater than 20 d. These low-frequency events usually are dominated by motions with larger spatial scales. Estimates of correlation length scales for temperature and velocity in this region typically range from 100 to 150 km, so the utility of tomography in averaging over many individual correlation lengths has not been demonstrated in this experiment due to the short propagation ranges (100 to 200 km). However the tomographic measurement does average over many of the higher frequency motion events, which typically have smaller spatial scales of motion. This is clearly demonstrated in the various spectral comparisons. The tomographic results presented in this chapter also show that errors in the tomographic estimates, based on the model statistics, are now nearly the same as the errors inherent in more conventional instrumentation.

The daily-averaged time series introduced in this chapter will be exploited to investigate the energetics and dynamics of the region in the following chapter.

Chapter 5. Statistics and Dynamics

5.1 Introduction

Experimental evidence accumulated in the northwestern Atlantic shows that the eddy potential and kinetic energy densities increase by orders of magnitude when proceeding from the basin interior towards the Gulf Stream (Wyrski *et al.*, 1976; Dantzler, 1977; Schmitz *et al.*, 1983). This places the tomographic array in one of the most energetic regions of the subtropical gyre. In the Gulf Stream System this high eddy variability has been linked to change in atmospheric forcing, change in topography, and instabilities of the Stream itself producing wave radiation into the interior (Schmitz *et al.*, 1983 and Wunsch, 1983). The near-field region of the Gulf Stream, somewhat loosely defined here as the region within 100 km of the Gulf Stream axis (of the order of several Rossby radii), is often dominated by the lateral meandering of the Stream. Cold-core cyclonic rings are often expelled from the Stream in the region downstream of the New England Seamount Chain. The rings then become embedded in the large-scale westward recirculation south of the jet.

The mean ocean circulations have been fairly well documented by now. The previous two decades have focused on a characterization of the low-frequency field of motion throughout the ocean. Much progress has been made toward this goal. Altimetric measurements have provided a good first-order description of the variability of the global surface waters (*e.g.*, Nerem *et al.*, 1990). More recently, an important focus of oceanographic research has been on the effect of low-frequency variability on the time-mean circulation. Mesoscale eddies contribute to the mean

potential vorticity balance through the potential vorticity flux, in a combination of lateral momentum transfer and vertical momentum transfer. Such fluctuations are important for the dynamics and thermodynamics of large-scale circulation and parameterization of their heat and momentum fluxes is essential for the development of realistic models.

Until recently, the observational data base has been fairly sparse in the region, consisting largely of CTD stations, current meter measurements and SOFAR float trajectories. Only the gross structures of the region have been surmised. Two earlier experimental studies (Local Dynamics Experiment (LDE) at 30°N , $69^{\circ}30'$ and Polymode Array 2 at 36°N , 55°W) have looked in some detail at the dynamics of the southern recirculation gyre. The LDE array was situated roughly 500 km from the Gulf Stream axis, and thus can be considered in the far field of the Gulf Stream. The Polymode array had moorings positioned 100 km to 300 km to the south of the Stream axis, thus partly situated in the near-field region. In both experiments, eddies were found to gain energy by converting available potential energy contained in the large-scale flow into eddy energy (Bryden, 1982 and Hogg, 1985). Bryden also found that the eddies lose energy in their interaction with the mean currents, as evidenced by an up-gradient eddy momentum flux. There is no local conversion of eddy energy into mean kinetic energy, and he thus concluded that the eddies do not locally drive the mean flow. From the Polymode current meter data set Hogg (1983) found that both the lateral and vertical momentum fluxes are important in driving the recirculation gyre. The vertical momentum flux dominates the lateral momentum flux in the region just south of the Gulf Stream axis at 55°W (north of 36°N). From a detailed analysis of the LDE current meter measurements, Brown *et al.*, (1986) estimated the quasi-geostrophic eddy potential vorticity flux

at a mid-thermocline depth and found that eddies in this portion of the gyre tend to reduce the mean potential vorticity gradient. However, the 225-day time series was too short to reliably estimate the divergence of the eddy fluxes.

Bower and Hogg (1992) have compiled a statistical description of the western North Atlantic using the available current meter data throughout the region. Eddy variability and momentum fluxes have been estimated at a standard depth of 4000 m. North of the Gulf Stream they find conclusive evidence of barotropic wave radiation away from the Stream for motions with periods of 50–250 d. South of the Stream, they find less conclusive evidence of a wave radiation signal at low frequencies. The lack of a barotropic wave-radiation signal is possibly attributed to the presence of baroclinic instability in the westward return flow, masking the radiation signal from the Stream itself. Tai and White (1990) find a much more consistent pattern of positive momentum fluxes south of the Kuroshio Extension from an analysis of altimetric sea level measurements.

Numerical modeling results have also proven quite useful, especially in pointing out the importance of the fluxes of heat, momentum and vorticity in maintaining the large-scale circulation patterns observed in the region. Numerical experiments suggest that the divergence of the eddy fluxes can force the deep circulation (Holland and Rhines, 1980). They also suggest that the vertical flux dominates the lateral flux in the recirculation region.

The estimation of energies and cross-covariances of the property fields, such as heat and momentum fluxes, is necessary for a complete statistical description of the region. From estimated second-order statistics of the region, it is important to ascertain the dominant periodicities of the motions which contribute to the bulk of

observed eddy fluxes. The divergence of the eddy fluxes is of dynamical significance in driving the large-scale circulations. If the divergence of the eddy momentum and heat fluxes can be estimated, then the issue of how the eddy motions contribute to the large-scale momentum and heat balances can be addressed.

The presence of strongly inertial, tight recirculation cells both to the south and to the north of the Stream has been known for some time now (Hogg *et al.*, 1986; Hogg, 1988; Holland and Rhines, 1980). Can the eddy Reynolds stresses, *i.e.*, the divergence of the eddy potential vorticity flux, induce a mean recirculation south or north of the Stream? Theoretical studies and numerical simulations provide well-known examples of eddy-driven recirculation cells (Hogg, 1988; Malanotte-Rizzoli *et al.*, 1992; Holland and Rhines, 1980). Diagnostic tools capitalizing upon the estimates of eddy fluxes can be used to prove that the source of the eddy energy found in the far field is indeed the Gulf Stream itself. Recent theoretical studies have focused on the transient behavior of Gulf Stream meanders, whose life cycles are characterized by growth and decay periods, and amplitude pulsations. These stochastic meander motions excite transient pulses of Rossby waves, and this transient part of the response is capable of radiating energy away from the source and assumed to be responsible for the observed eddy energy in the far field (Malanotte-Rizzoli *et al.*, 1987; Hogg, 1988; Malanotte-Rizzoli *et al.*, 1992).

The focus of this chapter is on a statistical description of the northern extremes of the southern recirculation gyre at 55°W. The vertical distributions of range-averaged temperature, velocity and vorticity fields was discussed in the previous chapter. To investigate the specific issues addressed above, mean and eddy kinetic energies, and eddy momentum and heat fluxes are estimated for the tomographic measurements for the region. This represents the first use of tomographic

measurements to estimate second-order statistics. Owing to the integrating nature of the tomographic measurement, an unique perspective of the statistics is obtained.

The evaluation of second-order statistics from tomographic measurements differs somewhat from the approach which has primarily been used with current meter observations. The discrepancy arises from the disparity between the slice measurement and the point measurement. For each slice connecting a source/receiver pair, tomographic measurements of range-averaged temperature and along-path current velocities are estimated. From these estimates of temperature, means and fluctuations about the mean have been calculated. Second-order statistics, such as mean and eddy kinetic energy, and heat and momentum flux, have been calculated. The interpretation of these quantities is considered in detail in the following section.

The next section is devoted to a discussion of the estimated kinetic energies and eddy fluxes. A comparison of the tomographic estimates with current meter estimates at two levels in the vertical is provided. In an attempt to understand the dynamics of the energetic low-frequency fluctuations and their relation to the general circulation, the potential vorticity equation is considered in Section 5.3. Some insight into the dynamics of the region is obtained with the aid of the Eliassen-Palm flux diagnostic presented in Section 5.4. A discussion section then follows.

5.2 Statistics of the Region

From the tomographic estimates of temperature, current velocity and areal-averaged vorticity, means and fluctuations about the mean have been calculated. Kinetic energies and eddy momentum fluxes are estimated for the 300-day period

from October 1988 through August 1989. The energy estimates are representative of the average energy content over the entire array.

A few remarks are now made concerning the estimation of momentum and heat fluxes from the tomographic measurements. The estimate of current velocity is solely for the component in the plane connecting the instruments. Any flow normal to this plane is not sensed by the tomographic measurement. As a consequence, momentum fluxes cannot be calculated using a single slice-measurement. To estimate the momentum flux from the range-averaged velocities, the covariance of velocities from two crossing slices is calculated (*i.e.*, velocities from a leg oriented in the east–west direction and velocities from a leg oriented in the north–south direction). This estimate of the momentum flux is actually made by two separate legs, and is representative of the flux due to large-scale averaged velocities. For heat flux, the estimate is for the flux of heat in the plane connecting the source/receiver pair, and does not yield two components owing to the insensitivity of the tomographic measurement to velocities normal to this plane. An estimate of the relative vorticity flux can be determined by calculating the covariance between the areal-average vorticity with a slice estimate of velocity. The exact interpretation of a measurement like this is not obvious, but it does present a unique view of integral properties of the region.

Errors in the estimated statistics must also be considered. The sampling errors address the error in the estimate due to a finite record length. The sampling error variance about the mean is equal to the variance divided by the number of degrees of freedom in the record. The number of degrees of freedom is equal to the number of integral time scales in the data record. A value of ten days, estimated from integrating the correlation functions using 300-day record length current meter

measurements of temperature and velocity, was estimated for a typical integral time scale.

The individual estimates of the various quantities are now presented. Table 5.1 shows a comparison of array-averaged estimates of the various statistics of the region at nominal depths of 500 m and 4000 m. The quantities estimated from current meter measurements are the average of five instruments at each depth (current meter moorings 9, 10, 11, 12 and 13, located in the vicinity of the tomographic array). Standard procedures were used to calculate the energy and eddy fluxes. For the tomographic estimates, the estimates of the quantities taken from the layers 500–750 m and 3000–4000 m have been used. Mean and eddy kinetic energies are estimated using leg 3↔4 for the u -velocity and leg 2↔5 for the v -velocity. The temperature variance represents the average of all six sections calculated for the tomographic array. The momentum flux is estimated using the u -velocity from leg 3↔4, and the v -velocity from leg 3↔4. The heat fluxes have been calculated using two separate legs of the tomographic array. The zonal heat flux is estimated using u and t values from leg 3↔4. The meridional heat flux is estimated using v and t estimates from leg 2↔5. Mean and perturbation vorticity estimates are for the area bounded by moorings 2, 3, 4 and 5.

Estimates from tomographic and current meter measurements of mean and eddy variances, along with flux estimates, compare favorably. The variance estimates from the current meter measurements exceed those of the tomographic measurement, most likely due to the spatially-integrating nature of the tomographic measurement. The higher variance levels for the current meter measurement were noted in the previous chapter.

Table 5.1: Statistical Comparison

Measurements at 500 m

Measurement	$\frac{\bar{u}^2 + \bar{v}^2}{2}$ (cm ² /s ²)	$\frac{u'^2 + v'^2}{2}$ (cm ² /s ²)	$\overline{T'^2}$ (°C) ²	$\overline{u'v'}$ (cm ² /s ²)	$\overline{u'T'}$ (°C cm/s)	$\overline{v'T'}$ (°C cm/s)	$\bar{\zeta}$ 10 ⁻⁶ s ⁻¹	$\bar{\zeta}^2$ 10 ⁻¹² s ⁻²
Tomography	12.3 ± 26.1	225.4 ± 123.4	1.1 ± 2.7	5.0 ± 76.1	-2.3 ± 4.5	-4.6 ± 6.2	-2.1 ± 4.3	0.25 ± 1.2
Current Meter	33.1 ± 17.8	382.4 ± 54.9	2.5 ± 1.7	-12.6 ± 54.6	-3.3 ± 4.7	-6.3 ± 5.0	-2.1 ± 3.9	—

Measurements at 4000 m

Measurement	$\frac{\bar{u}^2 + \bar{v}^2}{2}$ (cm ² /s ²)	$\frac{u'^2 + v'^2}{2}$ (cm ² /s ²)	$\overline{T'^2}$ 10 ⁻⁴ (°C) ²	$\overline{u'v'}$ (cm ² /s ²)	$\overline{u'T'}$ 10 ⁻² (°C cm/s)	$\overline{v'T'}$ 10 ⁻² (°C cm/s)	$\bar{\zeta}$ 10 ⁻⁶ s ⁻¹	$\bar{\zeta}^2$ 10 ⁻¹² s ⁻²
Tomography	6.7 ± 15.9	42.1 ± 38.7	4.1 ± 3.9	9.8 ± 17.2	-0.2 ± 4.8	-2.1 ± 5.2	-0.8 ± 1.7	5.8 ± 7.2
Current Meter	9.5 ± 7.6	65.8 ± 23.6	6.3 ± 1.9	15.3 ± 14.1	1.3 ± 3.6	-2.7 ± 3.8	0.7 ± 000	—

The mean kinetic energy levels for the tomographic estimate are very low throughout the water column, suggesting near-zero mean flow in the background region. Eddy kinetic energy levels are quite high, and dominate the mean field from top-to-bottom. The estimated kinetic energies show a fairly monotonic decrease with depth. The temperature variance is a maximum in the thermocline region, with the variability most likely dominated by the vertical translation of the large-scale vertical gradient of temperature. The meridional heat flux dominates the zonal heat flux throughout the water column, and is directed southward at all levels. The zonal heat flux is directed westward in all the layers except at 1000–1800 m depth. The momentum flux is positive for all layers except the upper two layers, where it is small and negative. The perturbation relative vorticity is larger than the mean, with typical values a full order of magnitude larger than the mean estimate. The perturbation relative vorticity is surface-intensified and decreases monotonically with depth.

Mean and eddy kinetic energies estimated from both measurements compare quite favorably, as do the estimates of the temperature variances and heat fluxes. The momentum fluxes compare at 4000 m, but not at 500 m. The similarity of the relative vorticity at 500 m is primarily due to the near-zero mean value of the relative vorticity.

We now focus on a description of the region based on the tomographic estimate of the terms in Table 5.1. Inverse estimates of the various quantities were calculated at depths ranging from the surface to a depth of 4000 m. The mean and eddy kinetic energies are considered first. Throughout the water column the eddy kinetic energy dominates the mean kinetic energies. The temperature variances peak in the thermocline, with the value given at 500 m the maximum throughout

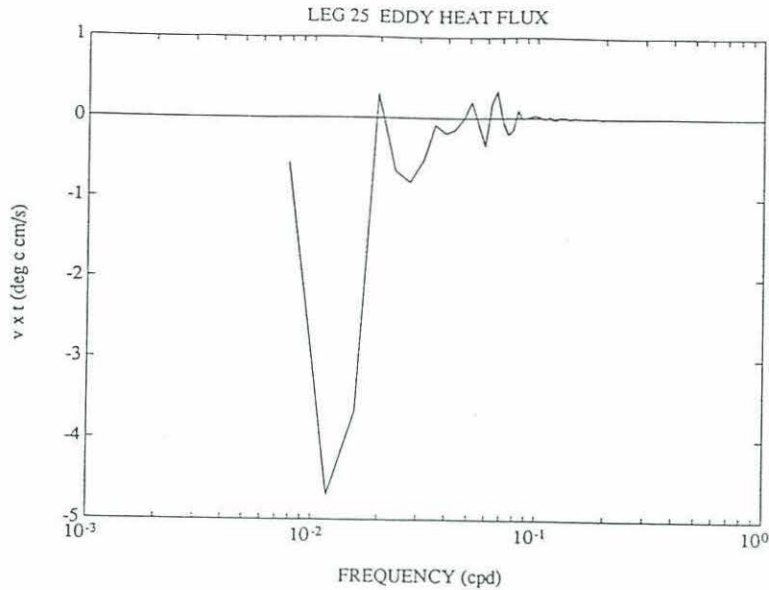


Figure 5.1: Meridional heat-flux spectrum at 1000 m depth in variance-preserving form.

the water column. The momentum flux is predominantly positive, with small negative values at the two surface layers. The meridional heat flux is much larger than the zonal heat flux throughout the water column, and is directed southward at all levels. The zonal heat flux is directed primarily westward, with the exception of the layers between 1000–1800 m. The perturbation relative vorticity is in excess of the mean value, with typical values a full order of magnitude larger than the mean estimate. The perturbation vorticity variance is surface-intensified, and decreases fairly monotonically with depth.

The co-spectrum of v and T provides an estimate of meridional heat flux, and is presented in Figure 5.1. The co-spectrum of v and T shows a large southward flux of heat associated with wave motions of 50–120 d periodicities. Spectral estimates of other co-spectral estimates, such as zonal heat flux and momentum flux, can be characterized in the same fashion at various depths. The estimation of these fluxes will be used later to address the wave-mean flow interaction of the eddy field with the large-scale circulation.

5.3 The Vorticity Equation

In order to address the dynamics of low-frequency fluctuations and their relation to the general circulation, we must consider the potential vorticity. The local effects of the mesoscale eddy field on the mean potential vorticity distribution is determined from the quasi-geostrophic eddy potential vorticity flux. The divergence of this flux acts as a driving mechanism in forcing flow across geostrophic contours. Even though we are unable to calculate many of the terms in the potential vorticity balance, as will be discussed below, the formalism is important to illustrate what we can measure, and what we should strive to measure in future endeavors.

The quasi-geostrophic potential vorticity equation for a continuously stratified inviscid fluid, in the absence of sources or sinks [see *e.g.*, Pedlosky (1979) or Brown *et al.*, (1986)] is given by

$$\left[\frac{\partial}{\partial t} + u \frac{\partial}{\partial x} + v \frac{\partial}{\partial y} \right] \left[\zeta + f + f_0 \frac{\partial}{\partial z} \left(\frac{\rho}{\bar{\rho}_z} \right) \right] = 0, \quad (5.1)$$

where \mathbf{u} is the horizontal velocity (u, v) , ρ is the perturbation density, $\bar{\rho}$ is the reference state density, $f = f_0 + \beta y$ is the Coriolis parameter, $\zeta = dv/dx - du/dy$ is the vertical component of relative vorticity and $q = \zeta + f + f_0 \partial/\partial z (\rho/\bar{\rho}_z)$ is the potential vorticity. This equation incorporates the heat equation into the vorticity equation.

The mean potential vorticity balance is derived by separating time-mean and time-dependent components, and averaging. The result is

$$\bar{\mathbf{u}} \cdot \nabla \bar{q} = -\nabla \cdot \overline{\mathbf{u}'q'}, \quad (5.2)$$

with the mean potential vorticity defined by

$$\bar{q} = \beta y + \overline{v_x} - \overline{u_y} + f_0 \overline{\frac{\partial}{\partial z} \frac{\rho}{\rho_z}}. \quad (5.3)$$

The first term is the planetary vorticity, the second term relative vorticity, and the third vortex stretching. The advection of the mean potential vorticity by the mean circulation is balanced by the horizontal divergence of the eddy potential vorticity. The eddy potential vorticity flux vector is given by

$$\overline{\mathbf{u}'q'} = \overline{\mathbf{u}'(v'_x - u'_y)} + f_0 \overline{\mathbf{u}' \frac{\partial}{\partial z} \frac{\rho}{\rho_z}}. \quad (5.4)$$

The eddy potential vorticity flux is composed of two terms. The first term is the relative vorticity flux. The second term is the eddy thickness flux.

The eddy relative vorticity flux may be written in terms of velocity variances.

The components of the eddy relative vorticity flux are

$$\begin{aligned} \overline{u'\zeta'} &= \frac{\partial}{\partial x} \overline{u'v'} + \frac{\partial}{\partial y} \frac{\overline{v'^2 - u'^2}}{2} \\ \overline{v'\zeta'} &= -\frac{\partial}{\partial y} \overline{u'v'} + \frac{\partial}{\partial x} \frac{\overline{v'^2 - u'^2}}{2}. \end{aligned} \quad (5.5)$$

The components of the eddy thickness flux are

$$\begin{aligned} \overline{u'\eta'} &= f_0 \overline{u' \frac{\partial}{\partial z} \frac{\rho}{\rho_z}} \\ \overline{v'\eta'} &= f_0 \overline{v' \frac{\partial}{\partial z} \frac{\rho}{\rho_z}}. \end{aligned} \quad (5.6)$$

Under the assumption of a tight $T - S$ relationship, the densities may be written in terms of temperatures.

To fully understand the effect the eddies have on the mean flows, all of the terms in the eddy potential vorticity flux need to be evaluated. Note that it is the divergence of the eddy potential vorticity flux which allows the low-frequency fluctuations to have an influence on the large-scale circulation. However, the direction of the eddy vorticity fluxes relative to the mean large-scale potential vorticity gradient indicate whether the eddies enhance or reduce the mean potential vorticity distribution.

The velocity variances can be readily estimated with the tomographic measurements, but the horizontal gradients are more difficult to measure. Even more troublesome is the inability to calculate the divergence. The thickness flux, which is roughly proportional to the heat flux, can be estimated from the tomographic measurements, albeit with large uncertainty for the present experiment. To better attack the problem, a longer data record is needed, as well as better horizontal resolution from the tomographic array. This issue will be considered further in the discussion section.

As we are not able to estimate all of the terms in the vorticity equation, we adopt a procedure which will allow us to obtain some dynamical information regarding the relation of the eddies to the mean circulation. This will be accomplished with the calculation of the Eliassen-Palm flux vectors. Under relatively mild assumptions, it will be shown that a source of eddy energy external to the experimental region can be inferred from the second-order statistics.

5.4 Eliassen–Palm Flux Calculation

Tomographic estimates of second-order statistics are used to diagnose properties of eddy–mean flow interactions. Consideration of the eddy heat and momentum fluxes within the context of the Eliassen–Palm flux formalism provides a useful procedure for investigating the effect of eddy motions on the large-scale circulation (see *e.g.*, Eliassen and Palm, 1961 and Pedlosky, 1979). The Eliassen–Palm flux formulation has been used in the analysis of the propagation of wave activity and of the interaction between waves and mean flows. The utility of the Eliassen–Palm flux framework is in the direct linking of eddy transport properties with propagation characteristics. The original formulation was restricted to wave interactions on zonally-averaged flow. More recently the concept has been generalized to three dimensions by Plumb (1986). The formulation given below follows Plumb’s analysis.

The generalized theory is valid for small-amplitude transient eddies on a slowly-varying mean flow. The result leads to the definition of a flux \mathbf{M}_T which is a conserved measure of the flux of eddy activity. This flux is parallel to the group velocity for an almost-plane wave train. The total wave activity flux \mathbf{M}_T is given by

$$\mathbf{M}_T = \mathbf{M}_R + \bar{\mathbf{u}} M, \quad (5.7)$$

where \mathbf{M}_R is the radiative activity flux and $\bar{\mathbf{u}} M$ is the wave activity flux due to advection by the mean flow. The positive definite quantity M is given by

$$M \propto \frac{e}{|\nabla_H \bar{q}|},$$

where $e = \frac{1}{2} \bar{q}^2$ is the eddy potential enstrophy and $|\nabla_H \bar{q}|$ is the modulus of the mean potential vorticity horizontal gradient. In the almost-plane wave limit

$$\mathbf{M}_T = \mathbf{c}_g M, \quad (5.8)$$

where \mathbf{c}_g is the group velocity of the transient waves. Under the assumption that the mean potential vorticity gradient is slowly varying, this wave activity flux can be used as a diagnostic of transient eddy propagation to infer sources and sinks of wave activity. In the quasi-geostrophic limit, the energy flux vector is equal to the wave energy multiplied by the group velocity (Pedlosky, 1979). As the group velocity is parallel to energy flux vector, the wave activity flux is thus parallel to the energy flux.

Several assumptions have been made prior to reaching this conclusion. The mean potential vorticity gradient is assumed to be meridional. This is valid since the potential vorticity is dominated by the planetary vorticity for the region of interest. In a depth-averaged sense, the local planetary vorticity is one to two orders of magnitude larger than the average relative vorticity and one order of magnitude larger than the average vortex-stretching vorticity. At thermocline levels, the vortex stretching is of comparable magnitude to the planetary vorticity. However, McDowell *et al.*, (1982) find that the contours of vortex stretching are mostly parallel to the planetary vorticity contours throughout the region. The basic assumption for Plumb's approximation to hold is that the total vorticity contours be mostly zonal. This assumption is therefore rather good in our region. The relative vorticity is smaller than the planetary vorticity throughout the water column. In the experimental region the mean velocity $\bar{\mathbf{u}}$ is negligible compared to the eddy-component

of the velocity, so $\mathbf{M}_T \approx \mathbf{M}_R$, *i.e.*, the total wave activity flux is approximately equal to the radiative component of the wave activity flux. In the coordinate system where the y -component of the flux is in the direction of the potential vorticity gradient, *i.e.*, the actual north in our case as $\nabla_H \bar{q} = \nabla_H \bar{f}$, the wave activity flux has components

$$\mathbf{M}_R = \left(\overline{v'^2} - \epsilon, -\overline{u'v'}, \frac{f \overline{v'\theta'}}{d\bar{\theta}/dz} \right) \quad (5.9)$$

in the quasi-geostrophic approximation, where $\epsilon = \frac{1}{2} [\overline{u'^2} + \overline{v'^2} + \frac{\overline{N^2} \overline{\theta'^2}}{(d\bar{\theta}/dz)^2}]$ is the eddy kinetic plus potential energy, $\bar{\theta}(z)$ is the background temperature profile, and $\overline{N^2}(z)$ is the background Brunt–Väisälä frequency profile.

The wave activity flux has been evaluated using estimates of the various statistics from the tomographic measurements. Zonal and meridional velocity variances are nearly the same, and an order of magnitude larger than the potential energy term in ϵ . As a result, the zonal component of the wave activity flux is an order of magnitude smaller than the meridional and vertical components. The momentum flux is predominantly positive and order $10 \text{ cm}^2/\text{s}^2$ throughout the water column. This leads to a negative estimate for the meridional component of the wave activity flux. The heat flux is always negative, with a maximum magnitude of -4.8°C cm/s at 600 m depth. This leads to a negative estimate for the vertical component of the wave activity flux. The interpretation is that the wave activity flux is directed predominantly southward and downward, as is to be expected for Rossby wave energy propagation. A schematic of the wave radiation process is presented in Figure 5.2. Three planar sections have been extracted from the fluid cube in which the array is imbedded. The wave activity flux is directed southward in the plan views at 500 m and 1000 m, and downward in a vertical section through

ELIASSEN – PALM FLUX VECTOR

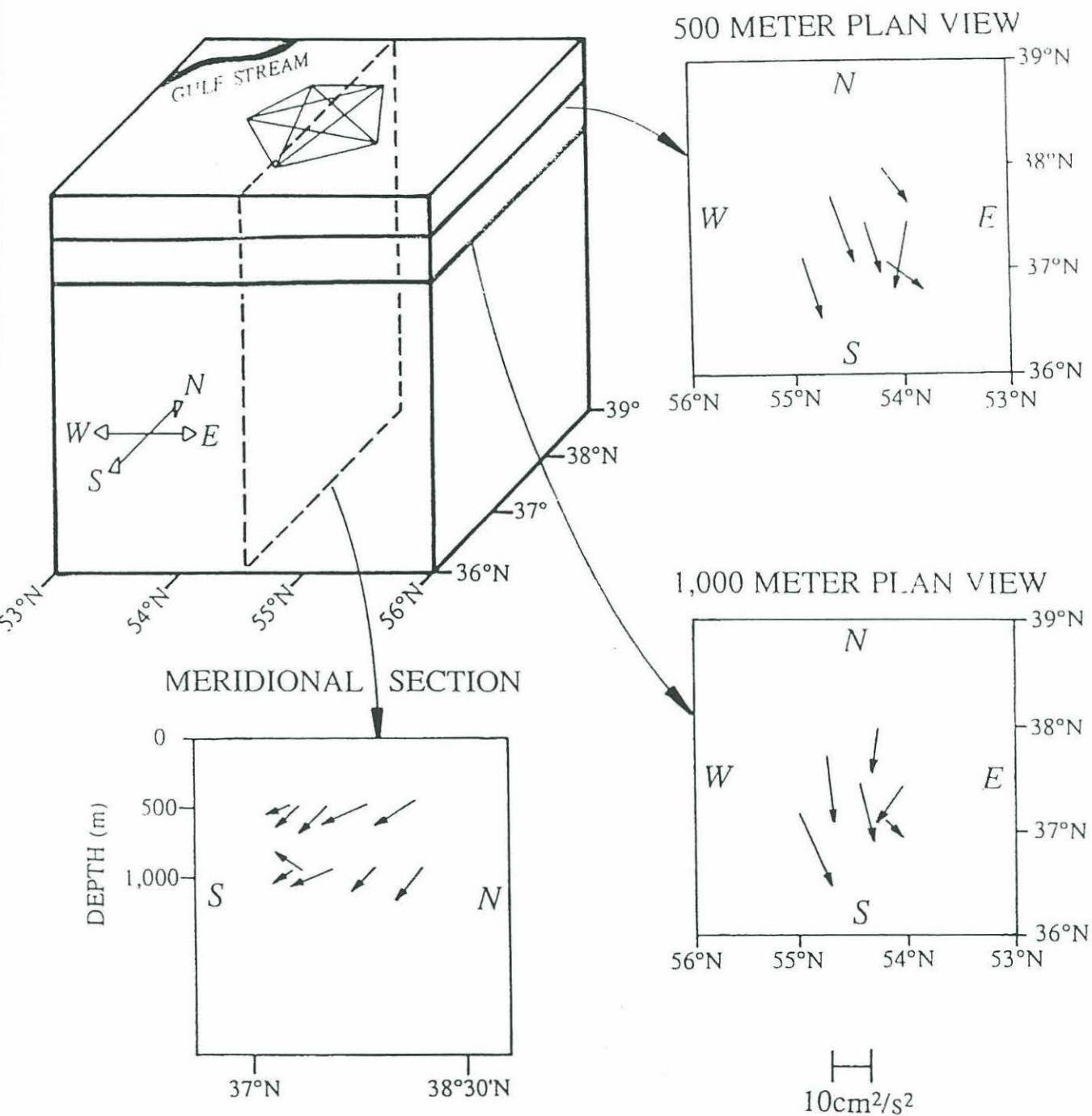


Figure 5.2: Eliassen-Palm flux vectors.

55°W. The source of the wave activity flux as diagnosed from the flux vector \mathbf{M}_R is located somewhere to the north of the tomographic array, in the region of the Gulf Stream jet path. This diagnosis provides a strong foundation to the hypothesis that the Gulf Stream itself is the source of wave energy radiating into the far field and found in the interior of the Northwestern Atlantic, even though caution must be used in view of the large errors in the flux estimates. However, a different interpretation may be possible, that being the presence of local baroclinic instability, and is discussed in the final section.

5.5 Discussion

The statistics of the region have been estimated from the spatially-averaged tomographic measurements. This presents a unique view of the region with better vertical resolution than has been previously attained. The statistics of many of the tomographic estimates compare well with measurements from current meter measurements. Part of this correlation is attributed to the large-scale nature of the motions which dominate the fluctuation fields, coupled with the short ranges separating the tomographic instruments. Discrepancies do exist, particularly in the estimated momentum fluxes. The comparison of the two measurements is also not expected to be identical. Two different measurements are being compared. One of the advantages of the tomographic measurement is the inherent spatial integration. Tomographic estimates of energies and fluxes are representative of areal averages, with small-scale motions being filtered out.

It is important to note that the Gulf Stream tomographic array is in proximity to the near-field region of the Gulf Stream. The near-field region is typically

considered to be several Rossby radii from the jet (order 100 km). The southern portion of the array is located roughly 300 km south of the mean axis of the jet, and may possibly be considered to be in the far field. The importance of this distinction is that wave motions generated by the Gulf Stream and radiated southward may not leave a conclusive signature in the near field. However, after having had more time to disperse, the wave train may have a more detectable fingerprint in the far-field region. In regions very far away from the source, dissipation becomes an important factor.

The nearness of the Gulf Stream jet to the tomographic array leads to difficulty in the interpretation of the various momenta fluxes and the corresponding propagation of energy. The tomographic array is situated in a transitional region, and the signal of wave radiation from the Stream itself and local baroclinic instabilities of the underlying westward return flow are probably both present in this area. The pycnocline slopes to the north in the Gulf Stream frontal region, consistent with geostrophy. Baroclinic instability in this region would be accompanied by motions with an downward group velocity. In the recirculation region there is a gentle slope of the pycnocline upward to the south. Upward group velocities are expected for Rossby waves in this region.

A complete dynamical investigation of the interaction of the eddy field with the large-scale circulation could not be obtained in this experiment. We were unable to estimate the divergence of the eddy fluxes, which can act to drive mean circulations. However, through the Eliassen–Palm flux diagnosis, we are able to infer a source for the energetic eddy variability in the region, albeit with large error bars. The Eliassen–Palm flux diagnosis is used as a tool to infer remote sources and sinks of wave action in the region. However, local instability processes, such

as baroclinic instability of the underlying mean flow, may also be prevalent in the region. An analysis of Polymode array current meter data by Hogg (1985) suggested that the westward return flow is baroclinically unstable. The signature of this process is a downgradient heat flux, and upward group velocities. The 300-day mean zonal velocities for the SYNOP experiment had near-zero velocities. However, mean zonal velocities estimated from two years of current meter measurements showed a mean westward velocity of 5 cm/s in the region. Both wave radiation from the Gulf Stream and local baroclinic instability are therefore most likely to be the important sources of eddy energy in this portion of the subtropical gyre.

Numerical models suggest that that one must make integral measurements of the fluxes to fully attack the wave-mean flow interaction problem. The interpretation of the observational results from point measurements is much more limited than for the numerical models because the divergence of the eddy flux cannot be calculated to sufficient accuracy. To this end, tomography is ideally suited to make these integral measurements. The inability of the SYNOP tomographic system to measure the divergence of the heat, momentum or vorticity flux was unfortunate. However, the goals of the tomographic experiment at the outset did not include such an analysis. This precludes us from saying anything definitive about the effect of the eddy field on the large-scale circulation. Nevertheless, we can comment on the structure of the low-frequency motions in the region, and through the Eliassen-Palm flux calculation can implicate the Gulf Stream as the source for the predominance of the mesoscale variability. The utility of the tomographic measurement is in the inherent spatial averaging and in the enhanced vertical resolution which arises from the acoustic sampling characteristics. Observations of the depth dependence of the momentum fluxes is an important result. The coefficient of eddy viscosity is directly

related to this term, and depth dependent measurements of these fluxes might be used to parameterize eddy coefficients in ocean general circulation models.

The SYNOP Gulf Stream tomography array was not specifically designed to look at second-order statistics. However, the importance of estimating these quantities has already been noted. An estimate of the divergence of the momentum flux, for example, would prove quite valuable in addressing the dynamical link between the eddy field and the large-scale circulation. For a larger tomographic array, with more transceivers, the horizontal resolution would be greatly improved as the number of crossing paths increases geometrically with each additional transceiver. This would lead to the ability to better resolve range-dependent structures. Divergences could then be readily calculated from horizontally-mapped fields. A feasible array geometry is a tradeoff between the compactness needed to obtain mesoscale resolution and the large area coverage necessary to measure large-scale circulations. The required resolution is a function of both the eddy length scales and the homogeneity of the momentum fluxes. A long time series of at least two years in duration would also be necessary to obtain statistical reliability for the estimates. It is however not clear at this stage how one would best design a tomographic configuration to attack this very problem, and such an array design is beyond the scope of this thesis.

Chapter 6. Summary and Discussion

The primary goal of this thesis has been to investigate the structure, energetics, dynamics and variability of the northern extent of the southern recirculation gyre at 55°W . The investigation has been conducted through the analysis of data obtained from an array of tomographic transceivers. The region of interest, centered at 38°N and 55°W is one of extremely energetic mesoscale variability. The proximity of the Gulf Stream, which was typically located 100 km to the north of the tomographic array, positions the array in the near-field region of the Stream. The local meandering of the Gulf Stream and the presence of cold core rings in the region both have a dramatic influence on the variability fields. This region is one of active interaction between the eddy field and the large-scale circulation.

Tomographic estimates of temperature, current velocity and relative vorticity have been estimated for 100–200 km sections over a 300-day period. The tomographic measurement provides a unique view of the region. The measurement provides an intriguing look at range-averaged properties of the temperature and along-path current velocity fields, and areal-averaged properties of the relative vorticity field. The structure and variability of the region has been sampled with better vertical resolution than has previously been attained. Typical resolution in the surface in the upper 1000 m of the ocean is of the order of 100–200 m. At depths greater than 1000 m, the resolution deteriorates to order 500 m. The enhanced vertical resolution is attributed to the sampling of the water column by several ray paths (typically two to five). Most of the energetic events have been shown to be coherent with depth.

Estimates of temperature, current velocity and relative vorticity have all been shown to be quite energetic. The variability is dominated by scales of motion ranging from roughly 20 d to 100 d. This preponderance of low-frequency energy is clearly manifest in the spectral properties of the estimates. Spectra calculated at various levels in the vertical (from the surface to 4000 m) all exhibit the typical red nature of the spectrum, which is characteristic for motions in this region. The importance of adequately describing the variability field in the region cannot be over-emphasized as this field is directly coupled to the Gulf Stream. In other words, any attempt to predict the evolution of the Gulf Stream requires a realistic characterization of the near-field region.

Cold core rings are present in the region for a substantial portion of the 300-day data record, and their signature is clearly present in temperature and vorticity estimates. The direct estimate of relative vorticity over regions of roughly 10,000 square kilometers is one of the most interesting results of the thesis. Estimated relative vorticity can prove unambiguously the presence and/or passage of cyclonic, cold-core rings that may not be detectable with other measurements, especially if the infrared imagery is not available or the ring has shed its surface signature. This direct measurement of vorticity also has errors much smaller than those obtained from previous measurements. Most earlier attempts at estimating relative vorticity have required the differentiation of the field with point measurements typically of the order of 100 km apart. The errors in a calculation of that type are quite large, owing in large part to the finite differencing of the measurements. Estimated relative vorticities throughout the experiment typically were an order of magnitude smaller than the planetary vorticity.

Comparison of the tomographic measurement with concurrent data, primarily current meter data, and numerical model values, also points out some interesting results. The spatially-integrating tomographic measurement has similar energy levels to the other field estimates for motions with periodicities greater than 20 d. These low-frequency events usually are dominated by motions with larger spatial scales. The correlation length scales for temperature and velocity in this region are typically estimated at 100 to 150 km, so the utility of tomography in averaging over many individual events has not been fully demonstrated in this experiment due to the short propagation ranges (100 to 200 km) for the Gulf Stream tomography experiment. However the tomographic measurement does average over many of the higher frequency motion events, which typically have smaller spatial scales of motion. This is clearly demonstrated in the various spectral comparisons.

The tomographic results presented in this thesis also show that errors in the tomographic estimates are comparable to the errors inherent in more conventional instrumentation. Daily-averaged estimates of range-averaged temperature, along-path current velocity, and areal averaged relative vorticity are estimated to a precision of 0.01°C , 3 cm/s , and $2 \times 10^{-6}\text{ s}^{-1}$, respectively.

Spatially-averaged measurements of heat and momentum fluxes have also been estimated with the tomographic data set. The integrating nature of the tomographic measurement has been exploited to sample the large-scale properties of the second-order statistical quantities in this energetic region. The eddy kinetic energy has been shown to be much larger than the mean kinetic energy throughout the water column.

Both heat and momentum flux estimates for the region are dominated by variability in the band of frequencies centered at 64 d. A spatially-averaged heat flux estimate for the region indicates a southward component throughout the water column. This is counter to the mean gradient of temperature, hence indicative of the local presence of baroclinic instability of the background flow. An estimate of the spatially-averaged momentum flux indicates a generally positive value through the water column. Due to a short data record (300 d), the sampling error leads to values which are not statistically significant at the 95% level, so care must be taken when considering results deriving from these estimates. By adopting the Eliassen–Palm flux diagnostic, an energy source to the north of the array has been hypothesized from the orientation of the fluxes in relation to the large-scale background field. The implication is that the Gulf Stream itself is the source for the eddy radiation field in the this region and responsible for the wave radiation in the interior of the North Atlantic subtropical gyre. It is the divergence of the eddy momentum and heat flux which is dynamically and thermodynamically important. Unfortunately, we are not able to estimate this quantity from the tomographic array. This precludes us from making any statements regarding the effect of the eddy field on the mean circulation. The direct link between the Gulf Stream and the mesoscale eddy field in the region cannot be deduced owing to the inability to estimate the divergence of the momentum flux. Nevertheless, the implication of the Gulf Stream as the source of energy for the far-field is an important conclusion.

A few technical details concerning the tomographic measurement are now considered. The transceiver positioning was not monitored throughout the experiment. Mooring motion leads to a large signal in the acoustic multipath travel time measurements and, if not accounted for, could lead to spurious inverse-estimated

temperature anomalies. Two solutions are available to deal with this indeterminacy. The first is to include the mooring position as an unknown in the inversion procedure. The second is to estimate the position of the mooring through the use of a mooring motion model. The second procedure was adopted in this study. Only a few (one to seven) identifiable and resolved acoustic multipaths existed for each source/receiver pair. The inclusion of the mooring positioning as an unknown in the inverse procedure essentially uses one of the precious pieces of information in the data to estimate the absolute range between the source and the receiver. The choice was made to not compromise the vertical resolution that was attainable from the limited data.

A few remarks concerning suggestions for future experimental endeavors are also made. The short separation ranges (100–200 km) for the Gulf Stream tomography experiment leads to a lack of dispersion of the acoustic multipaths, and thus the inability to separate individual arrivals. Transmission between the legs separated by greater ranges, such as leg 2↔5 (with a range of 200 km) leads to many more resolvable multipaths. This should be considered in the future. The signal level is adequate to extend these instruments to further ranges, thus increasing the vertical resolution achievable. Also, an array of hydrophones would allow for the resolution of simultaneously-arriving up and down rays, hence adding more information to the identification of arrivals.

Appendix A: Ambient Noise

In addition to receiving the transmitted signals, the tomographic transceiver systems are scheduled to make an ambient noise measurement just prior to each signal reception. The hydrophone samples the ambient field for several seconds, and the system adjusts the variable gain setting to maintain an output signal level of about 1.25 volts. This level corresponds to a value which is one quarter of full scale. The system is tuned at this level to prevent saturation of the receiver while sampling the signal. The digitizer used in the receivers consists of 12 bits (11 bits plus sign), so a signal level of 1.25 volts corresponds to 512 in digitizer units. The variable gain setting, as well as the current and previous input to the digitizer, are recorded on tape as part of the engineering measurements. Using these values, and the system calibration constants determined prior to deployment, ambient noise can be estimated.

The procedure is illustrated in Figure A.1. From the system calibration, the hydrophone sensitivity is -202 dB re $1 \mu\text{Pa}$. This means that 202 dB is required to create $1 \mu\text{Pa}$ of pressure at the phone. The fixed system gain, which includes amplification of the signal and filter gain, is $65 \text{ dB} + 24 \text{ dB}$, or 89 dB. The variable gain is set at increments of 1.5 dB per step (0 to 40 steps, but not allowed to surpass a variable gain setting of 33).

Daily estimates of the ambient noise at mooring 2 ($38^{\circ}35'\text{N}$, $54^{\circ}02'\text{W}$), at a depth of 1175 m, are given in Figure A.2. The calculated noise has a mean of 70.6 dB, with a standard deviation of 2.2 dB. Expected ambient noises in this region are roughly 70 to 75 dB at 400 Hz (see Urick, 1983), the primary source of noise being surface winds. The periods of high ambient noise correspond to periods

Ambient Noise Calculation

Consider the following example, where the variable gain is 15 (steps), and the value of the rms level at the input to the digitizer is 512 (in digitizer units). These values can be obtained from the engineering measurements recorded on tape for each reception.

The ambient noise at the hydrophone is found as follows:

First, the rms signal level at the input to the digitizer is converted to dB.

$$\begin{aligned}
 \text{Input Level} &= 512/2047 \times 5 \text{ volts} && [2047 = 2^{11} - 1, \text{ and multiply} \\
 & && \text{by 5 volts, which is full scale}] \\
 &= 1.25 \text{ volts} \\
 &= 1.94 \text{ dB} && [\text{power is proportional to volts}^2, \\
 & && \text{so multiply by } 20 \log_{10} (n \text{ volts}) \\
 & && \text{to convert volts to power}]
 \end{aligned}$$

This is the output of the digitizer. What we want is the input ambient noise field at the hydrophone itself. Thus, all of the system gains used to get to this stage must be subtracted out.

$$\begin{aligned}
 &+ 1.94 \text{ dB} && [\text{output of digitizer}] \\
 &- 65 \text{ dB} && [\text{fixed system gain (preamp)}] \\
 &- 24 \text{ dB} && [\text{fixed system gain (gain of band-} \\
 & && \text{pass filter in 1-Hz band)}] \\
 &- 22.5 \text{ dB} && [\text{variable gain (15} \times \text{1.5 dB/step)}] \\
 &- - - - - \\
 &= -109.6 \text{ dB}
 \end{aligned}$$

Ambient noise measurements are referenced to a 1 Hz band, so we must subtract out the gain using a 100 Hz band.

$$\begin{aligned}
 &-109.6 \text{ dB} \\
 &- 20 \text{ dB} && [\text{bandpass filter } (-10 \log_{10} 100 \text{ Hz})] \\
 &- - - - - \\
 &-129.6 \text{ dB} && \text{re 1 V in a 1 Hz band} \\
 &- -202 \text{ dB} && \text{re 1 V [hydrophone sensitivity]} \\
 &- - - - - \\
 &72.4 \text{ dB} && \text{re 1 } \mu\text{Pa in 1 Hz at 400 Hz}
 \end{aligned}$$

Figure A.1: Ambient noise calculation.

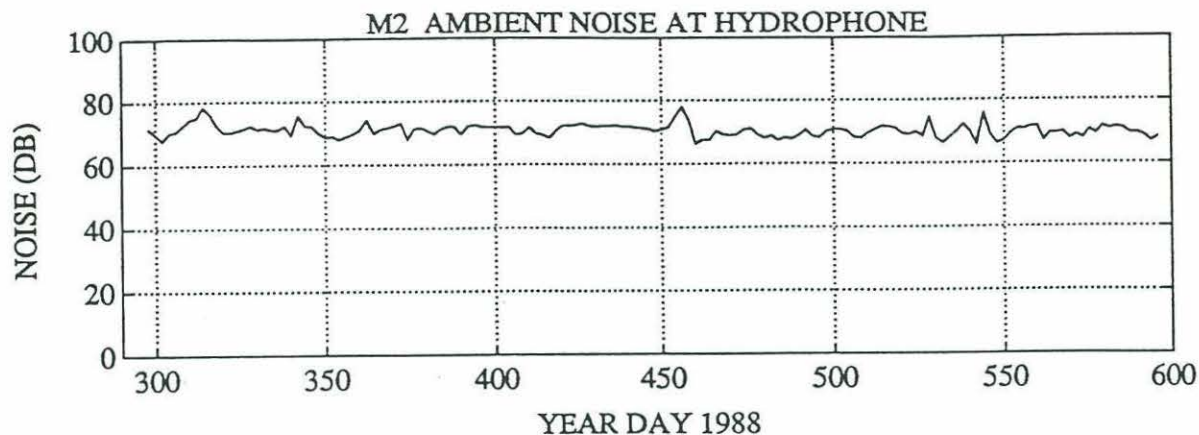


Figure A.2: Ambient noise level at mooring 2 ($38^{\circ}35'N$, $54^{\circ}02'W$), at a depth of 1175 m.

of energetic mesoscale activity, as evidenced by local current measurements and vertical excursions of the mooring. This leads one to suspect that ambient noise fluctuations can, in some instances, be used to infer the passage of mesoscale events

Ambient noise values, used in conjunction with the pulse response records, can be utilized to give the exact signal levels of the arrivals. This cannot be done solely with pulse response intensities. In forming complex demodulate pairs, we have sacrificed some information by compressing the original 16 samples per digit to four samples per digit. Nevertheless, we can equate the calculated ambient noise level with a suitably averaged 'quiet' portion of the pulse response record. Combining this information with the signal-to-noise ratio (SNR) of individual pulses, obtained solely from the pulse response records, the absolute signal levels can be surmised. For example, the ambient noise, as determined from the engineering measurements, is some value, say 70 dB. From the pulse response, we find that a typical noise level estimate is 10^{12} (this value derives from the correlation of the complex demodulates). The intensity of a peak arrival in the forementioned record is typically 10^{14} , or 20 dB

$(10 \log_{10} 10^{14} / 10^{12})$ above the background noise level. Hence, the absolute signal is 70 dB (ambient) + 20 dB (SNR) = 90 dB. The utility of such an estimate may not be all that important, but it worth showing how to arrive at it, and comparing with propagation loss estimates.

References

- Applied Tomography Experiment Group, The (1991) Applied tomography experiment of 1990. Technical Report, APL-UW TR9106, 120 pp.
- Berteaux, H. O. (1976) *Buoy Engineering*. John Wiley and Sons, New York, 314 pp.
- Boutin, P. B., J. Kemp, S. Liberatore, J. Lynch, N. Witzell, K. Metzger and D. Webb (1989) Results of the Lake Seneca directivity, source level, and pulse response tests of the MIT 400 Hz Webb tomography sources. Woods Hole Oceanographic Institution Technical Memorandum WHOI-1-89.
- Bower, A. and N. Hogg (1991) Correlation functions for objective mapping at 55°W. *The Synoptician*, 2(3), 4–6.
- Bower, A. S. and N. G. Hogg (1992) Evidence for barotropic wave radiation from the Gulf Stream. *Journal of Physical Oceanography*, 22, 42–61.
- Brown, E., W. B. Owens and H. L. Bryden (1986) Eddy-potential vorticity fluxes in the Gulf Stream recirculation. *Journal of Physical Oceanography*, 16, 523–531.
- Brown, M. G. (1884) Linearized travel time, intensity, and waveform inversions in the ocean sound channel — a comparison. *Journal of the Acoustical Society of America*, 75, 1451–1461.
- Bryden, H. L. (1982) Sources of eddy energy in the Gulf Stream recirculation region. *Journal of Marine Research*, 40, 1047–1068.
- Capotondi, A. (1993) Assimilation of altimeter data in a quasi-geostrophic model of the Gulf Stream System: A dynamical perspective. Ph.D. Thesis, Ph.D. Thesis, Massachusetts Institute of Technology/Woods Hole Oceanographic Institution.
- Chester, D. B., P. Malanotte-Rizzoli and H. DeFerrari (1991) Acoustic tomography in the Straits of Florida. *Journal of Geophysical Research*, 96, 7023–7048.
- Cornuelle, B. (1983) Inverse methods and results from the 1981 ocean acoustic tomography experiment. Ph.D. Thesis, Massachusetts Institute of Technology/Woods Hole Oceanographic Institution, 359 pp.
- Cornuelle, B. D. (1985) Simulations of acoustic tomography array performance with untracked or drifting sources and receivers. *Journal of Geophysical Research*, 90, 9079–9088.

- Dantzler Jr., H. L. (1977) Potential energy maxima in the tropical and subtropical North Atlantic. *Journal of Physical Oceanography*, **7**, 512–518.
- Del Grosso, V. A. (1974) New equation for the speed of sound in natural waters (with comparisons to other equations). *Journal of the Acoustical Society of America*, **56**, 1084–1091.
- Eliassen, A. and E. Palm (1961) On the transfer of energy in stationary mountain waves. *Geofysiske Publikasjoner*, **22**, 1–23.
- Fisher, A. Jr. (1977) Historical limits of the northern edge of the Gulf Stream. *Gulfstream*, **3**, 6–7.
- Flatté, S. M., R. Dashen, W. Munk, K. Watson and F. Zachariasen (1979) *Sound Transmission through a Fluctuating Ocean*. Cambridge University Press, New York, 299 pp.
- Flatté, S. M. and R. B. Stoughton (1986) Theory of acoustic measurement of acoustic wave strength as a function of depth, horizontal position, and time. *Journal of Geophysical Research*, **91**, 7709–7720.
- Flierl, G. R. and A. R. Robinson (1984) On the time-dependent meandering of a thin jet. *Journal of Physical Oceanography*, **14**, 412–423.
- Gaillard, F. (1985) Ocean acoustic tomography with moving sources or receivers. *Journal of Geophysical Research*, **90**, 11,891–11,898.
- Ghil, M., S. Cohn, J. Tavantzis, K. P. Bube and E. Issacson (1981) Applications of estimation theory to numerical weather prediction. In: *Dynamic Meteorology: Data Assimilation Methods*, L. Bengtsson, M. Ghil and E. Kallen (editors), Springer-Verlag, New York, 330 pp.
- Hamilton, K. G., W. L. Siegmann and M. J. Jacobson (1980) Simplified calculation of ray-phase perturbations to ocean-environmental variations. *Journal of the Acoustical Society of America*, **67**, 1193–1206.
- Hogg, N. G. (1981) Topographic waves along 70°W on the continental rise. *Journal of Marine Research*, **39**, 627–649.
- Hogg, N. G. (1983) A note on the deep circulation of the western North Atlantic: Its nature and causes. *Deep-Sea Research*, **30**, 945–961.
- Hogg, N. G. (1985) Evidence for baroclinic instability in the Gulf Stream recirculation. *Progress in Oceanography*, **14**, 209–229.

- Hogg, N. G., Pickart, R. S., Hendry, R. M. and Smethie, W., Jr. (1986) The Northern Recirculation Gyre of the Gulf Stream, *Deep-Sea Research*, **33**, 1139–1165.
- Hogg, N. G. (1988) Stochastic wave radiation by the Gulf Stream. *Journal of Physical Oceanography*, **18**, 1687–1701.
- Hogg, N. G. (1992) *The Synoptician Album*, p. 11.
- Holland, W. R. and P. B. Rhines (1980) An example of eddy-induced ocean circulation. *Journal of Physical Oceanography*, **10**, 1010–1031.
- Howe B. M., B. D. Cornuelle, J. A. Mercer, K. Metzger and P. F. Worcester (1991) Acoustic mid-ocean dynamics experiment: 1991 moving ship tomography cruise. Technical Memorandum, APL-UW TM18-91, 57 pp.
- Howe, B. M., P. F. Worcester and R. C. Spindel (1987) Ocean acoustic tomography: Mesoscale velocity. *Journal of Geophysical Research*, **92**, 3785–3805.
- Jackson D. D. (1972) Interpretation of inaccurate, insufficient, and inconsistent data. *Geophysical Journal of the Royal Astronomical Society*, **28**, 97–109.
- Ko, D. S., H. A. DeFerrari and P. Malanotte-Rizzoli (1989) Acoustic tomography in the Florida Straits: Temperature, current, and vorticity measurements. *Journal of Geophysical Research*, **94**, 6197–6211.
- Lanczos, C. (1961) *Linear Differential Operators*. Van Nostrand, London, 564 pp.
- Lawson, C. L. and R. J. Hanson (1974) *Solving Least Squares Problems*. Prentice-Hall, Englewood Cliffs, New Jersey, 340 pp.
- Levitus, S. (1982) Climatological atlas of the world ocean. NOAA Professional Paper 13, Rockville, MD, 173 pp.
- Liebelt, P. B. (1967) *An Introduction to Optimal Estimation*. Addison-Wesley, Reading, Massachusetts, 273 pp.
- Luyten, J. R. (1977) Scales of motion in the deep Gulf Stream and across the Continental Rise. *Journal of Marine Research*, **35**, 49–74.
- Malanotte-Rizzoli, P., D. B. Haidvogel and R. E. Young (1987) Numerical simulation of transient boundary-forced radiation. Part 1: The linear regime. *Journal of Physical Oceanography*, **17**, 1439–1457.
- Malanotte-Rizzoli, P., N. G. Hogg and R. E. Young (1992) Stochastic wave radiation by the Gulf Stream: Numerical experiments. In preparation.

- Metzger, K. Jr. (1983) Signal processing equipment and techniques for use in measuring ocean acoustic multipath structures. Cooley Electronics Laboratory / University of Michigan Technical Report 231, 342 pp.
- Moller, D. A. (1976) A computer program for the design and static analysis of single-point subsurface mooring systems: NOYFB. Woods Hole Oceanographic Institution Technical Report, WHOI-76-59, 106 pp.
- Munk, W. and A. M. G. Forbes (1989) Global ocean warming: An acoustic measure? *Journal of Physical Oceanography*, **19**, 1765–1778.
- Munk, W. and C. Wunsch (1979) Ocean acoustic tomography: A scheme for large-scale monitoring. *Deep-Sea Research*, **26A**, 123–161.
- Munk, W. and C. Wunsch (1982) Up-down resolution in ocean acoustic tomography. *Deep-Sea Research*, **29**, 1415–1436.
- Munk, W. and C. Wunsch (1983) Ocean acoustic tomography: Rays and modes. *Reviews of Geophysics and Space Physics*, **21**, 777–793.
- Nerem, R. S., B. D. Tarpley and C. K. Shum (1990) Determination of the ocean circulation using Geosat altimetry. *Journal of Geophysical Research*, **95**, 3163–3179.
- Newhall, A. E., J. F. Lynch, C. S. Chiu and J. R. Richardson (1990) Improvements in three-dimensional raytracing codes for underwater acoustics. In: *Computational Acoustics – Volume 1*, D. Lee, A. Cakmak and R. Vichnevetsky (editors), Elsevier, Holland, 169–185.
- Ocean Tomography Group, The (1982) A demonstration of ocean acoustic tomography. *Nature*, **299**, 121–125.
- Officer, C. B. (1958) *Introduction to the Theory of Sound Transmission*. McGraw-Hill, New York, 284 pp.
- Owens, W. B. (1991) A statistical description of the mean circulation and eddy variability in the northwestern Atlantic using SOFAR floats. *Progress in Oceanography*, **28**, 257–303.
- Pedlosky, J. (1977) On the radiation of meso-scale energy in the mid-ocean. *Deep-Sea Research*, **24**, 591–600.
- Pedlosky, J. (1979) *Geophysical Fluid Dynamics*. Springer-Verlag, New York, 624 pp.

- Plumb, R. A. (1986) Three-dimensional propagation of transient quasi-geostrophic eddies and its relationship with the eddy forcing of the time-mean flow. *Journal of the Atmospheric Sciences*, **43**, 1657–1678.
- Rhines, P. B. and W. R. Holland (1979) A theoretical discussion of eddy-driven mean flows. *Dynamics of Atmospheres and Oceans*, **3**, 289–325.
- Richardson, P. L. (1983) A vertical section of eddy kinetic energy through the Gulf Stream System. *Journal of Geophysical Research*, **88**, 2705–2709.
- Richardson, P. L. (1985) Average velocity and transport of the Gulf Stream near 55°W. *Journal of Marine Research*, **43**, 83–111.
- Richman, J. G., C. Wunsch and N. G. Hogg (1977) Space and time scales of mesoscale motion in the western North Atlantic. *Reviews of Geophysics and Space Physics*, **15**, 385–420.
- Shay, T. and J. Bane (1992) *The Synoptician Album*, p. 30.
- Spiesberger, J. L. (1985) Ocean acoustic tomography: Travel time biases. *Journal of the Acoustical Society of America*, **77**, 83–100.
- Spiesberger, J. L. and P. F. Worcester (1983) Perturbations in travel time and ray geometry due to mesoscale disturbances: A comparison of exact and approximate calculations. *Journal of the Acoustical Society of America*, **74**, 219–225.
- Spiesberger, J. L. and K. Metzger (1991) Basin-scale tomography: A new tool for studying weather and climate. *Journal of Geophysical Research*, **96**, 4869–4889.
- Spiesberger, J. L., R. C. Spindel and K. Metzger (1980) Stability and identification of ocean acoustic multipaths. *Journal of the Acoustical Society of America*, **67**, 2011–2117.
- Spindel, R. C. (1985) Signal processing in tomography. In: *Adaptive Methods in Underwater Acoustics*, H. G. Urban (editor), D. Reidel Publishing Company, pp. 687–710.
- Spindel, R. C. and P. F. Worcester (1991) Ocean acoustic tomography: A decade of development. *Sea Technology*, July, pp. 47–52.
- Spofford, C. W. (1969) The Bell Laboratories multiple-profile raytracing program. Informal report.

- Stammer, D. and C. W. Böning (1992) Mesoscale variability in the Atlantic Ocean from Geosat altimetry and WOCE high-resolution numerical modeling. *Journal of Physical Oceanography*, **22**, 732–752.
- Stoughton, R. B., S. M. Flatté and B. M. Howe (1986) Acoustic measurements of internal wave rms displacement and rms horizontal current off Bermuda in late 1983. **91**, 7721–7732.
- Tai, C-K and W. B. White (1990) Eddy variability in the Kuroshio Extension as revealed by satellite imagery: Energy propagation away from the jet, Reynolds stress, and seasonal cycle. *Journal of Physical Oceanography*, **20**, 1761–1777.
- Talley, L. D. (1983a) Radiating barotropic instability. *Journal of Physical Oceanography*, **13**, 972–987.
- Talley, L. D. (1983b) Radiating instabilities of thin baroclinic jets. *Journal of Physical Oceanography*, **13**, 2161–2181.
- Tarbell, S., A. Spencer and R. E. Payne (1978) A compilation of moored current meter data and associated oceanographic observations, Volume 27 (Polymode Array 2 data). Woods Hole Oceanographic Institution Technical Report, WHOI-78-49, 87 pp.
- Thompson, R. (1971) Topographic Rossby waves at a site north of the Gulf Stream. *Deep-Sea Research*, **18**, 1–20.
- Thompson, R. (1977) Observations of Rossby waves near Site D. *Progress in Oceanography*, **7**, 1–28.
- Thompson, R. (1978) Reynolds stress and deep counter-currents near the Gulf Stream. *Journal of Marine Research*, **36**, 611–615.
- Urlick, R. J. (1983) *Principles of Underwater Sound*. McGraw-Hill, New York, 423 pp.
- Welsh, E. B., N. G. Hogg and R. M. Hendry (1991) The relationship of low-frequency deep variability near the HEBBLE site to Gulf Stream fluctuations. *Marine Geology*, **99**, 303–317.
- Wiggins, R. A. (1972) The general linear inverse problem: Implication of surface waves and free oscillations for earth structure. *Reviews of Geophysics and Space Physics*, **10**, 251–285.
- Wiggins, R. A., K. L. Larner and R. D. Wisecup (1976) Residual statics analysis as a general linear inverse problem. *Geophysics*, **41**, 922–938.

- Worcester, P., B. Dushaw and B. Howe (1991) Gyre-scale reciprocal acoustic transmissions. In: *Ocean Variability and Acoustic Propagation*, J. Potter and A. Warn-Varnas (editors), Kluwer Academic, Netherlands, pp. 119–134.
- Worthington, L. V. (1976) *On the North Atlantic Circulation*. The Johns Hopkins Oceanographic Studies, **6**, 110 pp.
- Wunsch, C. (1978) The North Atlantic general circulation west of 50°W determined by inverse methods. *Reviews of Geophysics and Space Physics*, **16**, 583–620.
- Wunsch, C. (1983) Western North Atlantic interior. In: *Eddies in Marine Science*, A. R. Robinson (editor), Springer-Verlag, New York, 609 pp.
- Wyrski, K., L. Magaard, and J. Hager (1976) Eddy energy in the oceans. *Journal of Geophysical Research*, **81**, 2641–2646.